Emissivity Measurements of MAP Satellite Optics

Nathaniel R. Butler

Physics Department Senior Thesis

Advisor: Dr. Lyman Page, Jr.

Princeton University

April 13, 1998

Abstract

We measure the emissivity of two aluminum-coated composites designed for use as the MAP satellite reflector. It is desired that the emissivity be indistinguishable from that of bulk aluminum at room temperature and 90GHz. We measure the emissivity difference between the reflector surface and 6061-T6 aluminum alloy and compare the results with a theoretical value for the emissivity of aluminum. We also measure the emissivity of a sample of the proposed Greenbank telescope reflector.

We investigate a number of systematic effects including beam spill, uncertainty in the system calibration, signal variations due to variations in the sample flatness, the effect of the relative height of the sample on the sample emissivity, and the emission from the polyester tape used to hold samples in place.

Contents

Appendix A: Data and Specifications Sheets

Appendix B: How to Operate the Apparatus

I. Introduction

The Cosmic Microwave Background (CMB) is our most direct link to the early universe. It is what remains of the oldest photons we can observe—those freed to stream outward when the universe first became transparent at decoupling, roughly 200,000 years after the Big Bang. Prior to the recombination of atomic hydrogen, matter and radiation are in constant communication. Photons frequently Thompson scatter off of free electrons. Fluctuations in the matter are accompanied by fluctuations in the radiation. When the universe has expanded and cooled sufficiently for hydrogen to recombine, photons can travel essentially unimpeded across the universe, carrying with them the signature of primordial density fluctuations in the photon-baryon fluid.

These fluctuations, now seen as anisotropies in the CMB a part in 10^5, were first detected by NASA's Cosmic Background Explorer (COBE), launched in 1992. COBE's angular resolution was, however, limited to 7°. The Microwave Anisotropy Probe (MAP) satellite is designed to improve this, to achieve a resolution of approximately 0.3° over the entire sky. This is enough spatial resolution to compare sections of the CMB which were causally connected at decoupling. Planned for launch in the fall of 2000, the MAP satellite is expected to provide answers to cosmology's biggest questions. The data will help us to understand structure formation in the universe if the current popular models are correct. It will strongly constrain the values of the cosmological parameters such as $\Omega_\circ$, Ω_b, Λ, and $H_\circ$. It will describe the ionization history after decoupling.

For MAP to be effective in measuring the CMB to such unprecedented precision, systematic effects will have to be strictly controlled. In this experiment, we test the emissivity of the satellite reflectors.

The map reflectors are lightweight and sturdy composites coated with vapor-deposited aluminum (VDA) produced by Surface Optics Corporation. They are designed to withstand the extreme temperature variations associated with space flight while retaining excellent optical properties. The composites should be highly reflective at radio frequencies, the surface emitting very little radiation itself. The optical specifications require the composites to be no more than 0.1% emissive at 90GHz, essentially indistinguishable from the emisssivity of bulk aluminum. We received two 12 by 12 inch sample sections for testing. We measure their emissivities at room temperature and 90GHz to determine whether or not they meet specifications. Our results (Table 1) suggest that they do.

We also report measurements made of a section of the proposed Greenbank telescope's reflector (Table 1).

Ia. Experimental Overview

We measure the emissivity differences at 90GHz between aluminum (6061-T6) and four other materials– AISI 304 stainless steel, oxygen-free (OF) copper, MAP VDA composites, a section of the Greenbank telescope's reflector. The samples are mounted on aluminum disks. The disks are at 45° relative to the ground and are rotated at about 1Hz as shown in Figure 1. Below the disk, there is a nitrogen cold load.

The nitrogen bath is lined with microwave absorber (Appendix p. A2) ($e \approx 1$), and thus has an effective temperature approximately equal to the boiling point of nitrogen (77K). The quantity e is the emissivity, a measure of the radiative efficiency of a body, as explained in the next section. The area around the bath is also lined with microwave absorber to prevent reflected signals from reaching the sample.

A W-band radiometer centered at 90GHz receives the radiation emitted

Figure 1. The experimental setup. We measure the emissivities at an incidence angle of 45°. The signal received by the horn is the sum of the radiation emitted by the disk and the radiation emitted by the bath and reflected by the disk. Our convention for treating the two polarizations is also displayed. Here, the emissivity is labeled e.

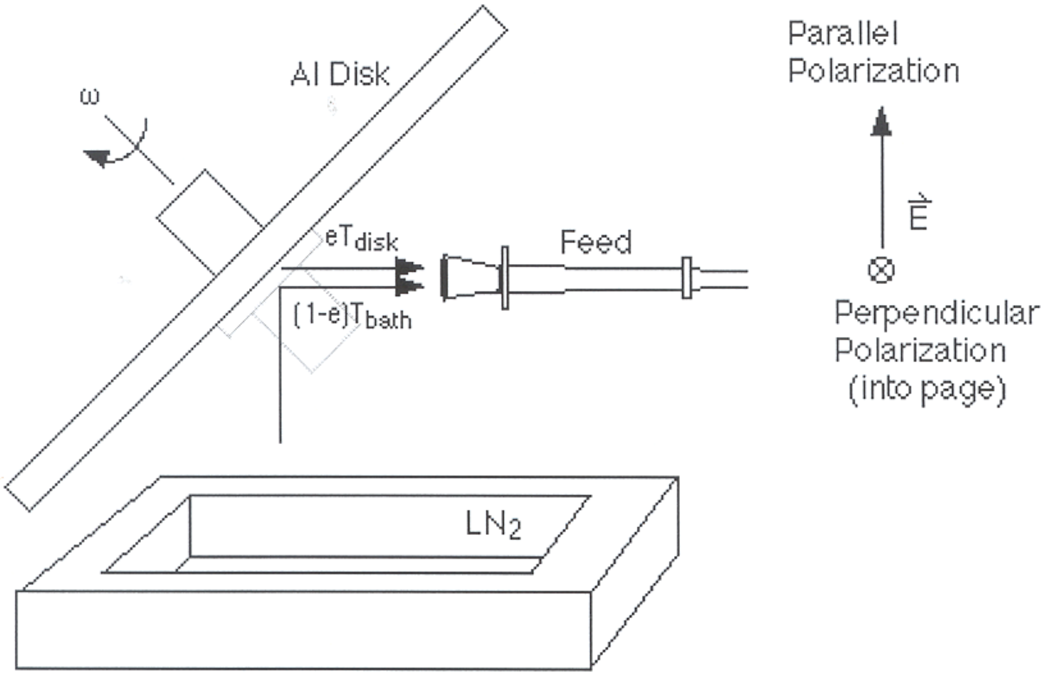

and reflected by the sample. The signal it receives is the sum of the radiation emitted by the sample at room temperature (293K) and the radiation emitted by the microwave absorber at 77K reflected by the disk. For a surface that is opaque and transmits nothing, the fraction of incident radiation absorbed, the absorptivity, is equal to one minus the fraction reflected, the reflectivity. Kirchoff's law then tells us that the absorptance is equal to the emissivity. It follows that the total signal is:

$$T_s = eT_{Disk} + (1-e)T_{Bath}. \tag{1}$$

For a typical measurement, the sample is mounted, with a flush surface, to an aluminum disk. Denote the sample's emissivity by e_s and the emissivity of the disk by e_{Al}. As the disk rotates, we will see two signals of the form in equation (1). The difference between these two is

$$\Delta T_s = (e_s - e_{Al})(T_{Disk} - T_{Bath}). \tag{2}$$

To find the emissivity difference, we take the voltage output of the radiometer, which is directly proportional to ΔT_s, and divide by $T_{Disk} - T_{Bath} = 216\text{K}$. Typical values for the emissivity difference will be on the order of 10^{-4}. To measure ΔT_s's that are this many orders of magnitude smaller than the body's physical temperatures, the apparatus needs to be very stable. The only part of the system that we allow to change is the sample we are measuring.

The main source of (instantaneous) noise is Gaussian white noise (constant over all frequencies) from the radiometer. There is also noise from the 110V lines in the walls (at 60Hz), from mechanical vibrations, etc. These are reduced by chopping the radiometer output signal at 1Hz (the disk rotation frequency) and averaging the signal over many periods. This removes signals occurring at frequencies other than 1Hz and leaves only the variations we wish to measure. Figure 2 shows some typical data taken with our apparatus. We discuss systematic error when determining the final emissivities in later sections.

Our results are displayed in Table 1. We treat the two polarization of the electromagnetic field as one component parallel to the plane of reflection and one component perpendicular to the plane of reflection. Our convention is displayed in Figure 1. In addition to radiation incident at 45°, we present estimated values for the emissivity at normal incidence.

We have three strong reasons, as discussed in Section VI, for believing that our results are significant. First, our measurements of the emissivity of oxygen-free copper are self-consistent and consistent with emission at an incidence angle of 45°. (Section VI) Also, our results for copper are consistent with the theoretical value. (Section VI) Second, our measurements of the emissivity of AISI 304 stainless steel are self-consistent and strongly suggest an incidence angle of 45°. (Section Vf4) Further, our results for stainless steel

Figure 2. A typical sample. Samples are held in place by polyester tape. The MAP VDA samples are, in addition, fixed to the bulk aluminum by flathead screws epoxied to the sample underside as explained below. The outlined ellipse on the sample shows the location and size of the beam. Imagine this ellipse moving around the disk as the disk rotates.

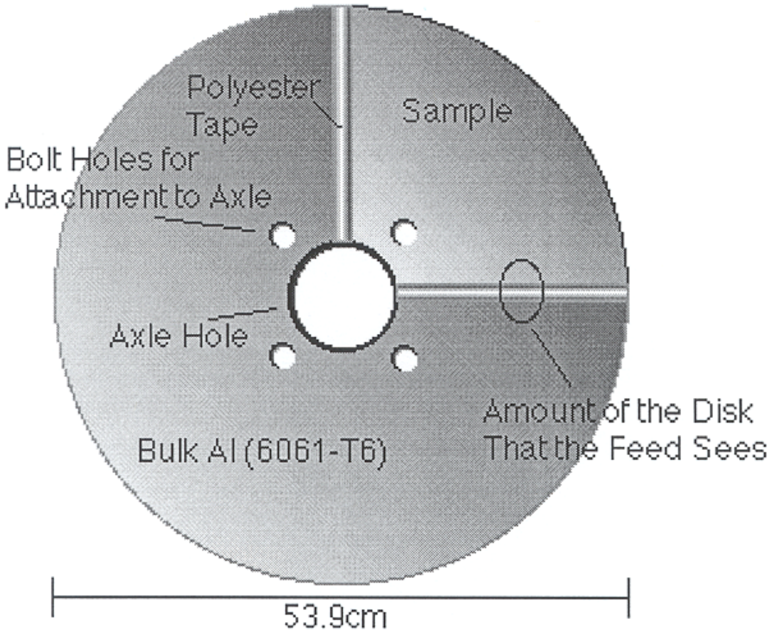

Figure 3. Typical disk surface data taken in this experiment. This is MAP VDA #1, measured 10/31/97. The temperature scale is inverted; so more emissive corresponds to lower temperatures. We fit a straight line to the data over each section of the disk. The χ^2/ν's describe the accuracy of these fits. To find emissivity, divide y-axis temperatures by 216K. The signal dips are due to the tape.

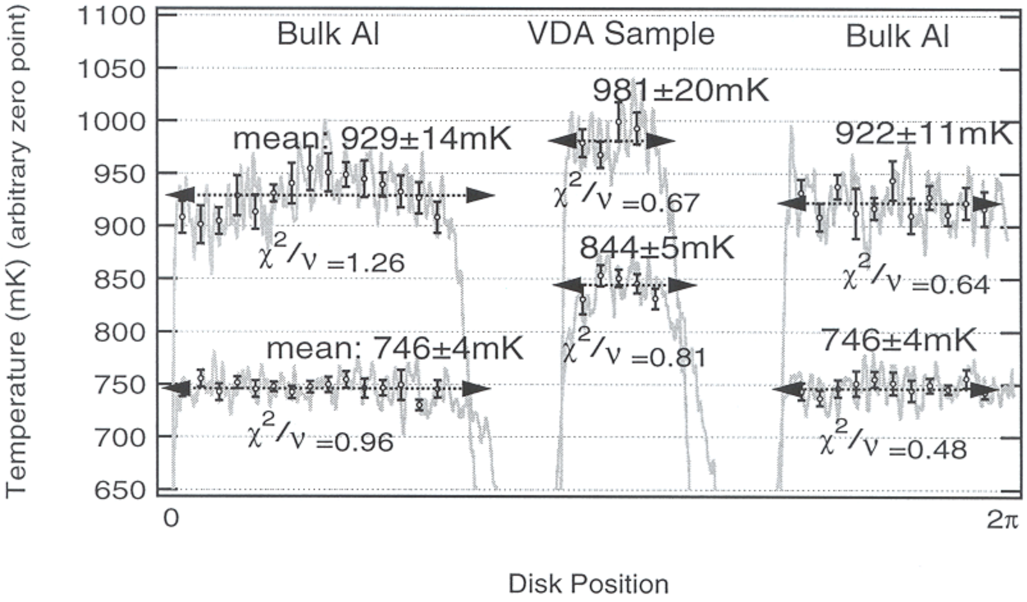

are consistent with the theoretical value. (Section VI) Thirdly, our results from

Table 1: Absolute Emissivities for all materials measured and calculated, at room temperature and 90GHz and $\theta_{inc} = 45°$*. Calculated values are from the model in Section IIa and corresponding material names are in italics.* $E_{\|}$ *denotes the parallel polarization and* $E_{\perp}$ *denotes the perpendicular polarization.*

	$E_{\|}$, $\theta_{inc} = 45°$	$E_{\perp}$, $\theta_{inc} = 45°$	Normal Incidence
Pure Al	$1.46 \pm 0.001 \times 10^{-3}$	$7.28 \pm 0.01 \times 10^{-4}$	$1.03 \pm 0.001 \times 10^{-3}$
6061-T6 Al	$1.826 \pm 0.044 \times 10^{-3}$	$9.14 \pm 0.22 \times 10^{-4}$	$1.29 \pm 0.031 \times 10^{-3}$
MAP VDA #1	$1.59 \pm 0.30 \times 10^{-3}$	$4.6 \pm 2.7 \times 10^{-4}$	$8.1 \pm 5.3 \times 10^{-4}$
MAP VDA #2	$2.13 \pm 0.27 \times 10^{-3}$	$6.7 \pm 2.6 \times 10^{-4}$	$1.14 \pm 0.56 \times 10^{-3}$
Greenbank	$4.07 \pm 0.50 \times 10^{-3}$	$1.45 \pm 0.35 \times 10^{-3}$	$2.39 \pm 0.84 \times 10^{-3}$
AISI 304	$8.31 \pm 0.89 \times 10^{-3}$	$4.11 \pm 0.57 \times 10^{-3}$	$5.76 \pm 0.75 \times 10^{-3}$
AISI 304	$7.58 \pm 0.02 \times 10^{-3}$	$3.80 \pm 0.01 \times 10^{-3}$	$5.367 \pm 0.016 \times 10^{-3}$
OF Cu	$1.31 \pm 0.29 \times 10^{-3}$	$7.51 \pm 3.0 \times 10^{-4}$	$1.06 \pm 0.43 \times 10^{-3}$
OF Cu	$1.16 \pm 0.01 \times 10^{-3}$	$5.82 \pm 0.03 \times 10^{-4}$	$8.22 \pm 0.05 \times 10^{-4}$

a test in which we rotate the field polarizations by 45° (Section Vf3) indicate both that the geometry of the setup is correct and that our radiometer is extemely self-consistent.

We will now list and briefly describe the different samples that we analyze during this experiment.

Ib. Sample Descriptions

Bulk Al Disk: 6061-T6 aluminum disks are central to this experiment. Surfaces are smooth and sanded to eliminate grooves in any particular direction. One aluminum disk is used exclusively as the system baseline. The other primary function of the plain aluminum disks is to serve as a substrate for systematic effect tests. We have four plain aluminum disks.

MAP VDA samples: The primary goal of this experiment is to constrain the emissivities of two 12 by 12 inch samples of the MAP satellite reflector. We received the first in mid October and the second in early January. The samples are aluminum coated composites, 245μm (0.01") thick, inset into a 6061-T6 aluminum disk. The samples have an rms roughness of 0.5μm. The construction is three layer: composite XN70 cloth, a VDA (vapor-deposited aluminum) coating 3μm thick, and a protective layer of SiO$_x$ (slow-fire silicon oxide) 2.5μm thick. SiO$_x$, which emits very strongly at 10μm, is employed to radiate away solar energy. It keeps the reflector surface cool in space. For MAP VDA #1, the sample is higher than the disk around it by approximately 120μm. For MAP VDA #2, the height is closer to 25μm. Information for the reflector and coating is in Appendix A. (p.A3)

Cu-Al-SS: This is a tri-metal sample. One third is OF copper. One third is 6061-T6 aluminum alloy. One third is AISI 304 stainless steel. The primary function of this sample is to employ the large aluminum-stainless emissivity difference in gauging the system calibration. We also check that the copper-aluminum emissivity difference measured agrees with the theoretical value.

Raised Al: This sample consists of a bulk aluminum (6061-T6) disk with a section of 490μm thick 6061-T6 sheet aluminum. Unlike the test samples, this aluminum is 490μm above the disk surface. It is used to test the effect of a raised surface on the sample emissivity.

Raised SS: Like the previous sample, this is used to gauge the effects of a raised surface. It consists of a 490μm sheet of AISI 304 stainless steel mounted to 6061-T6 aluminum plate. Unlike the test samples, this surface is 490μm above the disk surface. This sample is also used to gauge error in the system calibration.

Lowered Al: A wedge of this 6061-T6 aluminum plate has been milled out to a depth of 245μm. This disk is the same as those containing the MAP VDA samples, with the sample removed. It is used to test the effect of a lowered surface on the sample emissivity.

Greenbank: This is a sample from the Greenbank telescope's reflector. We began testing the 12 by 12 inch sample of the proposed reflector for the Greenbank telescope in late February of 1998. The reflector consists of a 93.1 μm (0.0038") layer of GBT Goldstone Paint on an aluminum plate. The rms roughness of the surface is 3.43μm (0.00014"). The total sample thickness is 2.205mm (0.09"). It is inset in an aluminum disk. We wish to measure the emissivity as for the MAP VDA samples. Information for the reflector and coating is in Appendix A. (p.A4-A6)

Note: The mounting of all samples is done by first milling out a section from a bulk aluminum disk so that the sample will be flush with disk surface. Next holes are drilled into the back of the disk where the sample will be attached. We epoxy bolts to the undersides of the samples and use these holes to fasten the bolts to the disk. Finally, we use polyester film tape (1.23cm (0.5") wide, 46.6μm (0.0019") thick) along the edges. This tape is between the sample and the aluminum disk on the face of the disk which is measured and hides the gap at the edges (Figure 2). The systematic effect related to having this tape in the beam path is discussed below.

II. Theory

Any body at non-zero temperature emits electromagnetic radiation. The radiated power W is characterized in terms of the energy that an ideal blackbody would emit per unit time W_{BB} at that temperature. The ratio is defined as the body's emissivity e:

$$e = \frac{W}{W_{BB}}. \tag{3}$$

The emissivity ranges from 1 for a perfect absorber of radiation (a blackbody) to 0 for a perfect reflector of radiation. The emissivity can be a function of frequency, angle, and temperature.

In the sections that follow, we discuss first the predicted functional form for the emissivity from Maxwell's equations. We plug in numbers and calculate the expected emissivities for our copper, aluminum, and stainless steel samples. Next we discuss the role of emissivity in allowing us to define an effective temperature for a radiating body. We discuss the useful convention of treating all noise powers, signal and system, in terms of effective temperatures.

IIa. Emissivity for Oblique Incidence

The emissivity of a metallic surface can be calculated from first principles as a function of the frequency of radiation emitted, the angle at which the emission occurs, and the conductivity of the metal. If the metal's surface is relatively smooth, the emittance is specular and is described by the Fresnel equations. The requirement of a surface for specular rather that diffuse emittance is $\sigma/\lambda <0.05$, where σ is the rms roughness in one dimension and λ is the wavelength of radiation. (Touloukian p. 16a) At 90GHz, we need $\sigma <170\mu$m, which is satisfied by the materials in this experiment. For the MAP VDA samples, the reported σ is 0.5μm. In the discussion that follows, we outline the derivation of the Fresnel equations, derive the complex index of refraction for a metal, combine the two, and solve for the emissivity.

Consider the oblique incidence of an electromagnetic wave as in Figure (4). We are interested in the case when $\theta_\circ = 45°$. The incident E field vector can be written as

$$\vec{E}_\circ = \vec{E}^\circ_\circ e^{i(\vec{k}_\circ \cdot \vec{r} - \omega t)} \tag{4}$$

where $\vec{E}^\circ_\circ$ is the amplitude. From Maxwell's equations, the H field is:

$$\vec{H}_\circ = n\hat{k}_\circ \times \vec{E}_\circ \tag{5}$$

where n is the index of refraction, approximately equal to unity in air. A portion of the wave will be reflected and another transmitted. Denote the reflected fields as

$$\begin{aligned} \vec{E}_1 &= \vec{E}^\circ_1 e^{i(\vec{k}_1 \cdot \vec{r} - \omega t)} \\ \vec{H}_1 &= \hat{k}_\circ \times \vec{E}_1 \end{aligned} \tag{6}$$

where n has been set equal to 1. Denote the transmitted fields

$$\begin{aligned} \vec{E}_2 &= \vec{E}^\circ_2 e^{i(\vec{k}_2 \cdot \vec{r} - \omega t)} \\ \vec{H}_2 &= n_m \hat{k}_2 \times \vec{E}_2 \end{aligned} \tag{7}$$

where n_m is the complex index of refraction of the metal.

The functional form of the complex index of refraction can be found by comparing the Ampere-Maxwell equation written for a metal to the equation written for a non-conducting material. In its most general and macroscopic form, the equation is

$$\vec{\nabla} \times \vec{H} - \frac{1}{c}\frac{\partial \vec{D}}{\partial t} = \frac{4\pi}{c}\vec{J}_f \tag{8}$$

where $\vec{J}_f$ is the current due to free charge carriers. For a linear medium, it is true that $\vec{D} = \epsilon\vec{E}$, where ϵ is the medium's dialectric constant, and $\vec{J}_f = \sigma\vec{E}$, where σ is the conductivity of the medium. We will assume that the field is periodic in time as $e^{-i\omega t}$.

Figure 4. Electromagnetic radiation incident on the boundary of two medium. Picture taken from Heald & Marion (1995).

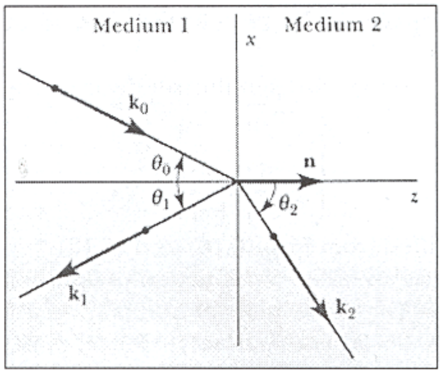

For a non-conducting material, there is no free current. Equation (8) reduces to

$$\vec{\nabla} \times \vec{H} - \frac{\epsilon}{c}(-i\omega)\vec{E} = 0 \tag{9}$$

For a conducting medium, it becomes

$$\vec{\nabla} \times \vec{H} - (\epsilon + i\frac{4\pi\sigma}{\omega})\frac{1}{c}(-i\omega)\vec{E} = 0 \tag{10}$$

Thus, the situations are mathematically identical if we define the quantity in brackets in equation (10) as a *complex dialectric constant.* The index of refraction for a non-magnetic medium is just the square root of the dialectric constant. Hence, the complex index of refraction is defined as

$$n_m \equiv \sqrt{\epsilon + i\frac{4\pi\sigma}{\omega}} \tag{11}$$

For the case of high conductivity (when the conductive current is much larger than the displacement current) it will be an excellent approximation at low frequency to write $4\pi\sigma >> \epsilon\omega$. For aluminum at room temperature, with ν =90GHz, $4\pi\sigma/\epsilon\omega \sim 10^6$. Also, the conductivity σ in equation (11) is essentially the DC conductivity σ_{DC} of the metal. At 90GHz, as explained below, the wave period is so much longer than the relaxation time of a conduction band electron that the electrons remain effectively undisturbed.

For electrons in good conductors, the relaxation time is set by the mean free time between electron collisions. The characteristic relaxation time, describing

Table 2: Physical data (resistivity ρ, conduction band electron density N, skin depth δ, Fermi velocity v_f, conduction band electron mean free time τ and mean free path l) for OF copper, pure aluminum, aluminum (6061-T6), and stainless steel (AISI 304) at room temperature (293K) and 90GHz. We suppress the uncertainties on all quantities except the resistivities.

	OF Cu	Pure Al	Al 6061-T6	AISI 304
ρ (nΩ-m)	$16.9 \pm 0.1^{\star}$	$26.48 \pm 0.02^{\dagger}$	$41.7 \pm 1.7^{\star}$	$722 \pm 2^{\star}$
N (10^{22}cm^{-3})	8.45	18.06	18.06	15.55
δ (10^{-5}cm)	2.20	2.73	3.43	14.25
v_f (10^8cm/s)	1.57	2.02	2.02	1.93
τ (10^{-16}s)	243.60	74.15	47.13	3.17
l (10^{-8}cm)	382.84	150.10	95.42	6.10

† *Taken from: Reed, R., P., Clark, A., F. Materials at Low Temperature. American Society for Metals. Metals Park, Ohio: 1983. p. 195.*

⋆ *Extrapolated from data in: Reed, R., P., Clark, A., F. Materials at Low Temperature. American Society for Metals. Metals Park, Ohio: 1983. p. 196-7.*

the way charge spreads out in time, that comes from the charge continuity equation ($\tau = \epsilon/4\pi\sigma_{DC}$) is much shorter. We can calculate an approximate mean free time using the Drude model:

$$\tau = \frac{m\sigma_{DC}}{Ne^2} \tag{12}$$

where m and e are the electron mass and charge respectively and N is the conduction band electron density. Values for these quantities can be found in Table 2. In this experiment, the largest mean free time that we will come across (for copper) is 450 times smaller than the wave period. With these approximations:

$$n_m = \sqrt{i\frac{4\pi\sigma_{DC}}{\omega}}. \tag{13}$$

This form for n_m will be sufficient for this experiment.

There are two corrections which are important at higher frequencies. First, if the skin depth δ, given by

$$\delta = \frac{c}{\sqrt{2\pi\sigma\omega}}, \tag{14}$$

is smaller than the conduction band electron mean free path l, given by

$$l = v_f\tau \text{ with } v_f = \frac{\hbar}{m}(3\pi^2 N)^{1/3} \text{ (Fermi Velocity)}, \tag{15}$$

Figure 5. Radiation with E field parallel to the plane of reflection. Picture taken from Heald & Marion (1995).

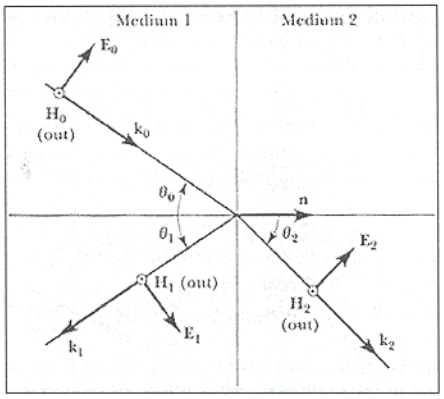

Figure 6. Radiation with E field perpendicular to the plane of reflection. Picture taken from Heald & Marion (1995).

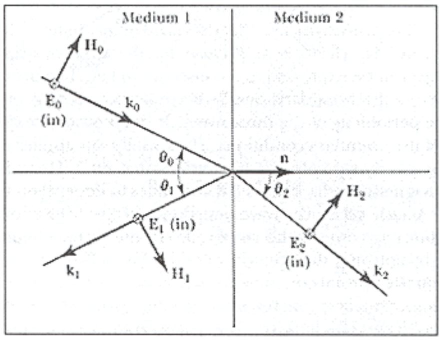

then the “anomalous skin effect” becomes important. From Table 2, it is apparent that it is not important here. Second, there is the relaxation effect which becomes important when the wave period becomes larger than the collisional time. This, as discussed above, is also not important here.

To simplify the discussion of our electromagnetic field obliquely incident off of a metallic surface, we consider two different possibilities. First, the E field polarization could be perpendicular to the plane of reflection as in Figure 5. Second, the E field polarization could be parallel to the plane of reflection as in Figure 6. Any other case can be constructed as a linear combination of these two.

For both polarizations we will use the field boundary conditions to relate incident, reflected, and transmitted field amplitudes. For the E and H fields, the boundary conditions require the tangential field components to be continuous across the boundary of the two mediums. That is, if we call the vector normal to the metal's surface $\vec{n}$,

$$(\vec{E}_{\circ} + \vec{E}_1) \times \vec{n} = \vec{E}_2 \times \vec{n}, \tag{16}$$

and likewise for H. In the parallel polarization, for example, the E fields are already tangential to the boundary. Thus

$$\vec{E}^{\circ}_{\circ} + \vec{E}^{\circ}_{1} = \vec{E}^{\circ}_{2}. \tag{17}$$

Applying the boundary conditions to the rest of the field components isn't so attractive. Nonetheless, after a deluge of algebra, one finds relationships between each field amplitude, the Fresnel equations. We are interested in the two Fresnel equations describing the relative amplitudes of the incident and reflected signals. They are

$$\vec{E}^{\circ}_{1}/\vec{E}^{\circ}_{\circ} = \frac{n_m \, cos\,\theta_{\circ} - cos\,\theta_2}{n_m \, cos\,\theta_{\circ} + cos\,\theta_2}, \tag{18}$$

for the parallel polarization, and

$$\vec{E}^{\circ}_{1}/\vec{E}^{\circ}_{\circ} = \frac{cos\,\theta_{\circ} - n_m \, cos\,\theta_2}{cos\,\theta_{\circ} + n_m \, cos\,\theta_2} \tag{19}$$

for the perpendicular polarization.

The fraction of the incident wave that gets reflected is $R = |\vec{E}^{\circ}_{1}|^2/|\vec{E}^{\circ}_{\circ}|^2$. The fraction T that gets transmitted is then $1 - R$. By detailed balance, this is also the emissivity. We use Snell's law, which follows from the boundary conditions (equation (16)), to get rid of θ_2 in equations (18) and (19):

$$sin\,\theta_{\circ} = n_m \, sin\,\theta_2 \tag{20}$$

gives

$$cos\,\theta_2 = \sqrt{1 - \frac{sin^2\,\theta_{\circ}}{n_m^2}}. \tag{21}$$

Table 3: Calculated emissivities at 45° for OF copper, pure aluminum, aluminum (6061-T6), and stainless steel (AISI 304) at room temperature (293K) and 90GHz.

	OF Cu	Pure Al	Al 6061 (T6)	AISI 304
$e_{\parallel}$ (10^{-4})	11.63 ± 0.07	14.55 ± 0.01	18.26 ± 0.44	75.76 ± 0.21
$e_{\perp}$ (10^{-4})	5.82 ± 0.03	7.28 ± 0.01	9.14 ± 0.22	37.95 ± 0.11

Finally, we plug in $\theta_{\circ} = 45°$ and equation (13) for the complex index of refraction, to find

$$e_{\parallel} = 1 - \left| \frac{n_m^2 - \sqrt{2n_m^2 - 1}}{n_m^2 + \sqrt{2n_m^2 - 1}} \right|^2 \approx 2\sqrt{\frac{\omega}{\pi \sigma_{DC}}} \tag{22}$$

and

$$e_{\perp} = 1 - \left| \frac{1 - \sqrt{2n_m^2 - 1}}{1 + \sqrt{2n_m^2 - 1}} \right|^2 \approx \sqrt{\frac{\omega}{\pi \sigma_{DC}}}. \tag{23}$$

For the last step in each equation above, the form (13) for the complex index of refraction is inserted and the high conductivity condition is used to approximate. The error in this approximation is on the order of +0.1% for the materials in this experiment. Calculated values for the relevant materials are displayed in Table 3.

As all of the emissivities we measure are relative to the emissivity of Al 6061-T6, our value for the resistivity of Al 6061-T6 is very important The reported values in metallurgical handbooks and from vendors range from 40-42nΩ-m. (e.g. Metals Handbook p.1.66) The best experimental data we could locate, from Reed & Clark (1983), only extends to 273K. Nonetheless, this data appears to be very linear at temperatures above 77K. We, therefore, extrapolate from their measured curve and find ρ =41.7±0.1nΩ-m. To allow for all of the reported values, we increase the uncertainty to ±1.7. Similarly, for AISI 304, we use the data in Reed & Clark to find ρ=722±2nΩ-m. And likewise for OF Cu, 16.9±0.1nΩ-m. These values are reported in Table 2.

IIb. Blackbody Radiation and Effective Temperatures

The spectral emission power of a blackbody (per unit area, per unit solid angle) is given by the Planck radiation law:

$$B_\nu = \frac{2h\nu^3}{c^2}\frac{1}{e^{h\nu/kT}-1}. \tag{24}$$

For this experiment, for radiation at ν =90GHz emitted from a body at liquid nitrogen and room temperatures, it is true that $h\nu << kT$. Thus, the correction between thermodynamic and brightness temperature can be ignored. We then expand the exponential in B_ν to get the Rayleigh-Jeans result:

$$B_\nu = \frac{2\nu^2}{c^2}kT. \tag{25}$$

The total power W_{BB} incident upon a surface A from a source for which B_ν is constant over a small bandwidth $\Delta\nu$ and spatial extent Ω is then

$$W_{BB} = \frac{2\nu^2}{c^2}kT\cdot\Delta\nu\cdot A\cdot\Omega. \tag{26}$$

For the case of noiseless antenna, the total received power per unit frequency range is:

$$W_\nu = \frac{1}{2}A_e\int\int B_\nu(\theta,\phi)P_n(\theta,\phi)d\Omega. \tag{27}$$

(Krauss p. 3-40) The factor of one half takes into account the fact that an antenna can only receive one of the two field polarizations. The effective area of the antenna, or the ratio of the total power the antenna receives to the incident flux of energy, is A_e. The normalized angular function $P_n(\theta,\phi)$ describes the antenna pattern. (See Appendix pp.A8, A9 for the pattern of our feed.)

For a source isotropic in space or simply constant while $P_n(\theta,\phi)$ is non-negligible, B_ν can be taken out of the integral. We can define $\Omega_A = \int\int P_n d\Omega$ and plug in equation (25) for B_ν to get

$$W = \frac{\nu^2}{c^2}kTA_e\Omega_A\Delta\nu. \tag{28}$$

Further, as one would expect, the wavelengths at which an antenna can radiate are constrained by its dimensions. Krauss (p. 6-5) demonstrates that

$$\lambda^2 = A_e\Omega_A. \tag{29}$$

With this result, we see that the antenna power is directly proportional to the temperature of the blackbody:

$$W = \Delta\nu \cdot kT. \tag{30}$$

We also see from (30) that it is possible to define an effective temperature T_e for a radiating body such that

$$T_e = eT \tag{31}$$

where T_e is always less that the physical temperature T.

Similarly, any circuit element can be treated as having an effective noise temperature. From Planck's law in the Rayleigh Jeans limit (equation (25)), Nyquist showed that the rms voltage v_{rms} due to the random motion of electrons is a resistor is

$$v_{rms} = \sqrt{4kT\Delta\nu R}. \tag{32}$$

(Pozar p.584) Here R is the resistance. The power is then

$$\left(\frac{v_{rms}}{2R}\right)^2 = kT\Delta\nu. \tag{33}$$

This result leads to an important simplification in discussions of radiometric noise measurements. Just as with electronic circuits we can describe an arbitrary circuit or circuit element by its Thevenin equivalent (i. e., by a matched resistor), we can describe an arbitrary noise source by an effective noise temperature T_N. Therefore for a source delivering power W to a load resistor R, we write

$$T_N = \frac{W}{GkB} \tag{34}$$

where G is whatever gain the element may have. The effective noise temperature defined in this manner generally bears no resemblance to the physical temperature of the object. It is typically a few orders of magnitude larger.

Nonetheless, it is a definition that makes the physics more transparent and greatly simplifies calculations.

As the proportionality constant for the power in the case of the antenna and in the case of the resistor is just the bandwidth $\Delta\nu$, and as the bandwidth is set in the radiometer (in our case by the first IF amplifier), it factors out of the calculations. The total power of the system is then just a linear combination of the source power plus the noise powers of each component, with each component's effective temperature weighted by the gain that it receives.

Two effective temperatures will be important here—the temperature of the source T_s detected via the antenna and the total effective temperature of the radiometric system T_{sys}. The total noise power at the radiometer output is

$$W_{total} = k(T_{sys} + T_s)\Delta\nu G. \tag{35}$$

We will use this expression for the system power in Section IVa when we discuss the system sensitivity. For this experiment, T_s is approximately 77K. For our radiometer, we measure T_{sys} =15800±2000K. (Section IVa) As T_{sys} is much larger, it is a good approximation to write

$$W_{total} = kT_{sys}\Delta\nu G. \tag{36}$$

Figure 7. The experimental setup. Samples are mounted on 53.9cm (22") diameter aluminum disks tilted 45° relative to the floor. A 24V motor rotates the disk at about 1Hz. The noise signal in thermal radiation is measured using a W-band radiometer centered at 90GHz. Every rotation, the noise signal is co-added to uncover variations in the sample noise from the receiver noise.

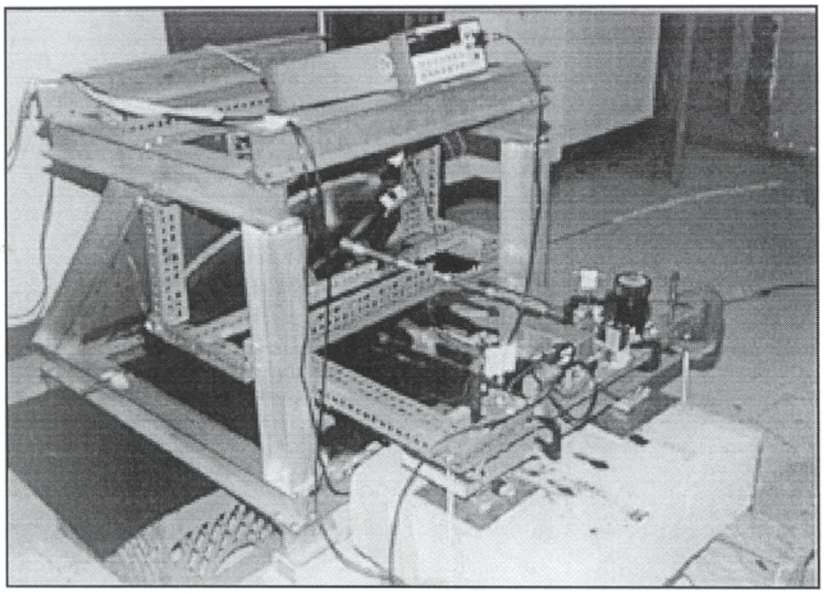

III. The Apparatus

IIIa. The Sample Setup

Samples to be measured are mounted on 53.9cm (22") diameter 1.23cm (0.5") thick aluminum plates. The support structure for the apparatus is a 71cm (29") by 76cm (31") by 90.7cm (37") aluminum cage constructed by Michael Kesden and me from June to August of 1997. The drivetrain, including the wheel axle and the motor, are mounted to a 1.23cm (0.5") aluminum plate which is bolted across the front (slanted) face of the cage. The axle contains two sets of pressure-loaded SKF ball bearings, tightly shimmed to ensure sample stability.

There is one ±15V power supply (SOLA SLD-15-3030-15) mounted to the bottom front of the cage. This provides the base voltages for the operational amplifier circuitry in the radiometer. There is also a 0-40V, 5A variable power supply (HP 6266B) mounted to the underside of the top of the cage which is

Figure 8. Schematic for the radiometer voltage regulation. This circuit is attached to the radiometer's aluminum base.

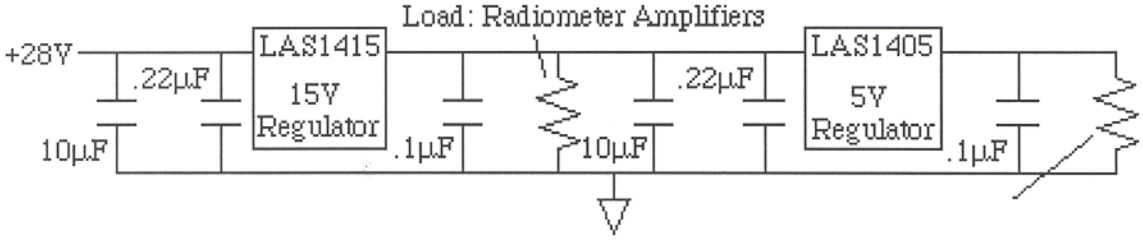

used to control the power to the motor. The rest of the system power comes from an external 28V power supply (Systron & Donner 0-160V, 0-15A). This is regulated down to 15V and 5V (Figure 8).

The cage was designed both to support the rotating sample and to protect and house the radiometer. The feed horn available to us was, however, much longer than the original cage design took into account. We used a specially elongated feed (designed for the MAP satellite) that forced the radiometer to rest behind and on the outside of the cage. We fixed the radiometer in position with a steel infrastructure, extended from inside the cage. We also support the radiometer from the ground with a cardboard and Styrofoam base, designed to minimize vibrations sympathetic with the rotating sample.

The cage rests on an array of four cinder blocks and wooden boards that lift it above a nitrogen cold load. The load, or bath as it will occasionally be referred, consists of a 25.7cm (10.5") by 58.8cm (24") by 73.5 (30") piece of Styrofoam. The center is hollowed out to a depth of 19.6cm (8"). This is then lined with mylar to prevent leakage. The lining is necessary as the Styrofoam is not strong enough to withstand the temperature differential when it is filled with liquid nitrogen; it cracks and becomes porous. The final layer in the bath is a double coating of 2.45cm (1") microwave absorber.

We use an optical gate (HOA1885-12) to trigger on the rotating disk (Figure 9). A small aluminum finger is attached to and extends from the underside

Figure 9. Optical gate used for triggering on the rotating sample.

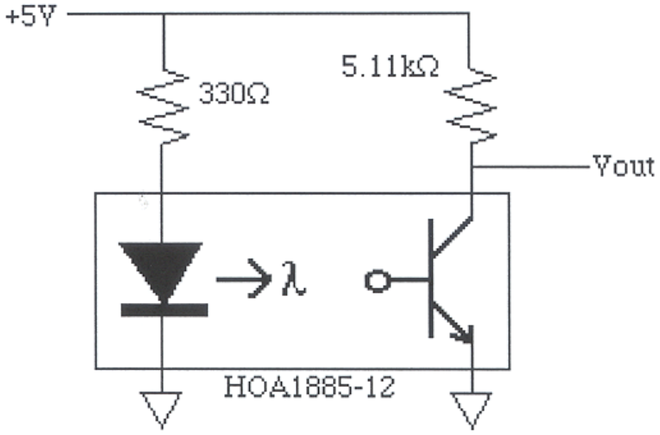

of the sample disk and passes through the gate once per rotation. When the gate is unblocked, a light-emitting diode forward biases the base-collection junction of a pnp transistor. Only a small portion of the +5V supply then reaches the circuit output terminal. When the gate is blocked, the base is at a higher voltage than the collector, no current flows through the transistor, and the output voltage increases to near 5V. We choose an input voltage of 5V so that the optical gate can be used as a digital trigger for TTL circuitry in the computer. (Section IIIc)

IIIb. The Radiometer

The following section describes the operation of each radiometer element in detail. A brief summary will provide a useful orientation. Consider Figure 10.

The feed-horn collects the thermal radiation from the sample like an antenna receives a radio signal. The horn is connected to the radiometer by an orthomode transducer and a mechanical switch. The OMT separates the two possible radiation polarization's onto two waveguide transmission lines, and the switch selects which then enters the next stage of the radiometer. Here the signal is multiplied by a reference signal from the local oscillator (LO) by the mixer. The mixer yields two signal components, one with a frequency that

Figure 10. Digital photograph and diagram of the radiometer.

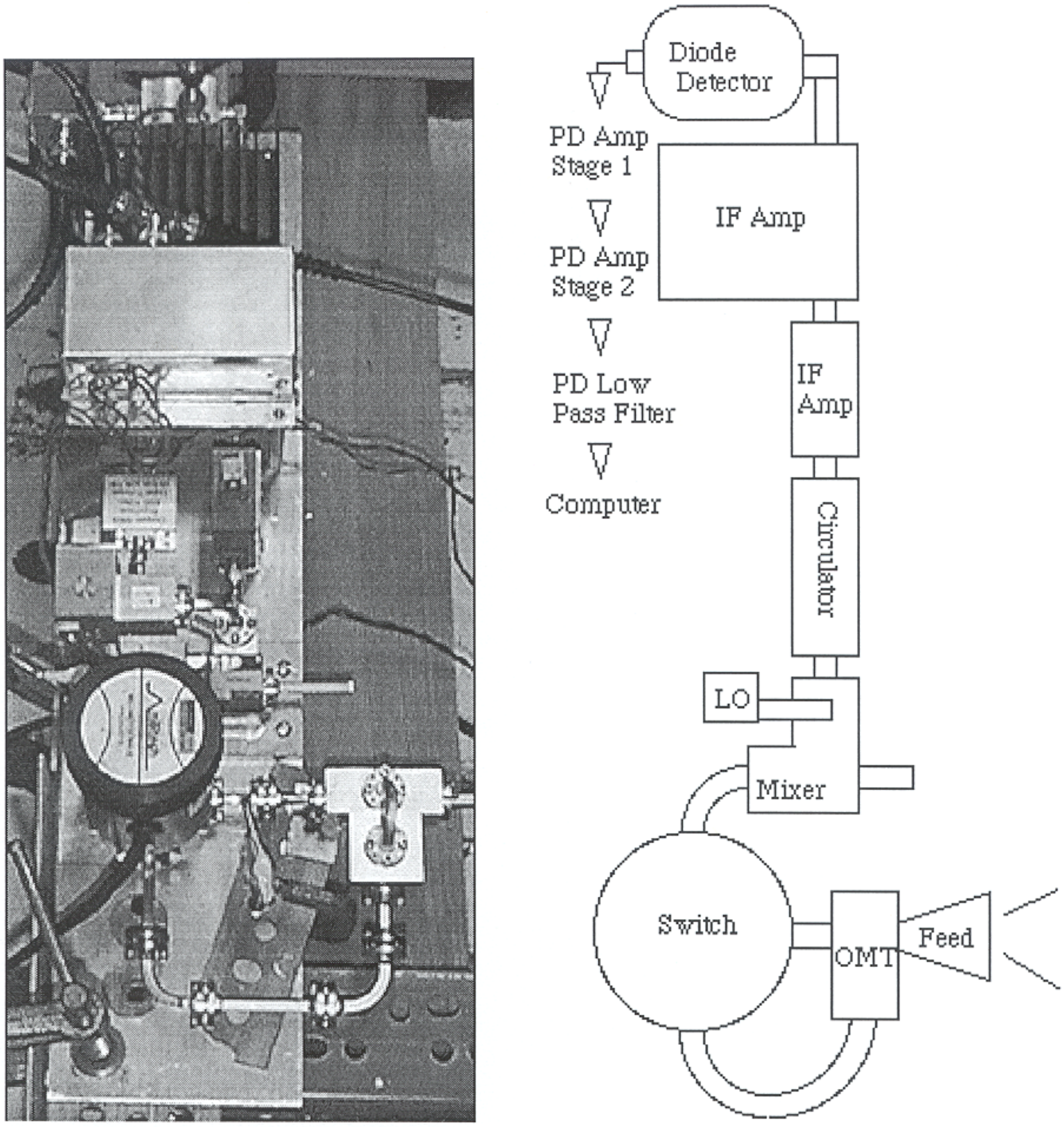

is the difference of the inputs and one that is the sum. The sum component cannot propagate through the coaxial line to the next stage. The circulator makes sure that nothing leaks back into the mixer. Continuing, the difference component gets amplified in an IF (intermediate frequency) gain stage. Next, the signal is demodulated in the diode detector. This converts the amplitude modulation of the signal to an easily analyzed DC voltage that is proportional to the input power. Finally, there are two post detection amplification stages.

The first provides a gain of 40dB. The second adds a DC voltage to cancel the DC portion of the post-detection signal and then amplifies it 26dB.

Each section of the radiometer is characterized by its action in the frequency domain on an input signal. Each also has a characteristic loss (reflecting its inefficiency) or gain measured in dB. There are two important types of loss that will be important. First is insertion loss IL. This is just an expression of the relative degree to which different parts of a circuit (i.e., the input and the output) vary in their ability to transmit a signal. Second is the return loss RL. This is a measure of how mismatched the load on the output is. If it is matched then all the available power is transferred. Otherwise, a portion of the signal gets reflected instead of transmitted. The return loss can also be expressed in terms of the voltage standing wave ratio VSWR. The conversion between VSWR and RL is:

$$RL = 20log\frac{VSWR-1}{VSWR+1}. \tag{37}$$

Values for the losses of each radiometer element are available from the data sheets in Appendix A.

An important question involving the loss of each circuit element is: given a particular input power, what is the output power? We can calculate this if given the RL and IL of the element. This in turn gives the total loss of the element. Consider, for example, a broadband signal centered around 90GHz with power 1W at the input of the OMT. We look at propagation straight through the OMT (i.e. the perpendicular polarization).

First, the isolation is given on the data sheet in the appendix (p.A10) as 26.26dB. This means that only one part in 423 of the incident signal power goes in the wrong direction, toward the side channel (i.e. the parallel polarization). Thus, we can ignore it.

Table 4. The gains and upper limit losses corresponding to each element of the pre-detection radiometer. There is approximately 26cm of waveguide attenuating at 1.3dB/m corresponding to data taken for the parallel polarization $E_{\|}$ and 8.75cm for the perpendicular polarization $E_{\perp}$. Data taken from tables in the appendix.

Radiometer Element	Gain/Loss $E_{\perp}$	Gain/Loss $E_{\|}$
OMT	$-0.9dB$	$-1.73dB$
Waveguide	$-0.51dB$	
Switch	$-0.87dB$	$-0.87dB$
Mixer	$-8dB$	$-8dB$
Circulator	$-0.81dB$	$-0.81dB$
Miteq Amp	$+36dB$	$+36dB$
Minicircuits Amp	$+25dB$	$+25dB$
Total	$49.91dB$	$48.06dB$

Continuing, we see that the RL is -16.83dB. Thus, $P \times 10^{RL/10}$ =20mW of the signal gets reflected, and the power available to go through the OMT is 0.98W. This now suffers an insertion loss of -0.81dB. The final power is then 0.81W. Finally we see that the overall loss is $10log(0.81/1) = -0.9$dB.

Table 4 contains values, calculated in this manner, for the losses of each radiometer element.

IIIb1. Feed Horn

We are using a feed designed by YRS associates for the MAP project. (Appendix A p.A7-A9) It operates over the W band (specifically, 82-106GHz) and is centered around 90GHz. Briefly summarizing the microwave properties of the feed, the forward gain at 90GHz is modeled to be 26.40dB. Measurements of the beam pattern (Appendix A p.A8, A9) show the peak power in the sidelobes is a factor of 10^4 down from the main lobe. Moreover, the main lobe is quite tight; the FWHM is 8.4°. This removes, to a large extent, problems arising from beam spill that previous feeds suffered from.

Briefly summarizing the feed's mechanical properties, the aperture diameter of the feed is 4.316cm. The length is 60.329cm. The length of the feed is necessitated by MAP satellite specifications and is made possible by corru-

Figure 11. Beam path for the Map corrugated feed horn. The geometric picture of what radiation is received by the radiometer suggests little beam spill-over into unwanted regions.

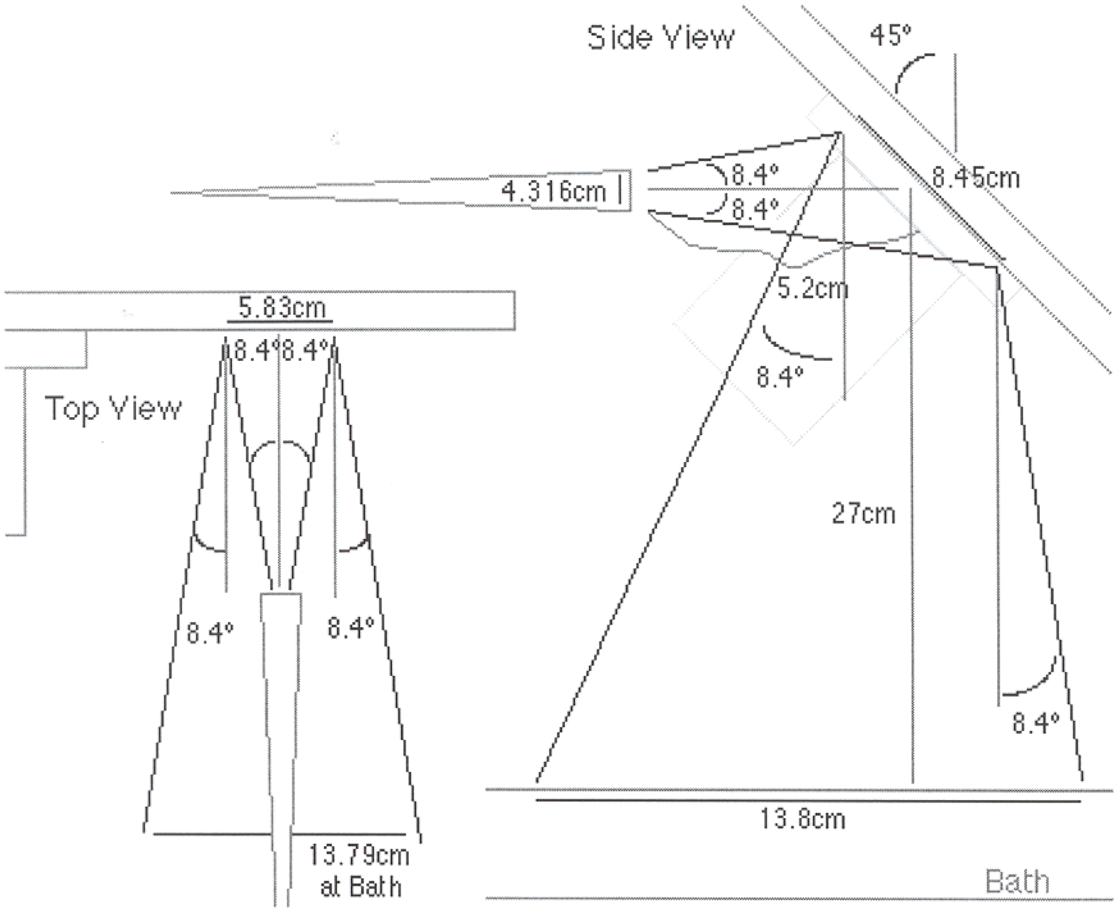

gating the interior of the feed. The corrugation also makes it possible to have a highly symmetric beam with small sidelobes and little loss.

Although the distance between the sample and the feed is only 5.21cm, much shorter than the 1.4 meters below which the far field description is no longer applicable, the FWHM beam angle gives us a useful picture of where the beam is roughly expected to be. Figure 11 shows a sketch of the beam path. Notice that the majority of the beam (in the far field limit) illuminates a small portion of the sample, neither straying toward the disk center or edge nor reflecting back onto the feed itself.

When the beam angle is approximately equal to 20°, the beam begins both to reflect back onto the feed itself and to see the edges of the bath below. From

20° to 180° the beam is then seeing 293K instead of 77K.

In Appendix A (p.A8, A9), there are two plots of the beam pattern. The first is a theoretical curve, the second contains both a theoretical curve and data points. The first shows the normalized gain (in dB) as a function of beam angle out to 180°. The second shows the gain relative to the gain of a spherical beam pattern. Both plots are in the far field limit.

Using the first of the two plots, we can get an estimate on how much of the beam power comes from room temperature radiation. At 20°, the feed gain is down 36dB. Therefore, the first time we see 293K, the gain is down by a factor of almost 4000. This makes 293K look like 70mK at the center of the beam. As signal variations this size correspond to (divide by 216K) emissivity differences on the order of 10^{-4}, they are just big enough to begin causing us problems.

These problems were quite evident early in the experiment, when we were using a small rectangular Millitech high gain feed horn with a larger FWHM beam angle (≈20°). Figure 12 shows a typical data set from that period. Here the effects of beam spill over onto the bolts holding the disk to the axle are clearly illustrated. The bolts, which are about 11cm left of beam center, would have come into the beam at an angle near 50°. There are four steel bolts and four corresponding dips, or emissivity increases, in the signal from the perpendicular polarization. The bolts appear in the perpendicular polarization rather than the parallel polarization due to the shape of feedhorn's beam pattern. The horn is rectangular, and the beam is wider in the direction corresponding to the polarization it is receiving.

To make certain that the signal from the disk near the axle was constant, an aluminum sleeve was machined to fit over the bolts in order to present a symmetrical and unchanging surface.

Figure 12. Data taken for the bulk aluminum disk in early October. Beam spill-over into unwanted regions is clearly indicated as the bolts holding the disk to the axle are present in the data. The sample here rotates flatly to within $245\mu m$ (0.01"). There were n =27000 iteration periods. The data was unfiltered and sampled at 1kHz. The calibration for both the parallel and perpendicular polarization is $16.9 \pm 0.2 mV/K$.

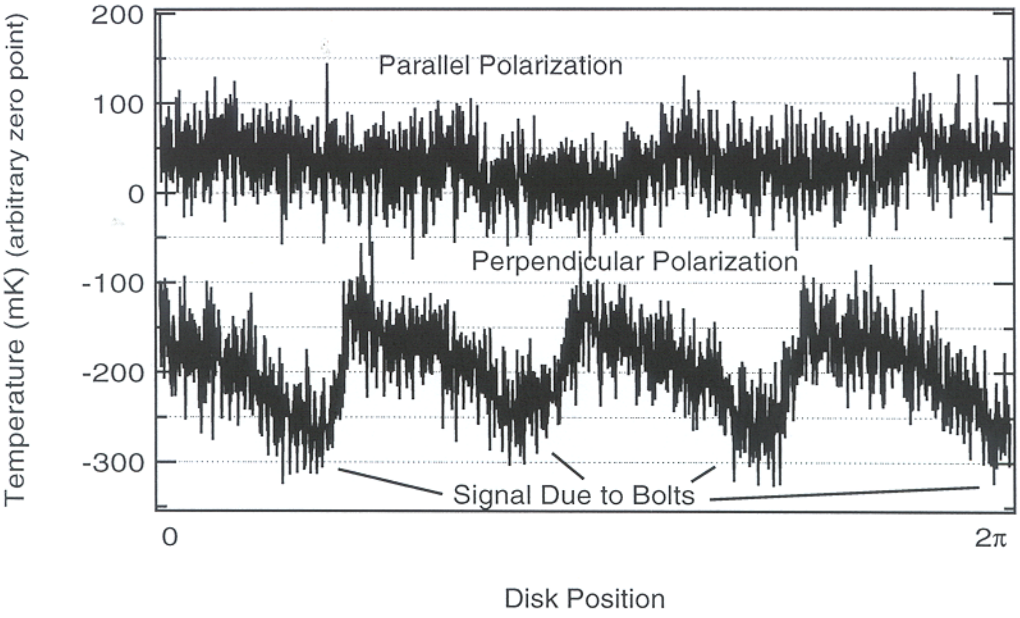

To keep variations in the disk edge, which for most samples is irregular and roughly milled, from contributing a synchronous signal, a shield of microwave absorber was mounted to the cage in front of the disk. This extends approximately one inch over the sample, remaining fixed to the cage as the disk rotates behind.

Late in October, we switched from the small Millitech feed to the longer corrugated standard gain feed discussed above. Even with the narrower beam, we have to be cautious. In the near field, a beam pattern becomes broader. We do not know exactly what the pattern will look like. Sidelobes will begin to play a larger role. To be safe, we retain the shield of microwave absorber around the disk and line the interior of the cage, around the bath, with microwave absorber to prevent signal reflection.

III2 OMT (Millitech CDC-10-01836)

The orthomode transducer takes the signal from the feed running through a circular transmission line and separates it into two channels. Radiation polarized parallel to the plane of reflection is passed directly through the OMT onto rectangular waveguide. The perpendicular polarization is passed through the side of the waveguide. The utility of the OMT comes from the fact that it makes it possible to look at both polarizations through the same feed without disconnecting and rotating it. It allows the switch to select between the separate polarizations at its input ports.

The design of the OMT requires much more waveguide to attach its side port than to attach its front port. Thus one of the polarization suffered an added loss in signal to noise due to transmission line loss. As we saw in the theory section, the signal in the parallel polarization is expected roughly to be twice as hot as that in the perpendicular polarization. Therefore, we run the parallel polarization out the lossier of the two lines. An effect of this is that the system calibration differs between the two polarizations. The data sheet and statistics for the OMT are in Appendix A. (p.A10)

IIIb3 W-Band Waveguide

The OMT is connected to the switch by WR-10 rectangular copper waveguide with dimensions a =0.254cm by b =0.127cm. The switch is also connected to the mixer by this waveguide. The dominant propagation mode, the TE_{10} mode, will thus have a cutoff frequency f_{co} of

$$f_{co} = \frac{c}{2a} = 59.01GHz. \tag{38}$$

(Pozar p.145) This is the mode with the E field pointing in perpendicular to the side of the waveguide with length b and parallel to the side of length a. From Appendix A, (p. A11) we see that the waveguide attenuation is 1.3 dB/m. Attenuation At is defined such that

$$W_{OUT} = W_{IN}(1 - 10^{\frac{-At\ in\ dB}{10}}). \tag{39}$$

From this, one can show that the loss in dB over a section of waveguide of length L, measured in meters, is:

$$Loss = -10L\,log(1 - 10^{-1.3/10}). \tag{40}$$

We use this to calculate the losses reported in Table 4.

IIIb4 Switch (Millitech MWS-10-0BP3W)

Of all the radiometer elements, the switch is the simplest to describe. It just rotates a waveguide flange between different input ports. It assembles waveguide like you would do if you had to disconnect and reconnect the feed horn every time you wanted to look at the other polarization. This is, however, very precise work. If waveguide is not lined up well, some of the signal gets reflected instead of transmitted.

The switch can either be operated manually or with an electronic driver. The driver runs at +28V and requires a large current, about 1A. The driver accepts logic levels in two channels to decide between the four switch positions.

IIIb5 Mixer (Millitech MXP-10-RSSXL) and LO (MWOC)

The fundamental circuit element at work in a mixer is the diode. As we will also need to discuss diodes when we get to the diode detector, a little background is necessary. The $V-I$ curve for a diode can be expressed in the general functional form:

$$I(V) = I_{\circ}(e^{\alpha V} - 1). \tag{41}$$

(Pozar p.595) Here $\alpha = q/nkT$, with q as the electron charge. The factor n is called the idealty factor and varies from 1.2 to 2 depending upon the structure of the diode. For the case of a small AC voltage v riding atop of a large DC offset $V_{\circ}$, equation (41) can be expanded to get

$$I(V) = I_{\circ} + i = I_{\circ} + vG_d + \frac{v^2}{2}G'_d + \cdots \tag{42}$$

where the G's are constants describing the impedance of the diode. Thus, we see that the diode response will be nonlinear in v.

There are two RF signals that enter the mixer. First is the broadband input signal from the feed-horn through the switch. Second is a 90GHz sine wave produced in the local oscillator (LO). Its form is

$$v_{LO}\,cos(\omega_{LO}t). \tag{43}$$

Let's imagine a component of the input signal at 92GHz. It would have the form

$$v_s\,cos(\omega_s t). \tag{44}$$

Plugging $v_{LO} + v_s$ into equation (42) yields three current terms. The first is just a DC offset. The second is linear in v. The third term is:

$$i = \frac{G'_d}{2}(v_s\,cos\,\omega_s t + v_{LO}\,cos\,\omega_{LO}t)^2. \tag{45}$$

After some trigonometric manipulation, this becomes

$$\begin{gathered} i = \frac{G'_d}{4}[v_s^2 + v_{LO}^2 + v + v_s^2\,cos\,2\omega_s t + v_{LO}^2\,cos\,2\omega_{LO} \\ + 2v_s v_{LO}\,sin(\omega_s - \omega_{LO})t + 2v_s v_{LO}\,sin(\omega_s + \omega_{LO})t]. \end{gathered} \tag{46}$$

We see that the mixer outputs DC terms and sinusoids at double the input frequencies, the sum of the input frequencies, and the difference of the input frequencies.

The transmission line out of the mixer is a coaxial line which rejects the high frequency components in equation (46). As a result, only the term with the intermediate frequency $\omega_{IF} \equiv \omega_s - \omega_{LO}$ makes it through. For the input signal we have chosen to look at, $\omega_{IF}/2\pi$ =2GHz. The mixer accepts all such input signal components between 92 and 94GHz. It also accepts a band this wide on the other side of the LO frequency. This is referred to as the image band. The result is a post mixer signal with an effective bandwidth of 4GHz. But this is not the whole story.

The mixer in our radiometer is a two port mixer, designed to receive two inputs as well as the LO. One of the ports, however, dead-ends into a waveguide termination. The return loss of this component is small (Appendix A p.A13); so it does not contribute an appreciable loss. But the mixer only gets half of the power that it expects. Therefore, although the non-rejection of the image band doubles the noise power, this effect cuts it in half, brings it back to normal. The attenuation is then just that given in Table 4. As the gain of the feed-horn is symmetric with respect to frequency around the LO frequency (Appendix A p.A14, A15), and as the mixer treats those bands similarly, there is no deleterious effect in not rejecting the image band.

The loss reported in Table 4 is referred to as conversion loss. It describes the ratio of available RF power that does not make it to IF frequencies. The conversion loss is a function of how well the impedance at the mixer ports has been matched. It depends strongly on the amount of power coming from the LO. Specifications for the mixer are in Appendix A. (p.A13) There is an 8dB loss as it converts RF signal to IF signals.

IIIb6 Local Oscillator (LO)

We use an LO designed and matched to our mixer by Millimeter-Wave Oscillator Company. The power supply is regulated to ensure a stable output. The power at 90GHz is 36mW and falls of steeply at higher and lower frequencies. Data sheets are in Appendix A. (p.A14, A15)

IIIb7 Circulator/Isolator (RYT 300037)

A circulator is a device with three ports between which the signal can pass only in certain directions. By capping one of the ports, the circulator functions as an isolator, allowing the signal to travel only in the forward direction. Thus, it allows no reflected portions from the IF amplifier to pass back into the mixer.

IIIb8 IF Amplifier 1 (Miteq AFD3-020040-15)

The next two stages of the radiometer are IF gain stages. The first is the Miteq amplifier with a gain of 36dB over 2–4GHz. The gain falls off sharply (Appendix A p.A18) at higher and lower frequencies. At 7.5GHz it is all the way down to 0.5dB. This sets the IF bandwidth for the system at approximately 2GHz.

IIIb9 IF Amplifier 2 (Minicircuits 2HL-10420)

This is another IF gain stage. The gain is 25dB. Thus the total IF gain of the IF system is 61 dB.

IIIb10 Diode Detector (HP 8472B, Low-Barrier Schottky Diode Detector)

At this point, we have an AC signal at the IF frequency (between 2 and 4GHz) which has a modulated amplitude. The power is proportional to the initial RF signal power. The modulation comes from two sources. A very slow and small modulation, the one we are looking for, is due to the change in emitted power from the sample over the course of one disk rotation. The much larger modulation is due to the overall sample and system noise. It comes from the fact that we have reduced the system bandwidth. The noise is still evenly distributed in the frequency domain (white noise), but it now has an amplitude with voltage v obeying a Rayleigh distribution

$$P(v) = \frac{v}{V_{eff}} e^{-v^2/2V_{eff}^2} \tag{47}$$

(Krauss p.7-5) with the effective voltage V_{eff} given by the rms noise voltage.

To see the effect the detector has on an IF signal modulated at a frequency ω_m, we can write the IF signal voltage as

$$v(t) = v_o(1 + m\, cos(\omega_m t))\, cos\, \omega_{IF} t \tag{48}$$

(Pozar p.598) where m is the normalized modulation amplitude. Plugging this form for v into equation (42) for the diode response yields, after a little trigonometry, three frequency components proportional to $v_\circ$ and eight components proportional to $v_\circ^2$. As we are interested in signal modulations much slower than the IF frequency, the components proportional to $v_\circ$ are all relatively high frequency ($\omega_{IF} \approx \omega_{IF} + \omega_m \approx \omega_{IF} - \omega_m \approx 2\pi(2GHz)$). There are both high and low frequency terms proportional to $v_\circ^2$ ($0, \omega_m, 2\omega_m, 2\omega_{IF}, 2\omega_{IF} \pm \omega_m$, and $2(\omega_{IF} \pm \omega_m)$). As long as we are operating over the section of the diode $V - I$ curve in which the v^2 term in equation (42) dominates , we don't have to worry about the high frequency terms proportional to v.

The resulting post-detection voltage v_{PD} across a load resistor R will have the form:

$$v_{PD} = R\frac{v_s^2}{4}G'_d\left[(1 + \frac{m^2}{2}) + 2m\,cos(\omega_m t) + \frac{m^2}{2}\,cos\,2\omega_m t + \cdots \text{ high frequency terms}\right]. \tag{49}$$

The output voltage is proportional to the square of the input voltage. This is referred to as "square law" behavior. When it is obeyed, the voltage at the output of the radiometer is directly proportional to the input power (and in turn, to the temperature).

From Appendix A, (p.A19) we see that our diode has certainly been operating over its square law range. From the "Sensitivity" specification on the data sheet, we see that as long as the output signal is less than 100mV, the output voltage is proportional to the input power. For even the hottest signal in this experiment, a room temperature load, the post-detection signal is typically only 20mV (with a 20μV rms).

The term in equation (49) that is the most important to us is the DC term which will change corresponding to variations in the sample emissivity with characteristic frequency ω_{DISK} ≈1Hz. To get to this component, we employ the detection scheme discussed in Section IVb.

IIIb11 Post-detection Amplification

The amount of gain needed in the IF amplifiers is dictated by two dueling factors. First, we need an overall system gain that will provide a large enough peak to peak voltage output to resolve the tiny temperature differences that we wish to measure at the radiometer input. Second, this gain cannot be so much that the diode detector saturates. We need it to be in its square law region so that antenna temperature variations manifest themselves as easily measured and calibrated voltage differences.

As an exercise, we can trace the evolution of a small input power as the signal goes through the radiometer. We will consider the signals in the perpendicular polarization and, for simplicity, will ignore the loss in the horn.

It is essential that we be able to measure emissivity differences to a few parts in 10^4. For a room temperature source, this implies $T_s \approx$30mK. This signal will be riding on top of the 77K reflected by the metal disks from the LN_2 bath. The power available from the sample is, from equation (30), $\Delta\nu_{IF} k T_{disk} = -83.7$dBm, where $\Delta\nu_{IF}$ =4GHz. From Table 4, we see that the resulting predetection power in the perpendicular polarization is -33.8dBm. For a typical diode detector, this falls within the square law region and corresponds to an output voltage of about 10μV. (Pozar p. 599) This is a small voltage and will require at least another 40dB of amplification.

We make up the rest of the system gain, 67.1dB, in two stages of post detection amplification. (Figure 12) After the diode detector, there is a shielded op amp circuit providing 40.2dB of gain. This stage also amplifies the DC offset coming from the diode detector which, as we make relative measurements, is unimportant. Moreover, its size can complicate the next and final stages in the setup, the analysis portion of the experiment. It can be too large for the low pass filter (see below), and it can be beyond the computer's input range. Therefore, the next amplification stage involves a summing amplifier.

Figure 12. Schematics for the post-detection amplification stages, labeled above in Figure 10 "PD Stage 1" and "PD Stage 2." All operational amplifiers are OP77EZ.

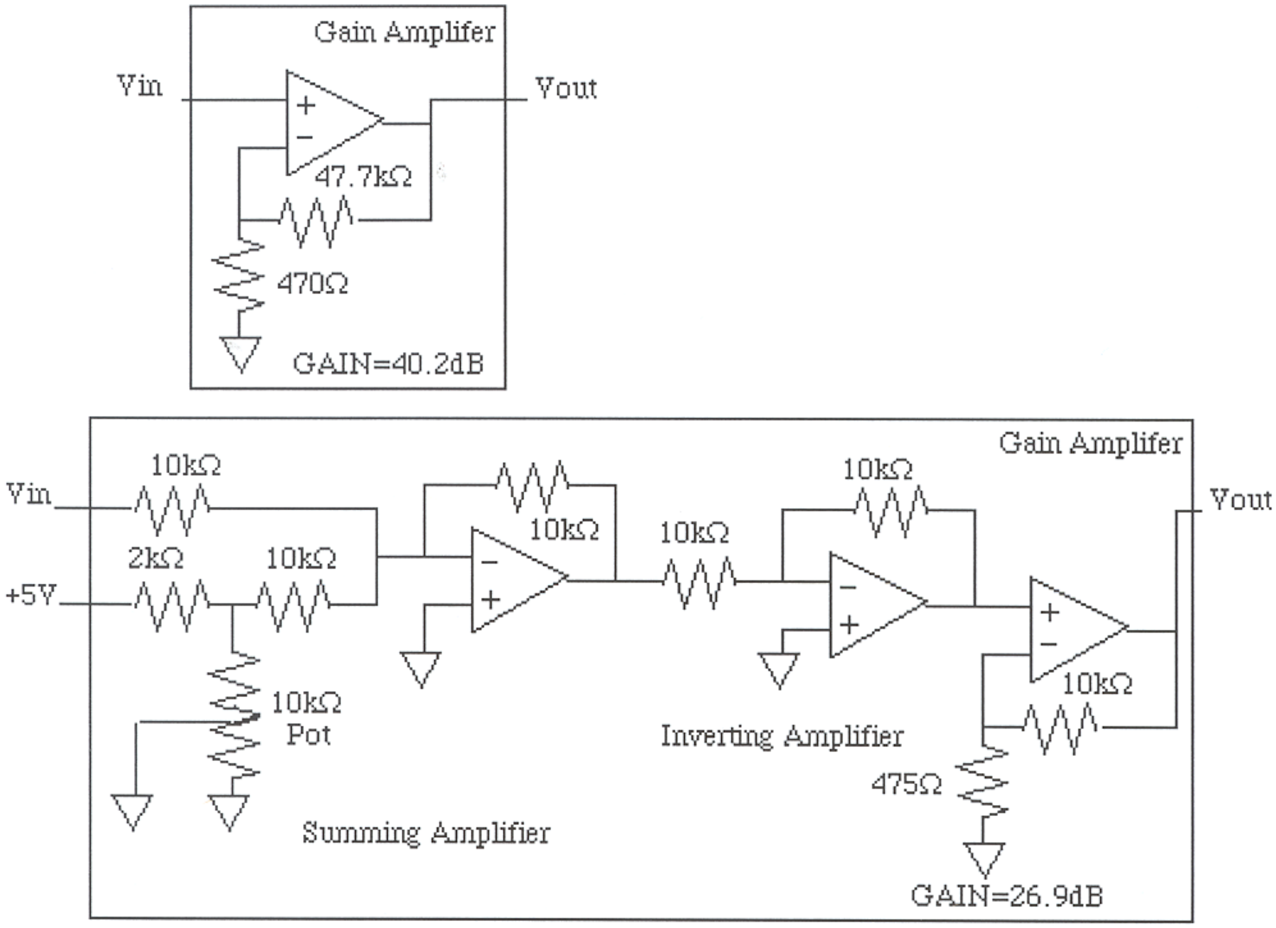

Controlled by a potentiometer, it adds a fraction of a 5V DC supply to bring the DC level (which is negative) toward zero. With the summing amp, there is an inverting amplifier necessitated by the inverting effect of the summing amplifier. Also, there is another gain amplifier, at 26.9dB.

IIIc. The Data System

After the radiometer, the signal goes to a Stanford low-noise preamp where it is low pass filtered. The importance of this stage is discussed in detail below. The effect is both to increase the signal to noise and to facilitate accurate signal sampling. The Stanford preamp overloads if the input signal is too large. The reduction in DC offset is provided in the summing amplifier discussed above.

The final stage in the experimental setup is a Dell Optiplex GXi Pentium computer running Lab View version 4.1. with a DAQ AT-MIO-16X data acquisition card. The computer and data acquisition software sample the signal out of the low pass filter. A running average of the co-added signal is kept. The computer interacts with the radiometer during data acquisition, telling the switch when to change positions. It keeps track of the number of data sweeps (disk rotations) and terminates after a preset number, saving the averaged data to file. The data are saved in millivolts. These are easily translated to Kelvin using the system calibration described in Section Vf4. The program performing all of the data operations is titled `mapscope.vi`.

IV. Noise, Sampling, and Synchronous Detection

As mentioned in Section IIb, the system temperature T_{sys} is far larger than the load temperature that we want to measure. We need a way of digging through the system noise to uncover the load variations. In the sections that follow, we first derive the form for the system sensitivity. This describes the amount of load variation we could measure if we looked just at the output of the detector. It turns out that this is 100 times larger than the temperature variations we wish to measure. Section IVb then describes the way in which we further trim down the system noise using synchronous detection. Finally, we address subtleties pertaining to and our application of synchronous detection.

IVa. System Temperature and Sensitivity

We saw in the last section that the detector outputs a DC voltage proportional to the input power. This signal will have several components. With the sample rotating once a second, there will be a voltage Δv varying at a frequency of 1Hz and harmonics. There will be unwanted signals coming into the horn from the sidelobes (spill). There will be a DC offset accounting for most of the system noise power. These signals can be characterized, as we saw in Section IIb, by effective temperatures. The total temperature T will be

$$T = T_{sys} + T_{disk} + T_{spill} + \cdots . \tag{50}$$

The total DC voltage v_{DC} at the output of the detector, which is proportional to the input power, will be

$$v_{DC} = \beta G k T \Delta\nu_{IF} \tag{51}$$

where we have used β for the proportionality constant. The pre-detection system gain is G.

We can now write an expression for the power output at the diode detector. We will use this in finding the system sensitivity. The DC signal power W_{DC}, proportional to the square of the voltage, will take the form

$$W_{DC} = K(\Delta T_L \Delta\nu_{IF})^2 \tag{52}$$

where K is a constant with units of action per temperature squared.

This will not, however, be the only power. There will be a power contribution from the AC components coming through the diode (equation (49)). These are due to high frequency noise components around the IF frequency beating with one another in the detector. (Krauss p.7-7) This produces low frequency noise components ν_{LF} with a triangular shaped power spectrum. Figure 13 shows a measurement of the power spectrum.

Writing the power density at the lowest frequency as W_ν, the total LF noise power is

$$W_{LF} = \frac{1}{2} W_\nu \Delta\nu_{IF}. \tag{53}$$

According to Evans (p.17), it can be shown that the total power in this LF component is equal to the total power in the DC component. The DC component is dominated by system noise, hence by the T_{sys} term in equation (50). Thus

$$W_\nu = 2KT_{sys}^2 \Delta\nu_{IF}. \tag{54}$$

Now let's consider the effects of the post detection circuitry in the radiometer and also the low pass filter following. There are two more gain stages after the detector. Denote the post detection gain G_{pd}. There is also a summing amplifier which adds the DC component mentioned above. Next, the low pass filter truncates the IF bandwidth to a much smaller bandwidth $\Delta\nu_{pd}$. There is, in our case, a post-detection low pass filter with $\Delta\nu = 2\pi/RC$ =300Hz. This is a two pole RC filter; the bandwidth $\Delta\nu_{pd}$ is then 1.22$\Delta\nu$=366Hz. (Krauss

p. 7-10) Over this small range, W_ν is approximately constant. The total LF noise power is then

$$W_{LF} = 2KG_{pd}T_{sys}^2\Delta\nu_{IF}\Delta\nu_{pd}. \tag{55}$$

We can now ask the question: what is the minimum detectable noise power in the total rms noise output that we could measure? We find the answer, termed the sensitivity $\Delta T_{L,\,min}$ by equating the noise and signal powers (equation (55) and equation (52) multiplied by G_{pd}):

$$\Delta T_{L,\,min} = T_{sys}\sqrt{\frac{2\Delta\nu_{pd}}{\Delta\nu_{IF}}}. \tag{56}$$

To use this equation, we first need to know the effective system noise temperature.

One way to measure T_{sys} is to determine the system output with a load at 0K. This is, of course, thermodynamically impossible to do directly. However, we can take advantage of the linear response of the system by measuring the power output at two known load temperatures. We can then draw a line connecting them and extrapolate down to 0K. This is termed the Y-factor method for reasons that will soon become apparent.

The loads we will look at are microwave absorber at room temperature (T_1 ≈293K) and microwave absorber immersed in liquid nitrogen (T_2 ≈77K). Calibrating the radiometer between these loads we found that approximately a 733mV voltage output difference corresponded to the 216K input difference. Denote this ratio, the system calibration, C. We will describe in detail how it is measured and the uncertainty involved in Section Vf4. We calculate here C =3.40±0.41mV/K.

Now if we define Y to be the ratio of the powers, we can solve for T_{sys}:

$$T_{sys} = \frac{T_1 - YT_2}{Y - 1}. \tag{57}$$

All the quantities on the left are measurable. We find Y by taking the ratio of the post-detector voltages. After taking six measurements, we found T_{sys} =12800±2000K. The error is so large due to the fact that our calibrations are uncertain to 12% (Section Vf4) Also, the fact that the Y value that went into equation (57) was only slightly different from unity makes equation (57) very sensitive to small variations in Y. As the denominator in equation (57) gets very large with Y near unity, any measurement error is greatly exaggerated. Ideally, one would want reference loads producing output powers that differed considerably more than the ones available here.

We can plug this value for T_{sys} into equation (56) to find the system sensitivity. As discussed in Section IIIb5, our mixer is double side-banded. This contributes another factor of 2 multiplying ν_{IF}. Therefore, using a 366Hz post-detection bandwidth, equation (56) gives $\Delta T_{L,\,min}$ =5.5±0.9K. We can check this number by actually measuring the rms voltage after the low passer filter. I measured v =15.5±0.5mV. This is consistent with the Y-value method prediction of 18.7±3.8mV.

There is another, more direct method for determining $\Delta T_{L,\,min}$. It involves taking the Fourier transform of the output signal. From Parseval's theorem, we know that the signal power expressed in the time domain is equal to the signal power expressed in the frequency domain. Denote a signal, measured in volts, by $h(t)$. Parseval's theorem states for the Fourier transform $H(\nu)$:

$$\int_{-\infty}^{\infty} |h(t)|^2 \, dt = \int_{-\infty}^{\infty} |H(\nu)|^2 \, d\nu. \tag{58}$$

In real life, integration over all time, or over an infinite bandwidth, would yield an infinite power. Thus we need to restrict integration to a finite time and bandwidth. It is necessary and sufficient to then speak of a power per unit bandwidth. We define the one-sided power spectral density $P(\nu)$ to be

$$P(\nu) \equiv |H(\nu)|^2 + |H(-\nu)|^2 \tag{59}$$

Figure 13. Power spectral density measurement at the radiometer output up to 10Hz. This is actually the square root of $P(\nu)$ with units Volts/$\sqrt{Hz}$. The top of the plot is at 1.99m$V/\sqrt{Hz}$ and there are 126$\mu V/\sqrt{Hz}$ per division.

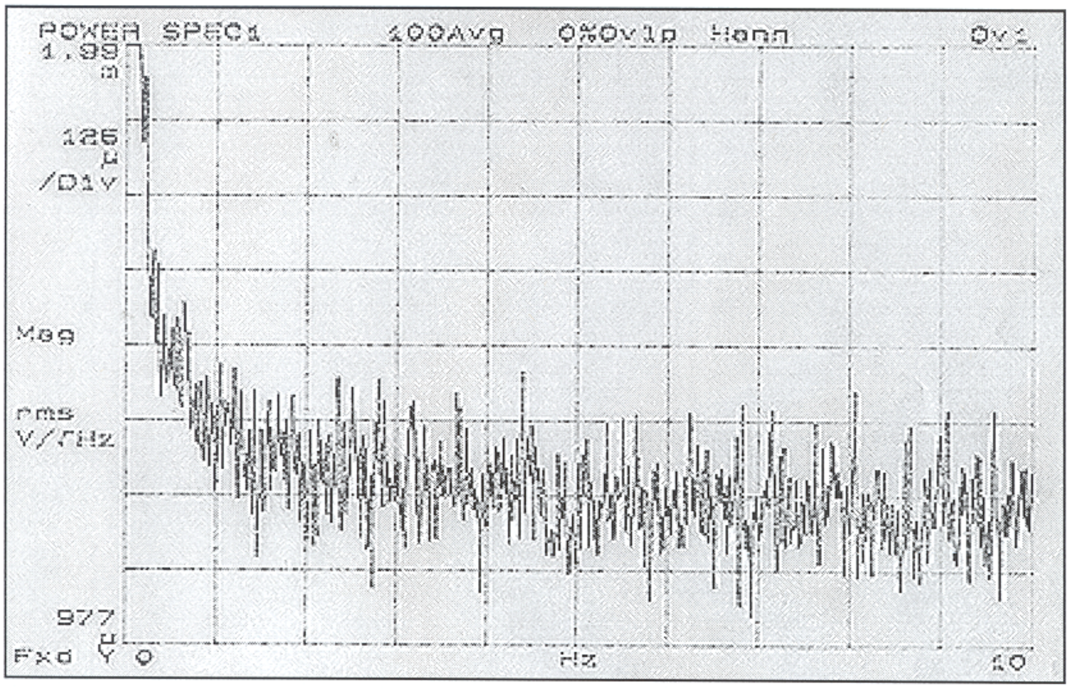

Table 5: Post-detector and low pass filter radiometer measurements for the perpendicular polarization. A post detection bandwidth of 366Hz was used.

Measurement	Temperature
T_{sys} (Y-factor)	$12800 \pm 2000K$
T_{sys} $(P(\nu))$	$15800 \pm 2000K$
$\Delta T_{L,\,min}$ (Y-factor)	5.5 ± 0.9K
$\Delta T_{L,\,min}$ $(P(\nu))$	6.8 ± 0.8K

such that

$$\frac{1}{T}\int_0^T |h(t)|^2\, dt = \int_0^{\nu_c} P(\nu)\, d\nu \tag{60}$$

where we integrate the power spectral density up to ν_c—the Nyquist critical frequency discussed in the next section. Unintegrated, $P(\nu)$ is the power in a particular bandwidth divided by that bandwidth. The system sensitivity in Volts is then just

$$\Delta T_{L,\,min} = \sqrt{P(\nu)} \times \sqrt{\Delta\nu_{pd}} \tag{61}$$

A device called a spectrum analyzer can be used to calculate $P(\nu)$. It uses an FFT (Fast Fourier Transform) algorithm to calculate the product of the

Fourier transform and its complex conjugate. Figure 13 shows a plot in volts per root Herz ($\sqrt{P(\nu)}$) as a function of frequency for our system. We see that $\sqrt{P(\nu)}$ levels off at high frequency. As we are interested in the power density below the frequencies at which we sample and filter, this is where we read off our number. From figure 13, $\sqrt{P(\nu)}$ =1.2±0.04mV/$\sqrt{\mathrm{Hz}}$. Therefore, we calculate T_{sys} from equation (56) as $\sqrt{P(\nu)}/C \times \sqrt{\nu_{IF}/2}$ =15800±2000K. Again, we use ν_{IF} =4GHz as our mixer is double side-banded. This value is consistent with the one calculated with the Y-factor method. Also, the sensitivity is, from equation (56) with $\Delta\nu_{pd}$ =366Hz, 6.8±0.8K. The data is summarized in Table 5.

IVb. Synchronous Detection

We hope to be able to measure load variations smaller than 100mK, corresponding to emissivity differences on the order of 10^{-4}. This is not possible with a direct measurement from the system. Above we saw that our sensitivity was as on the order of 1K. Therefore, we are detector noise limited, with a signal to noise of about one in one hundred. To reach the signal levels we desire, we must synchronously detect.

We want only the signal variations occurring on the timescale of a sample rotation at 1Hz. Therefore, we record the detector output every disk rotation, sum them all up after a long period, and divide by the number of cycles. Thus, we average the signal, averaging out the frequency components that look random because they change much faster than the detection period. The process is somewhat more complex, but that is the general picture.

To implement this scheme, we use a computer to sample and bin the post-detection signal. It does this every disk rotation, keeping track of the sum signal in each bin. Let us imagine that there are a total of n_N noise pulses on average per bin and n_s pulses of the signal we wish to measure per bin

Figure 14. Co-adding the detector output to eliminate non-synchronous noise. This is MAP VDA #1. The rms decreases like $n^{-1/2}$ *until the sample signal begins to dominate.*

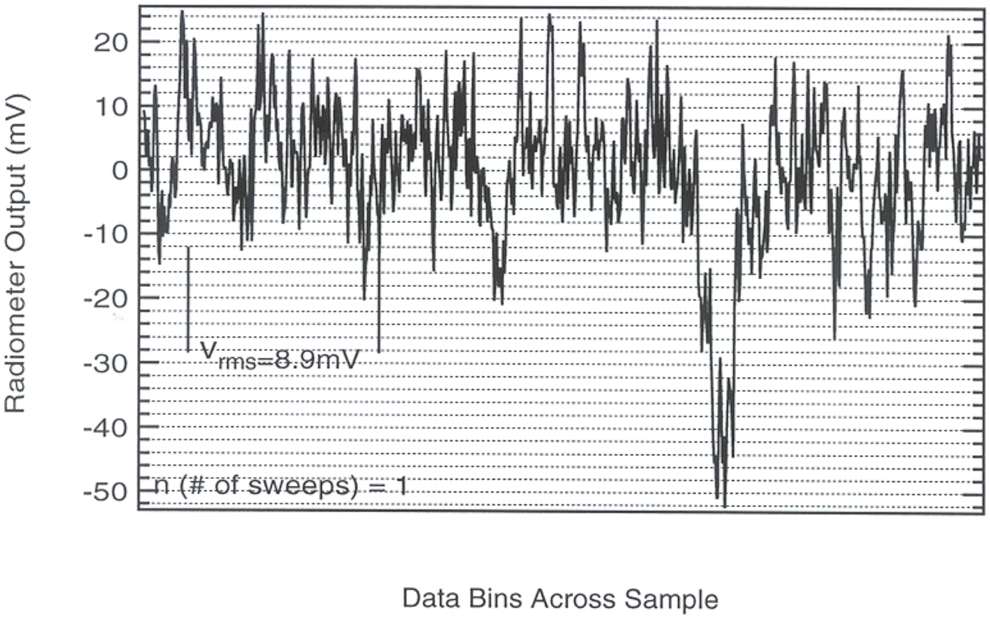

sampled by the computer every disk rotation. (Horowitz & Hill p.625) Also, $n_N >> n_s$. After one data sweep, the n_N pulses are distributed across the bins. The signal pulses will fall in specific bins and will continue to do so. The mean value of the noise signals that accumulates in each of these bins will be unimportant, manifesting itself as a nonvarying DC offset across all the bins. The fluctuations around the mean will, however, hide the signal. These increase in proportion to $n_N^{1/2}$. The signal to noise thus increases in proportion to the square root of the number of sampling cycles. If the signal to noise is initially 10^{-2}, then it takes 10^4 sampling periods to bring it to unity. Thus, we typically sample for 10^4 cycles in order to measure signal variations less than 100mK. The number of cycles n recorded during a measurement is reported with all data. Figures 14 through 17 display the averaging of the signal for MAP VDA #1.

This explains how white noise, the noise described by T_{sys}, is averaged out. Synchronously detecting the signal by co-adding disk rotations is also useful

Figure 15. Co-adding the detector output to eliminate non-synchronous noise.

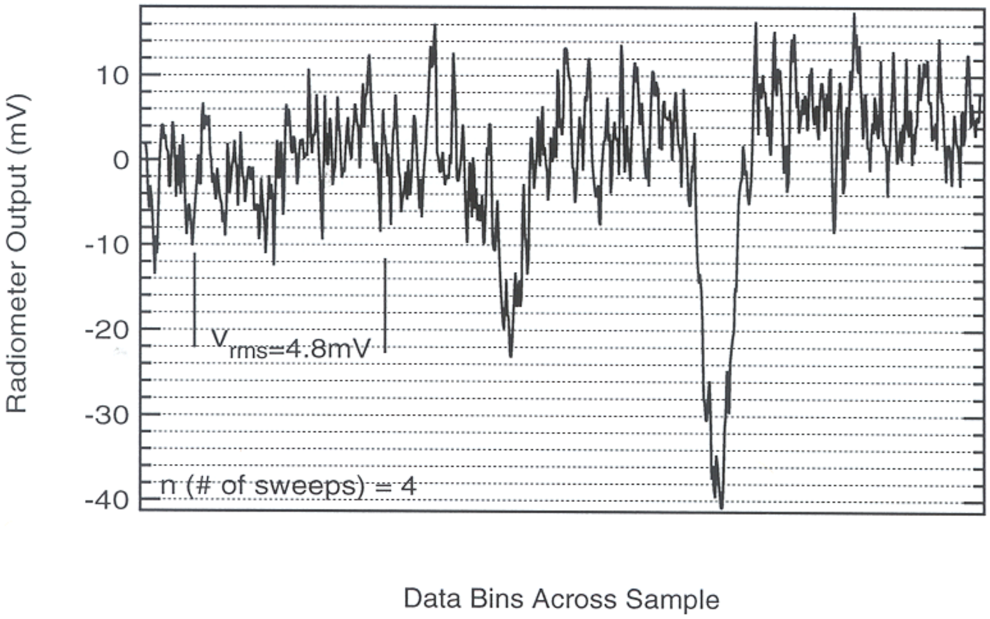

Figure 16. Co-adding the detector output to eliminate non-synchronous noise.

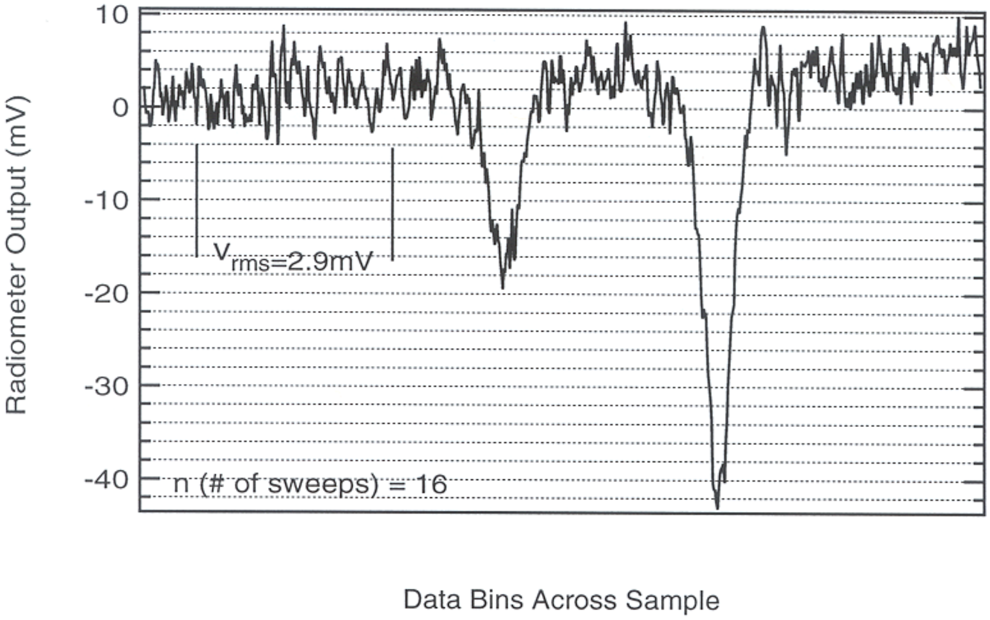

for eliminating unwanted signals at very definite frequencies (not equal to the chopping frequency). These are not averaged out as quickly as white noise. Consider an unwanted signal with period T present in the signal that we are chopping at a period T_D. This signal will bin constructively until, because it is changing at a rate different from the chopping rate, it will drift across

Figure 17. Co-adding the detector output to eliminate non-synchronous noise.

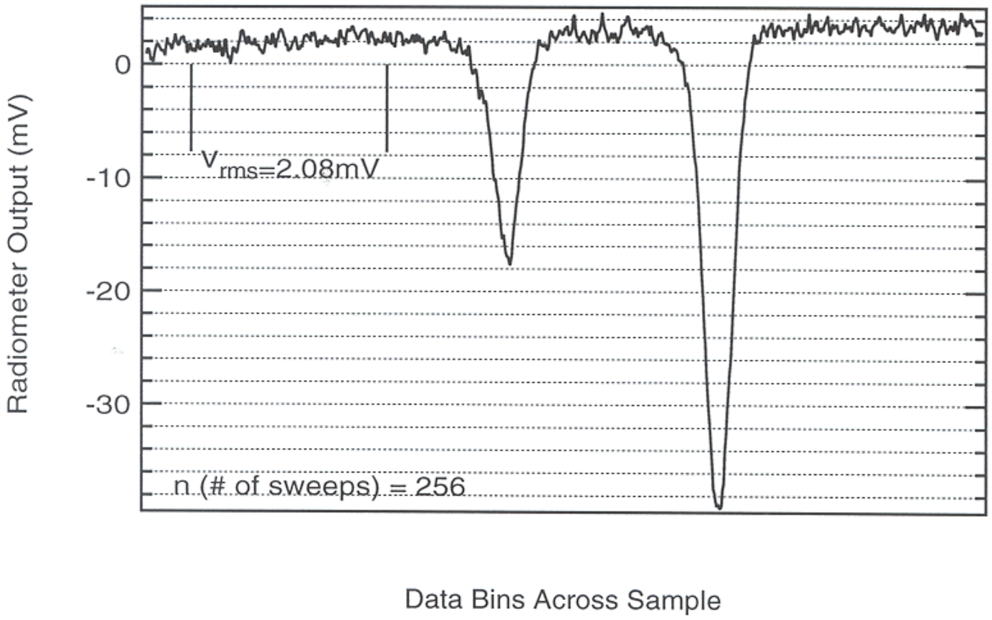

all the bins, spreading uniformly. The timescale over which this occurs is $(1/T_D - 1/T)^{-1}$. (Horowitz & Hill p. 627) Thus, all we have to do to get rid of this signal is wait long enough. Note that as the period of the spurious signal approaches the disk (chopping) period, this blows up. Expressed in this is the fact that if we could integrate the signal for an infinite amount of time, the bandwidth would be reduced to include only the chopping frequency. Thus, we see that synchronous detection is essentially a bandwidth reduction technique.

IVc. Sampling

There are some important subtleties involved in the sampling process that must be considered. These involve the sampling interval Δ (inverse of the number of bins per cycle) and its effect on whether or not, as we discretize the post-detection signal, we retain an amount of information adequate to describe it.

The typical number of samples taken across a data cycle in this experiment is about 1000. This was found to yield a continuous and smooth picture of the signal. The buffer has more than enough memory to hold this many samples and to keep a running tally of the sum per bin. For a disk rotating at 1Hz, 1000 samples corresponds to Δ =1ms.

When sampling, we have to be careful of two things. First, we need to bandwidth limit the post-detector signal to below the Nyquist critical frequency:

$$\nu_c \equiv \frac{1}{2\Delta}. \tag{62}$$

Second, we have to be aware that bandwidth limiting the signal causes it to become correlated.

The sampling theorem states that if you take a continuos function $h(t)$ and sample it at an interval Δ, then $h(t)$ is *completely determined* as long as $h(t)$ is limited to a bandwidth below ν_c. (Press et al. p.501) If the bandwidth is not limited to below ν_c, then all the signal power at higher frequencies gets aliased back into the frequency range $-\nu_c < \nu < \nu_c$. Therefore, if you thought you were just looking at signals within this frequency range, you would have more power than you could account for.

Moreover, when you low-pass filter a sampled signal, sampled data that is closer together in time than $2/\Delta\nu_{pd}$ becomes correlated, where $\Delta\nu_{pd}$ is the filter bandwidth and the factor of 2 is due to the Nyquist criterion. This just means that you cannot expect to sample faster than the signal is changing.

The filter we use to bandwidth limit the signal is a two pole RC filter ($\Delta\nu_{IF} = 1.22\Delta\nu_{3dB}$) as stated above. Along with all data, values for the sampling rate and filter 3dB point are reported.

For data taken before February, samples were rotated slowly enough that 500 samples per second was sufficient to characterize surface temperature variations. This sampled data was filtered below ν_c =250Hz at a frequency of 100Hz. Approximately every two data points are then correlated.

For the later data in this experiment, in which it was wished to make measurements as fast as possible to minimize the effects of slowly varying system temperatures, the sample rotation rate and the sampling rate were increased. These data were sampled 1000 times a second and filtered at 300Hz. A larger filter value was needed so that sampled signal was smooth and continuous. Here, approximately every 1.4 data points are correlated.

IVd. Methodology for Data Analysis

We are now in a position to run valid statistical tests on the data. The general procedure for calculating Δe values is as follows. Consider, Figure 18. The unprocessed data is in gray. We start by binning the data into groups larger than the number of correlated data points. We are over-cautious. Bins, unless otherwise noted, contain fifteen data points each. Next, we get a tentative idea of the error for each of these bins using the standard deviation divided by the square root of the number of uncorrelated data points in the bin. This is the tightest possible uncertainty. We then increase this uncertainty based upon the system baseline uncertainty.

We establish the system baseline before each measurement group using the flat aluminum disk. We define the system baseline uncertainty as the size of the error bars needed for this data to fit to a flat straight line with $\chi^2/\nu = 1$. Here χ^2 is defined to be

$$\chi^2 = \sum_{n=1}^{N} \left(\frac{x_i - \bar{x}}{\sigma_i} \right)^2 \qquad (63)$$

where $\bar{x}$ is the bin average and σ_i is the error which we vary until $\chi^2/\nu = 1$. For a good fit, χ^2 should be approximately equal to the number of data point (bins). The reduced χ^2, which is just χ^2 divided by the number of degrees of freedom ν, or data points when all the bins are independent, should be equal to unity.

Figure 18. Data for MAP VDA #1, Early. 10/31/97 The temperature scale is inverted. The disk is flat to 245μm. Data was taken for n=10000 sweeps per polarization and sampled at 500Hz with a 100Hz low pass filter. The calibrations are: Parallel (top graph), Perpendicular (bottom) 5.10±0.61mV/K. This is the first run of MAP VDA #1, prior to the installation of the OMT.

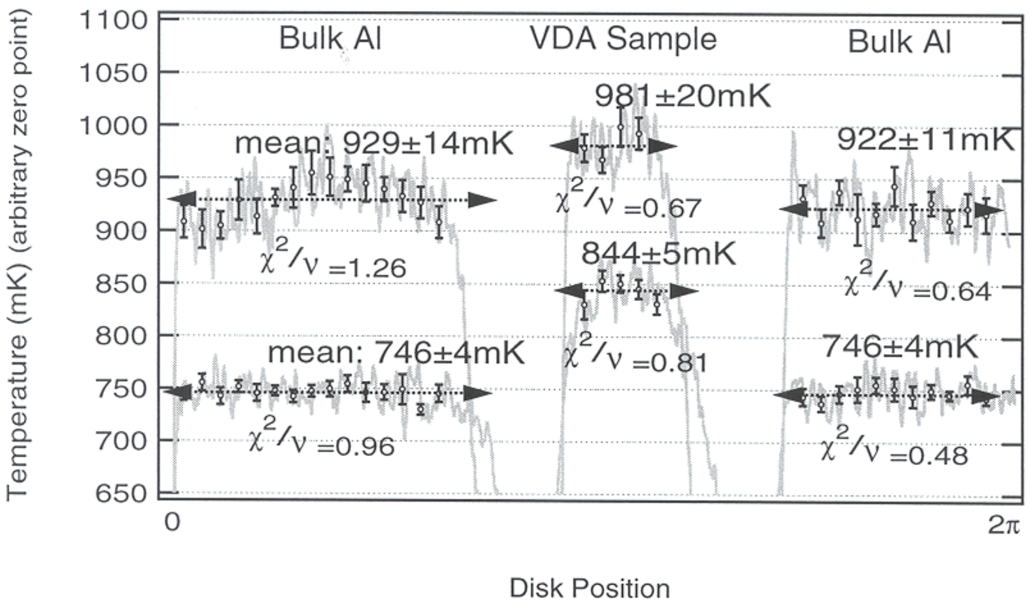

This uncertainty automatically takes into account both the statistical uncertainty and any systematic uncertainty that would affect the flat aluminum disk. For example, it includes the systematic uncertainty due to the relative unflatness of the sample disk, discussed in Section Vf1. Systematic effects not represented by the baseline are discussed in Sections Vf2–Ve6.

For an example of a flat aluminum disk with which we determine the system baseline, look ahead to Figure 23 on page 58.

After lengthening all error bars until they are as long as the system baseline error bars, we gauge by the positioning of the bins which need to be thrown out. In Figure 18, we have thrown out all bins near the dips due to the tape. The width of the signal due to the tape is estimated using $\pi/5$ radians as the beam width in units of the disk rotation angle. We determine this width in Section Vf2.

Continuing, imagine we wish to know the emissivity difference between aluminum and the MAP VDA sample in the parallel polarization in Figure 18. For each section of the data, we perform a weighted average over all of the bins to get the most representative emissivity. We present the reduced chi-squared values for each section as an indicator of the accuracy of this average. Should this reduced chi-squared be much greater than unity, we would either increases the size of the error bars or, if only certain sections of the data look much worse than others, decide to throw the data out entirely.

We calculate the average aluminum emissivity by averaging the two aluminum sections on either side of the MAP VDA sample. Then we subtract this from the MAP VDA sample mean to get the average temperature difference. This makes certain that the difference measurement weights the aluminum portions (of the disk on which the sample is mounted) equally. We find for the temperature difference -56±33mK. The emissivity difference is this temperature difference divided by 293-77K. We find $\Delta e = -2.57 \pm 1.53 \times 10^{-4}$.

The uncertainty will be increased in later sections.

V. Experiment and Results

The measurements made during the course of this experiment fall chronologically into four groupings—Early, Series 1, Greenbank, and Series 2. Interspersed with these are a number of tests to uncover systematic effects. Early are all those data taken before the final experimental setup was established in early January. This is not to say that these data are less reliable than later data. During this period, as addressed in Section Vf, many systematic effects were discovered and eliminated. Once the final and most sensitive experimental setup was established, data were taken in two cycles. Series 1, and Series 2 after it, were multiple data runs focusing on the MAP VDA samples. Each were taken over a short period ($\sim$ 1 week), in which the apparatus was kept as constant and unchanging as possible. Greenbank was another such cycle in which the sample from the Greenbank telescope reflector was measured.

All data groupings (except those in Early) contain a measurement of the emission pattern from a plain aluminum disk. This establishes the system baseline. Here we check to see that the sample signal is independent of rotation angle. The majority of the systematic effects discovered were found from plain aluminum disk measurements in which the signal was not observed be flat across the sample. Error bars for all data in a particular series are set using the data from the plain aluminum disk as discussed in the last section (IVd).

We will now list, chronologically by grouping, all measurements made along with the location of the respective plots and discussions in this paper.

Early: $\leq$ 1/7/98

- 9/2/97 Cu-Al-SS. Section Vf4.
- 9/2/97 Bulk Al Disk. Section IIIb1.
- 10/31/97 MAP VDA #1. Sections Ia, IVd, Va.

- 12/10/97 MAP VDA #1. Section Va.
- 11/14/97 +490μm Raised Al. Section Vf6.
- 1/6/98 MAP VDA #2. Section Va.
- 1/7/98 MAP VDA #2. Section Va.

Analysis of Disk Flatness

- 11/14/97 Bulk Al Disk. Section Vf1.

Series 1: 1/16/98–1/22/98

- 1/16/98 +490μm Raised SS. Section Vf6.
- 1/16/98 MAP VDA #2. Section Vb.
- 1/17/98 MAP VDA #1. Section Vb.
- 1/17/98 +490μm Raised Al. Section Vf6.
- 1/19/98 -245μm Lowered Al (with polyester tape over sample edges). Sections Vf5,6.
- 1/19/98 -245μm Lowered Al. Section Vf5.
- 1/20/98 Cu-Al-SS (with polyester tape over sample edges). Sections Vf4,5.
- 1/21/98 Cu-Al-SS. Sections Vf4,5.
- 1/22/98 Bulk Al Disk (with polyester tape). Section Vf5.
- 1/22/98 Bulk Al Disk. Sections Vb, Vf5.

Polarization Check

- 2/10/98 Bulk Al Disk (with Carbon Fiber thread in three orientations). Section Vf2.

Greenbank Telescope: 2/19/98–2/25/98

- 2/19/98 Bulk Al Disk. Section Vd.
- 2/20/98 Greenbank Sample. Section Vd.
- 2/24/98 Bulk Al Disk (parallel polarization only). Section Vd.
- 2/25/98 Greenbank Sample. Section Vd.

Series 2: 3/3/98–3/9/98

- 3/3/98 Bulk Al Disk. Section Vc.
- 3/4/98 MAP VDA #1. Section Vc.
- 3/4/98 MAP VDA #2. Section Vc.

- 3/5/98 Cu-Al-SS. Section Vf4.
- 3/9/98 Bulk Al Disk. Section Vc.

Rotated Polarizations Test

- 3/10/98 Bulk Al Disk. Section Vf3.
- 3/11/98 MAP VDA #1. Section Vf3.
- 3/11/98 MAP VDA #2. Section Vf3.
- 3/14/98 Cu-Al-SS. Section Vf3.
- 3/15/98 Bulk Al Disk. Section Vf3.

Chopped Carbon Fiber Thread Measurements

- 3/24/98 Bulk Al Disk (with different lengths and orientations of carbon fiber thread attached with spray-on adhesive). Section Ve.

Figure 18. Data for MAP VDA #1, Early. 10/31/97 The temperature scale is inverted. The disk is flat to 245μm. Data was taken for n=10000 sweeps per polarization and sampled at 500Hz with a 100Hz low pass filter. The disk is rotating at 3/5Hz. The calibrations are: Parallel (top graph), Perpendicular (bottom) 5.10±0.61mV/K. This is the first run of MAP VDA #1, prior to the installation of the OMT.

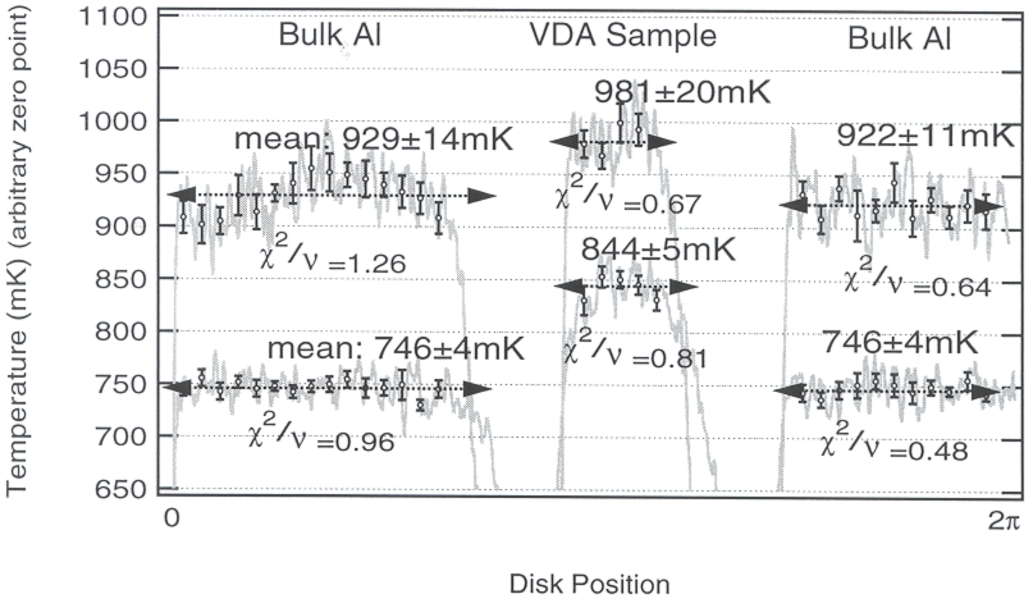

Va. Early

All measurements performed before January 7th, 1998 fall under the subheading early. These include the two measurements of MAP VDA #1 in Figures 19 and 20. The first measurement, that in Figure 19, was performed prior to the installation of the OMT. All other reflector measurement are performed with the OMT. The two measurement of MAP VDA #2 in Figures 21 and 22 also fall under the category Early.

There was no system baseline measured during this period. Therefore we use the largest uncertainty suggested by future baselines. We scale all statistical error bars by at least 2.93 for the parallel polarization and at least 3.1 for the perpendicular polarization, as discussed in Section IVd.

Calculated emissivity differences for the MAP VDA samples is displayed in Table 6. Uncertainties do not include those discussed below in Sections Vf.

During this time period, we also examined two systematic effects. First,

Figure 19. Data for MAP VDA #1, Early. 12/10/97 The temperature scale is inverted. The disk is flat to 245μm. Data taken for n =10000 sweeps at a sample rate of 500Hz. It was then low pass-filtered at 100Hz. The disk is rotating at 3/5Hz. Calibrations are: Parallel (top graph) 2.78±0.33mV/K, Perpendicular (bottom) 4.17±0.50mV/K. This is the second, first with the OMT, run of MAP VDA #1. The OMT is used for the rest of MAP VDA #1 data.

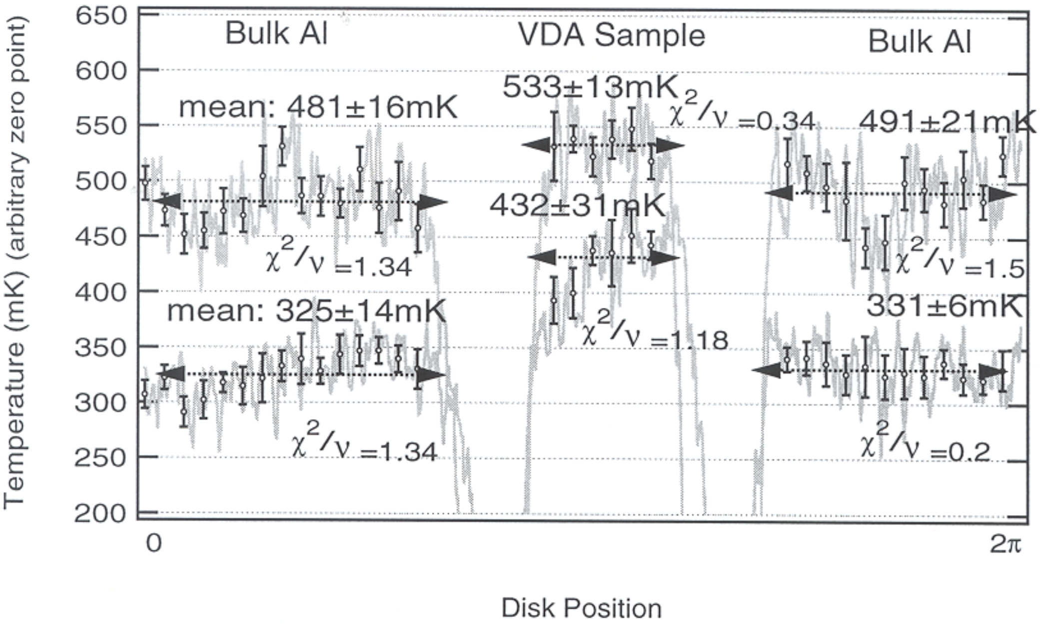

we quantified the effects of disk flatness, as discussed below in Section Vf1. Second, we began to examine the effects of the sample not being flush with the surrounding aluminum, as discussed below in section Vf6.

Figure 20. Data for MAP VDA #2, Early. 1/6/98 The temperature scale is inverted. The disk is flat to 368μm. Data taken for n =3600 sweeps and sampled at 500Hz. Data Filtered at 100Hz. The disk is rotating at 5/8Hz. Calibrations: Parallel (top graph) 2.78±0.33mV/K, Perpendicular (bottom) 4.40±0.53mV/K This is the first run of MAP VDA #2. The OMT is used here and for the rest of MAP VDA #2 data.

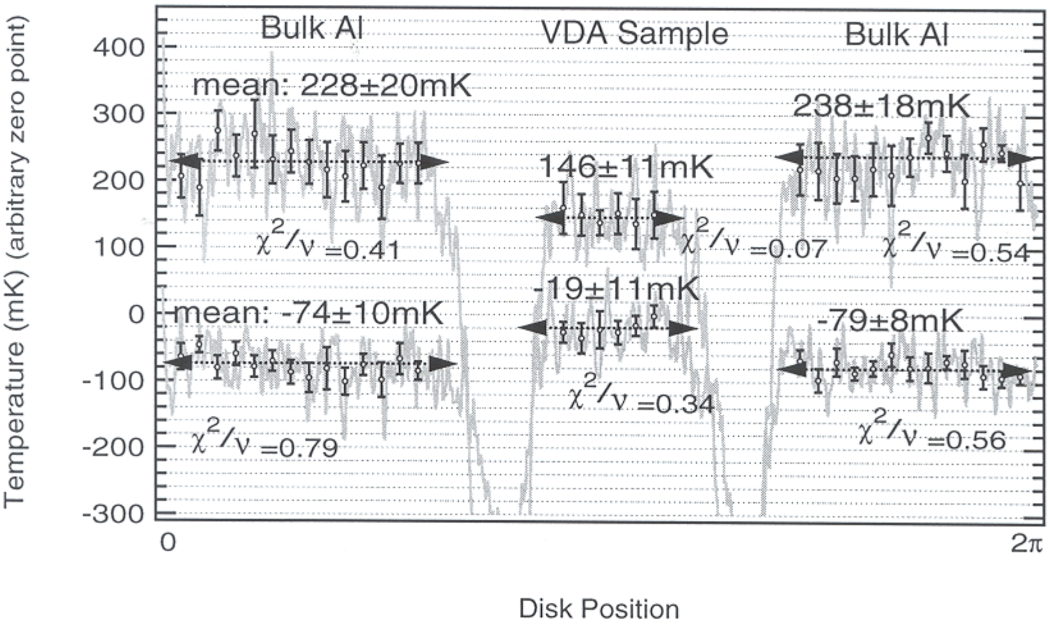

Figure 21. Data for MAP VDA #2, Early. 1/7/98 The temperature scale is inverted. The disk is flat to 398μm. Data taken for n =19800 sweeps, sampled at 500Hz, and filtered at 100Hz. The disk is rotating at 2/3Hz. Calibrations: Parallel (top graph) 2.78±0.33mV/K, Perpendicular (bottom) 4.40±0.53mV/K This the second run, first with a long integration period, of MAP VDA #2.

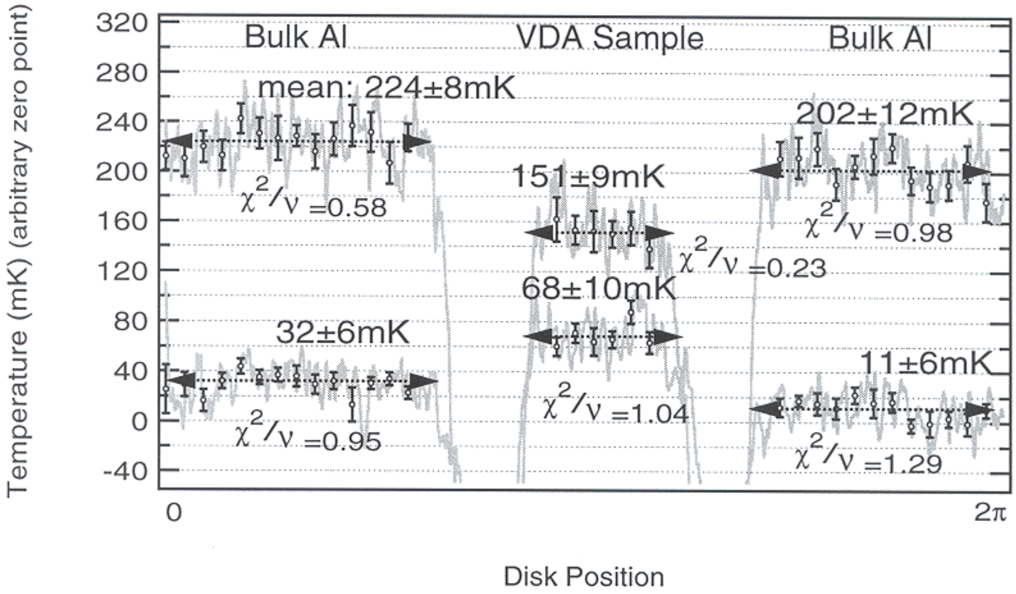

Table 6: Emissivities relative to bulk aluminum (6061-T6). $(e - e_{Al}) \times 10^4$. *A minus sign denotes less emissive than the aluminum.* $E_{\|}$ *denotes the parallel polarization and* $E_{\perp}$ *denotes the perpendicular polarization.*

MAP VDA #1.

Date	$E_{\|}$	$E_{\perp}$
10/31/97	-2.59 ± 1.53	-4.53 ± 0.42
12/10/97	-2.18 ± 1.48	-4.81 ± 1.90

MAP VDA #2.

Date	$E_{\|}$	$E_{\perp}$
1/6/98	4.03 ± 1.39	-2.69 ± 0.93
1/7/98	2.87 ± 0.88	-2.18 ± 0.74

Vb. Series 1

The first of two grouping of related measurements was performed in mid to late January of 1998. This collection of ten measurements, which we label Series 1, was assembled over a period of six days with as little alteration of the apparatus as possible. The only alterations that occurred between trials were the detachment and reattachment of the feed and the microwave absorber shield around the disk edge. These were necessary in order to change samples. Reattachment of the microwave absorber shield was done meticulously, making certain that no outer disk edge was visible to the feed. Likewise the horn was consistently returned to position. It was kept at a constant distance of 5.2cm from the sample.

Figure 23 shows the baseline for Series 1. We scale all statistical error bars by at least 2.93 for the parallel polarization and at least 3.1 for the perpendicular polarization, as discussed in Section IVd.

In Series 1, we examine two possible systematic effects. The first is the effect of a raised or lowered sample, of the proximity of the sample to the feed, on the sample emissivity. The two MAP VDA samples are slightly higher than the bulk aluminum around them (+120μm for MAP VDA #1, 25μm for MAP VDA #2). Next we attempt to quantify the amount to which the tape (that extends radially outward from the disk center, holding a particular sample in place) affects the emission pattern over a sample.

At the heart of Series 1 are measurements of the two MAP VDA samples and systematic checks to quantify their significance. Figure 24 shows the data for MAP VDA #1 and Figure 25 shows the data for MAP VDA #2.

The measurement here of MAP VDA #1 yielded emissivities differences less than all other measured values by a factor of two. The data over the sample, especially in the perpendicular polarization was far from flat. Note

Figure 23. Baseline for Series 1. Bulk Al Disk (6061-T6), Series 1. 1/22/98 The disk is flat to 245μm. Distance, feed to sample: 5.2cm. Data was taken for $n = 7200$ sweeps, sampled at 500Hz, and filtered at 100Hz. The rotation frequency of the disk is 0.66Hz. Calibrations: Parallel (top graph) 2.39±0.29mV/K, Perpendicular (bottom) 4.02±0.48mV/K

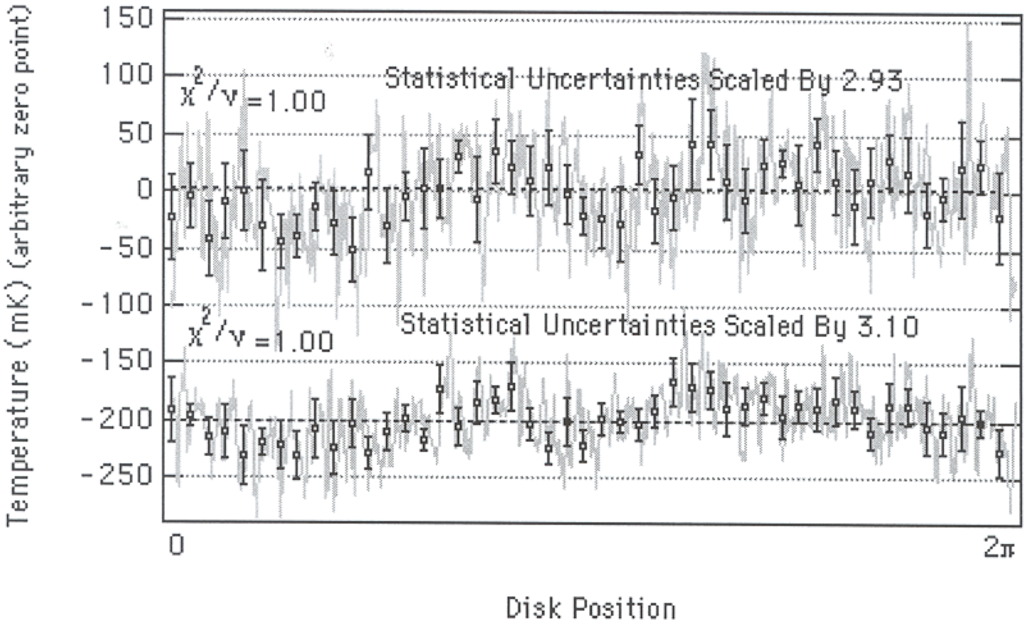

the large χ^2/ν value in Figure 24.

We examined several possible explanations for this behavior. We covered with microwave absorber every surface near the feed to be certain the beam was under control. This included attaching a sleeve of microwave absorber around the disk axle. These measures had no effect.

Continuing, we made certain that the disk was flat (to 245μm) on the axle and that it was rotating smoothly. This involved re-shimming the disk and had no effect. Finally, we checked to see that the sample was attached firmly and flatly to the aluminum disk. This implicated the polyester tape as a possible source of the increased signal.

We explore in detail the effects of tape below. We find no evidence that it could have caused the emissivity decrease for this measurement of MAP VDA #1.

As the results of this measurement varied so much from the rest, and

Figure 24. Data for MAP VDA #1, Series 1. 1/17/98 The temperature scale is inverted. The disk is flat to 98µm. The distance from the feed to the sample is 5.2cm. Data taken for n =8400, sampled at 500Hz, and filtered at 100Hz. The rotation frequency of the disk is 2/3Hz. Calibrations: Parallel (top graph) 2.55±0.31mV/K, Perpendicular (bottom) 3.94±0.47mV/K This is the third run of MAP VDA #1, first in a series format.

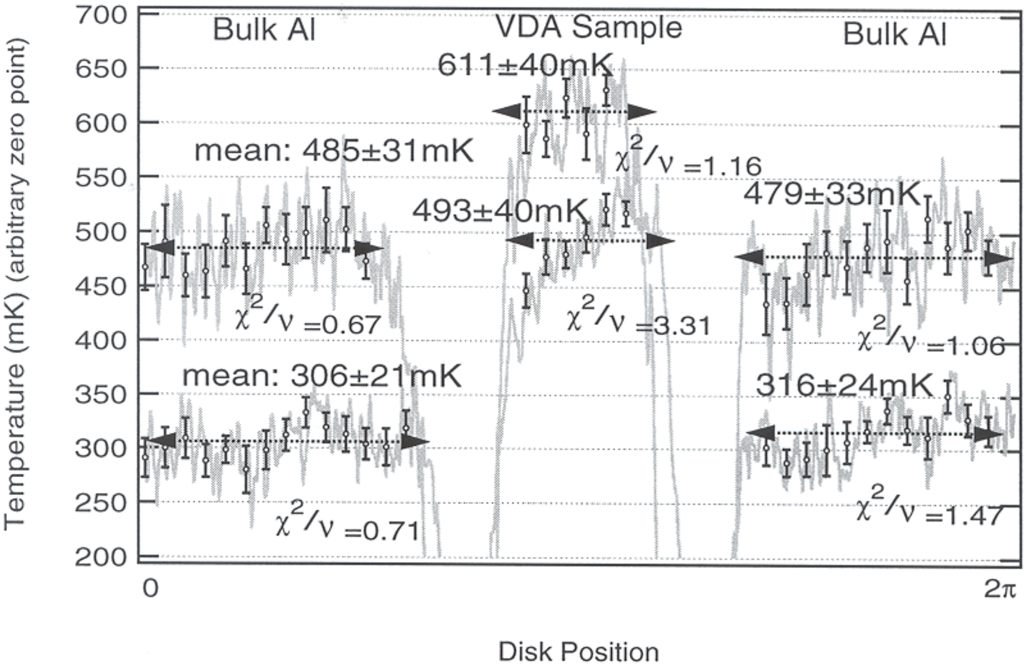

as later measurements returned values consistent with those previous after a series of systematic adjustments, we assume this measurement to be erroneous. We thus reject it.

Emissivity difference values for the two MAP VDA samples are displayed in Table 7. The uncertainty here does not include the corrections discussed in Sections Vf.

Figure 25. Data for MAP VDA #2, Series 1. 1/16/98 The temperature scale is inverted. The disk is flat to 245μm. Distance, feed to sample: 5.2cm. Data was taken for n =10800 sweeps, sampled at 500Hz, and filtered at 100Hz. The rotation frequency of the disk is 5/8Hz. Calibrations: Parallel (top graph) 2.32±0.28mV/K, Perpendicular (bottom) 4.17±0.50mV/K. This is the third run, first in a series format, of MAP VDA #2.

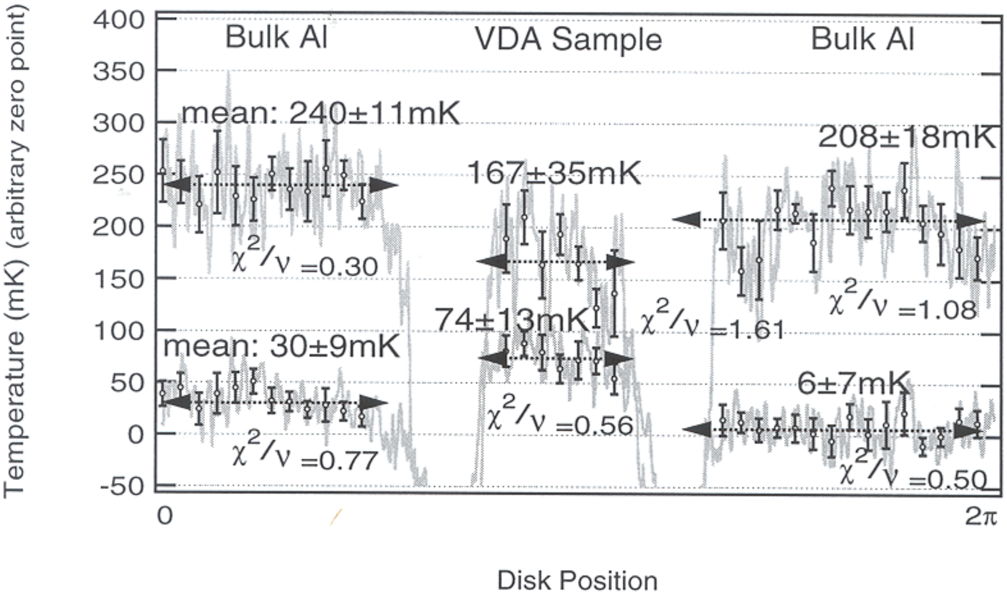

Table 7: Emissivities relative to bulk aluminum (6061-T6). $(e - e_{Al}) \times 10^4$. A minus sign denotes less emissive than the aluminum. $E_{\|}$ denotes the parallel polarization and $E_{\perp}$ denotes the perpendicular polarization.

MAP VDA #1.

Date	$E_{\|}$	$E_{\perp}$
1/17/98	-5.98 ± 3.34	-8.43 ± 2.92

MAP VDA #2.

Date	$E_{\|}$	$E_{\perp}$
1/16/98	2.64 ± 2.32	-2.59 ± 0.97

Figure 26. Initial system baseline for the Series 2. Bulk Al Disk (6061-T6), Series 2. 3/5/98 The disk is flat to: 245μm. Distance, feed to sample: 5.2cm. Data taken for n =10000 sweeps, sampled at 1kHz, and filtered at 300Hz. The disk is rotating at 5/4Hz. Calibrations: Parallel (top graph) 2.08±0.25mV/K, Perpendicular (bottom) 3.30±0.40mV/K

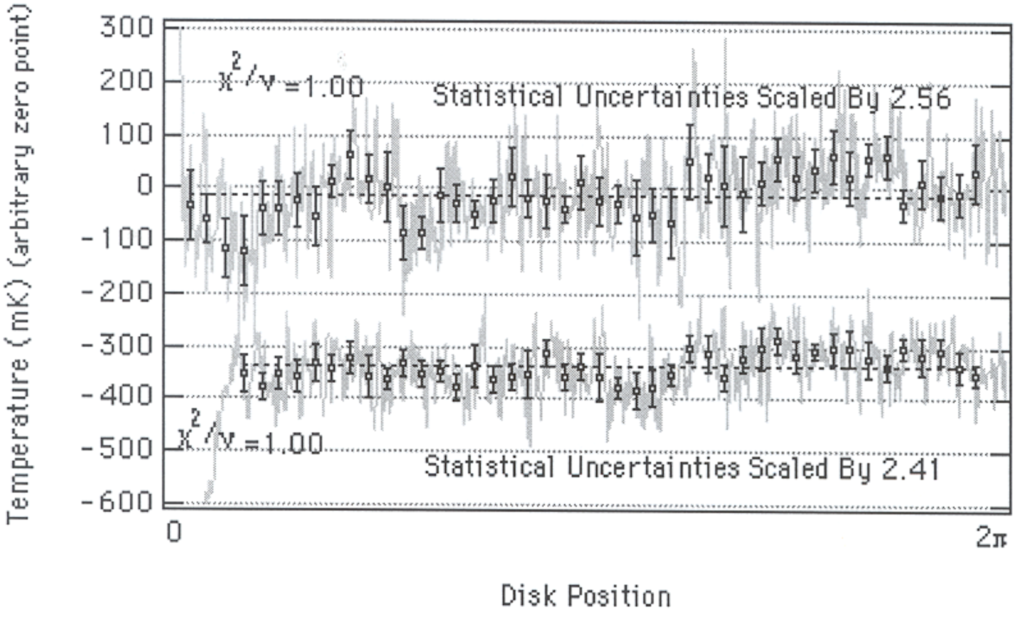

Vc. Series 2

The second of two groupings of related measurements was performed in early March of 1998. This collection of five measurements, labeled Series 2, was assembled over a period of five days with as little alteration of the apparatus as possible. The only alterations that occurred between trials were the detachment and reattachment of the feed and the microwave absorber shield around the disk edge. These were necessary in order to change samples. Reattachment of the microwave absorber shield was done meticulously, making certain that no outer disk edge was visible to the feed. Likewise the horn was consistently returned to position. It was kept at a constant distance of 5.2cm from the sample.

After establishing the system baseline (Figure 26) we performed one additional measurement each for the two MAP VDA samples. Figure 27 shows the data for MAP VDA #1 and Figure 28 shows the data for MAP VDA #2.

Figure 27. Data for MAP VDA #1, Series 2. 3/4/98 The temperature scale is inverted. The disk is flat to 245μm. Distance, feed to sample is 5.2cm. Data was taken for n =10000, sampled at 1kHz, and filtered at 300Hz. The disk is rotating at 5/4Hz. Calibrations: Parallel (top graph) 2.09±0.25mV/K, Perpendicular (bottom) 3.28±0.39mV/K. This is the third and final run of MAP VDA #1. Spikes at the start of the data are due to switch transients.

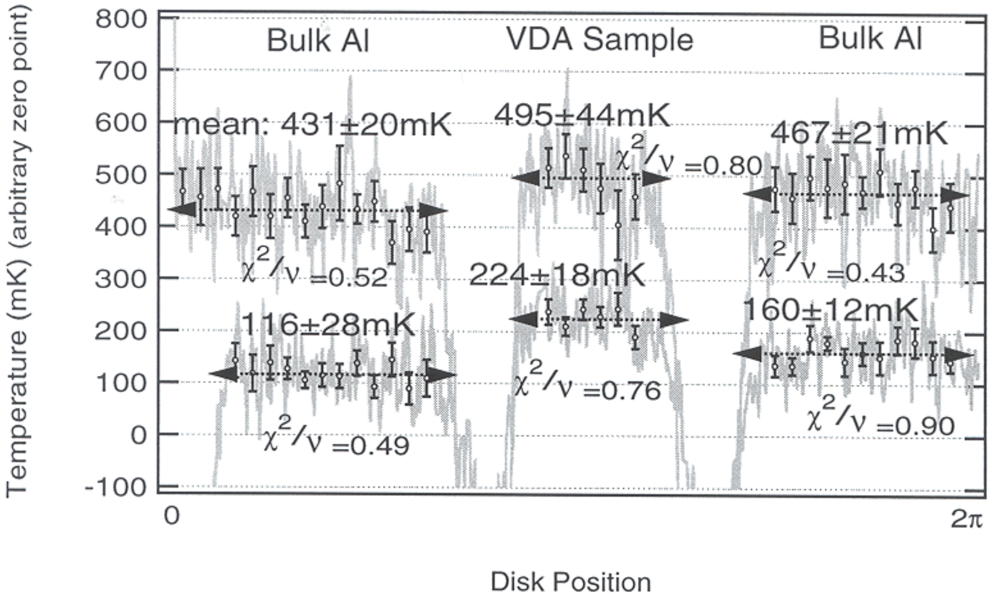

We also measure the Cu-Al-SS sample used in the discussion of Section Vf4. Finally, we reestablish the system baseline (Figure 29). As the final system baseline is tighter we use it to begin scaling data. All data in the parallel polarization is then scaled by at least 2.30. All data in the perpendicular polarization is scaled by at least 2.02.

The emissivity differences we calculate for the MAP VDA samples are displayed in Table 8. The uncertainties here do not include corrections due to the systematic effects discussed below in Sections Vf.

For all of the data taken in Series 2, there are large dips or spikes at the beginning of the data. These are due to the mechanical switch not having enough time to return completely to position before data started to be averaged.

Figure 28. Data for MAP VDA #2, Series 2. 3/4/98 The temperature scale is inverted. The disk is flat to 245µm. Distance, feed to sample is 52cm. Data taken for n =10000 sweeps, sampled at 1kHz, and filtered at 300Hz. The disk is rotating at 5/4Hz. Calibrations: Parallel (top graph) 2.10±0.25mV/K, Perpendicular (bottom) 3.34±0.40mV/K This is the fourth and final run of MAP VDA #2. The signal spikes at the start of the data are due to switch transients.

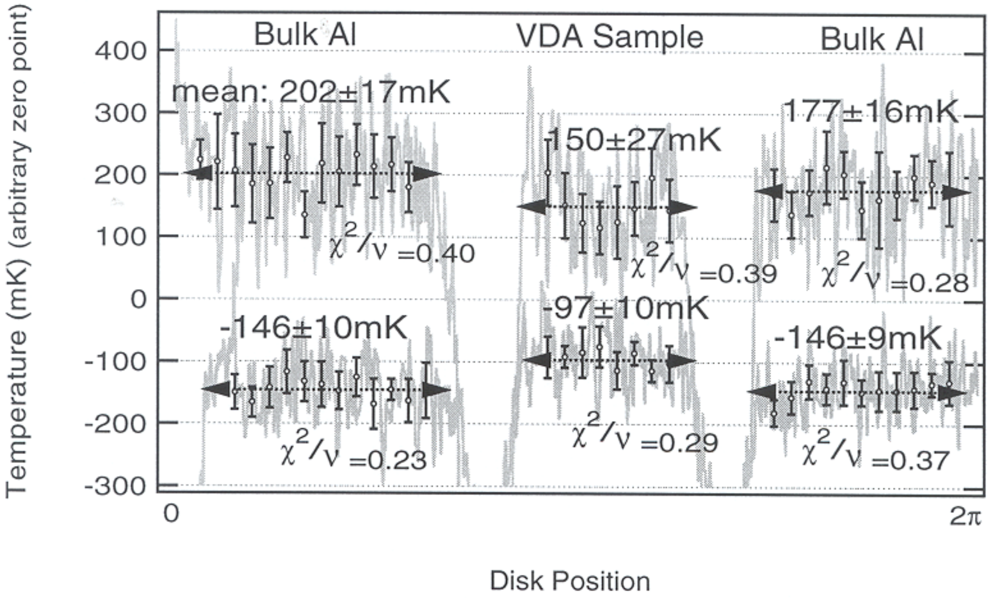

Figure 29. Final system baseline for Series 2. Spike at start of data is due to switch transient. Bulk Al Disk (6061-T6), Series 2. 3/9/98 The disk is flat to: 245µm. Distance, feed to sample: 5.2cm. Data taken for n =10000 sweeps, sampled at 1kHz, and filtered at 300Hz. The disk is rotating at 5/4Hz. Calibrations: Parallel (top graph) 2.17±0.26mV/K, Perpendicular (bottom) 3.37±0.40mV/K

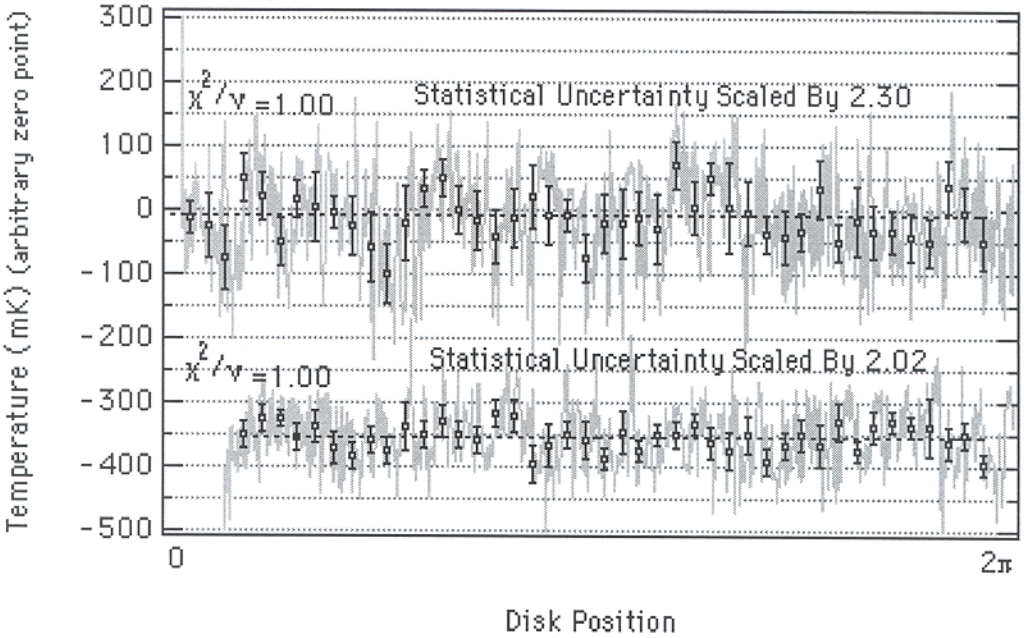

Table 8: Emissivities relative to bulk aluminum (6061-T6). $(e - e_{Al}) \times 10^4$. *A minus sign denotes less emissive than the aluminum.* $E_{\|}$ *denotes the parallel polarization and* $E_{\perp}$ *denotes the perpendicular polarization.*

MAP VDA #1.

Date	$E_{\|}$	$E_{\perp}$
3/4/98	-2.13 ± 3.01	-3.98 ± 1.76

MAP VDA #2.

Date	$E_{\|}$	$E_{\perp}$
3/4/98	1.85 ± 2.04	-2.27 ± 0.93

Figure 30. System baseline for the Greenbank sample. Bulk Al Disk (6061-T6), Greenbank. 2/19/98 The disk is flat to: 245μm. Distance, feed to sample: 5.2cm. Data taken for n =10000 sweeps, sampled at 1kHz, and filtered at 300Hz. Calibrations: Parallel (top graph) 1.94±0.23mV/K, Perpendicular (bottom) 2.97±0.36mV/K

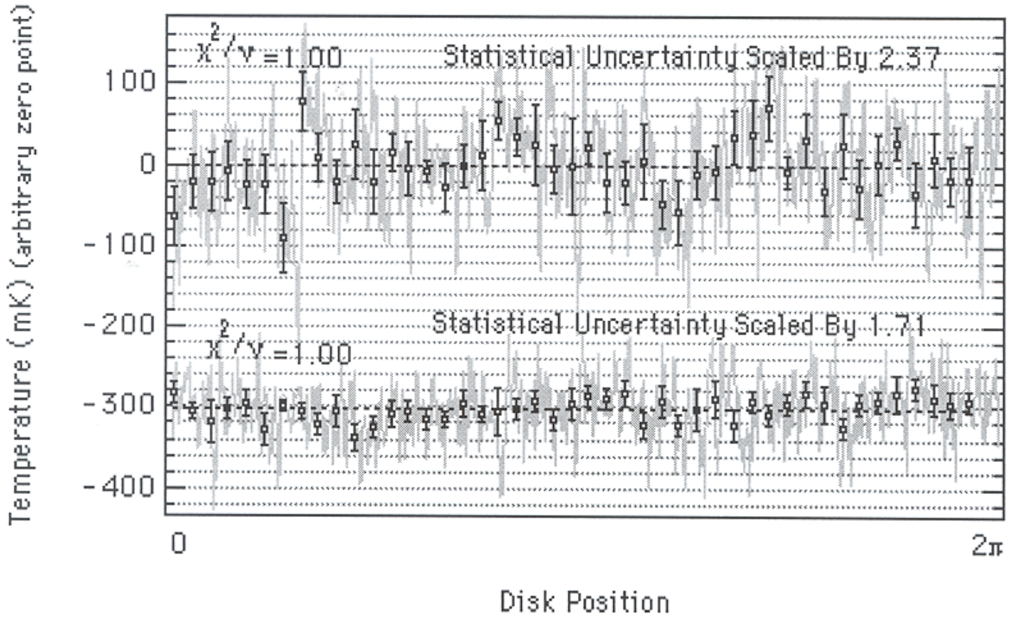

Vd. Greenbank

Data was taken near the end of February 1998 for the reflector of the Greenbank telescope. We determine the system baseline (Figure 30) and perform two measurements, Figures 31 and 32. Error bars in Figure 31 are multiplied by 2.37 for the parallel polarization and 1.71 for the perpendicular polarization. Those for figure 32 had to be multiplied by more as suggested by Figure 33 and discussed below. We do not yet consider the uncertainties discussed in Sections Vf.

The final two measurements in the Greenbank series, one of the Greenbank sample (Figure 32) and one of the Bulk Al disk (Figure 33), were sampled and low-pass filtered a little differently than usual. We filtered at 30Hz to attempt to remove as much noise as possible before averaging. The result of this was to increase the degree to which the signal was correlated (see Section IVc) and not to improve the signal to noise at all. The error bars we get are larger. The

Figure 31. First measurement of the Greenbank sample. Greenbank Sample, Greenbank. 2/20/98 The disk is flat to: 245μm. Distance, feed to sample: 5.2cm. Data taken for n =8400 sweeps, sampled at 500Hz, and filtered at 100Hz. The disk is rotating at 0.63Hz. Calibrations: Parallel (only graph) 2.06±0.25mV/K, Perpendicular (bottom) 2.94±0.35mV/K.

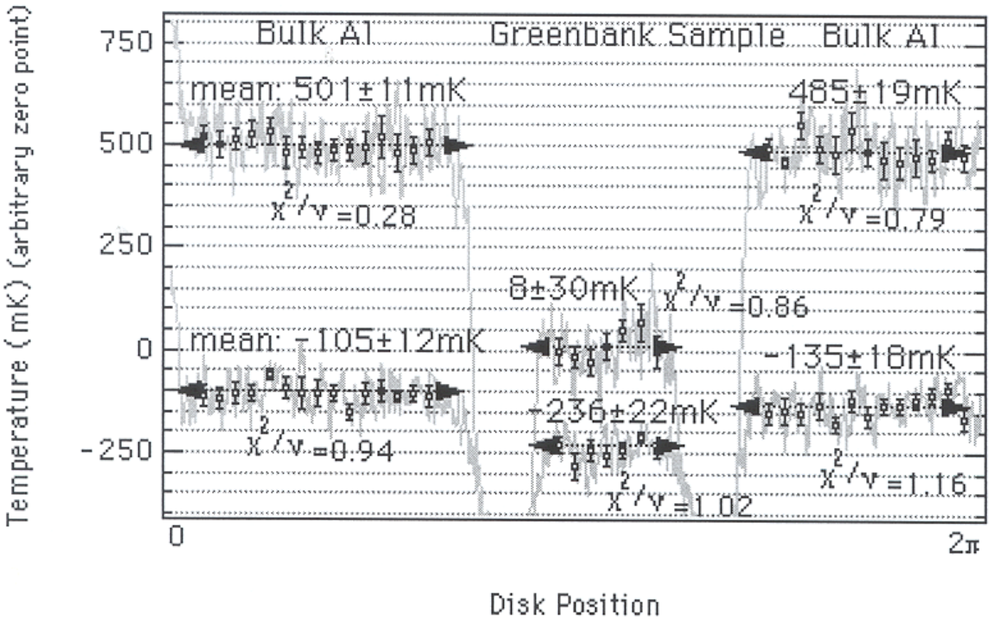

Figure 32. Second measurement of the Greenbank sample. Data are binned in groups of twenty. Greenbank Sample, Greenbank. 2/25/98 The disk is flat to: 245μm. Distance, feed to sample: 5.2cm. Data taken for n =20000 sweeps, sampled at 1.5kHz, and filtered at 30Hz. The disk is rotating at 1.22Hz. Calibrations: Parallel (only graph) 1.83±0.22mV/K, Perpendicular (bottom) 2.84±0.34mV/K.

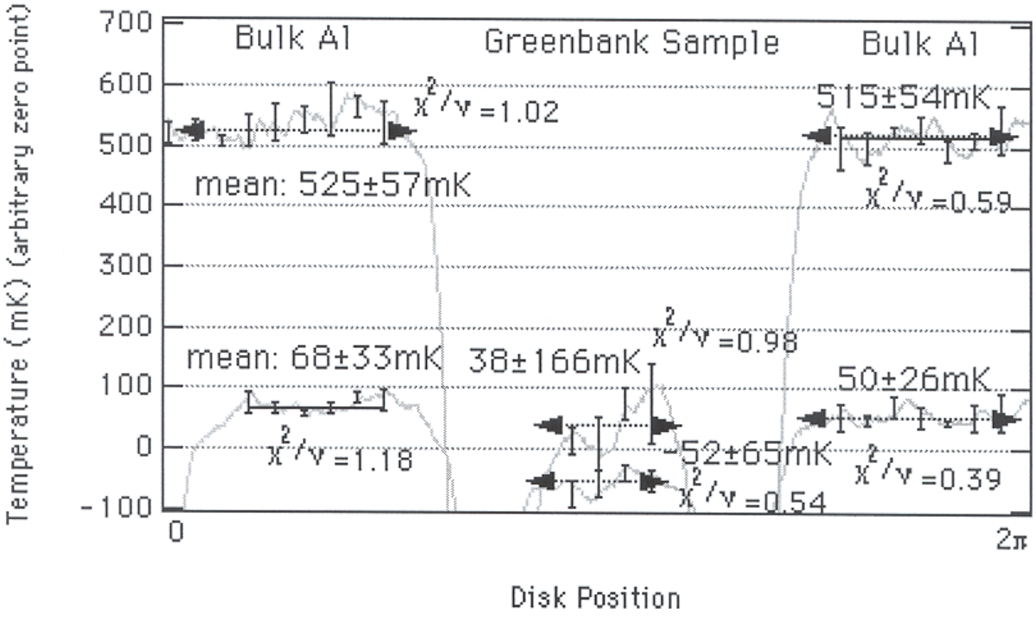

data is displayed in Table 9.

Figure 33. Flat aluminum disk used as baseline for the final Greenbank measurement. Data are correlated here in groups of twenty. Bulk Al Disk (6061-T6), Greenbank. 2/24/98 The disk is flat to: 245μm. Distance, feed to sample: 5.2cm. Data taken for n =50000 sweeps, sampled at 1.5kHz, and filtered at 30Hz. The disk is rotating at 1.27Hz. Calibrations: Parallel (only graph) 1.90±0.23mV/K.

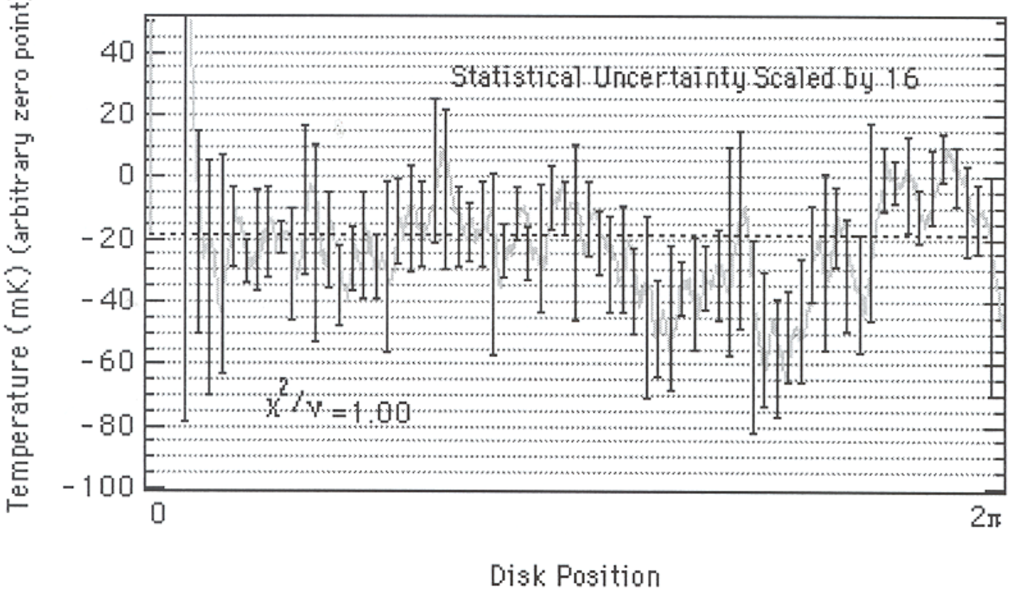

Table 9: Emissivities relative to bulk aluminum (6061-T6). $(e - e_{Al}) \times 10^4$. *A minus sign denotes less emissive than the aluminum.* $E_{\parallel}$ *denotes the parallel polarization and* $E_{\perp}$ *denotes the perpendicular.*

Greenbank Sample.

Date	$E_{\parallel}$	$E_{\perp}$
2/20/98	22.47 ± 2.08	5.37 ± 1.71
2/25/98	22.33 ± 10.28	5.14 ± 4.40

Ve. Carbon Fiber Thread Tests

We performed four measurements of aluminum disks with sections coated with spray-on adhesive and covered in carbon fiber thread. First we measured the aluminum disk alone (Figure 34) to establish the baseline. Next, we measured the sample with the adhesive only. (Figure 35) There are small dips due to this coating. They are, however, far smaller and negligible in comparison to the huge signals produced from the carbon fiber.

The first sample that we measure, is a disk coated with carbon fiber thread less than 0.5mm long. Figure 36 shows the appearance of the disk. The threads are randomly scattered across the surface. Figure 37 shows the resulting data after a short integration period.

Next we measure a sample with thread greater than 3cm long scattered over the disk surface. Figure 38 shows the appearance of the sample. Figure 39 shows the data.

Finally, we measure a sample with the threads, greater than one in long, lined up along the radial direction. Figure 40 shows the appearance of the sample. Figure 41 shows the data.

These data will not be interpreted here.

Figure 36. Digital photograph of samples used in carbon fiber thread tests. Here carbon fiber thread is smaller that 0.5mm.

Figure 38. Digital photographs of samples used in carbon fiber thread tests. Here the thread is longer than 3cm and is criss-crossed along the sample.

Figure 40. Digital photographs of samples used in carbon fiber thread tests. Here the thread is longer than 3cm and is lined-up along the radial direction.

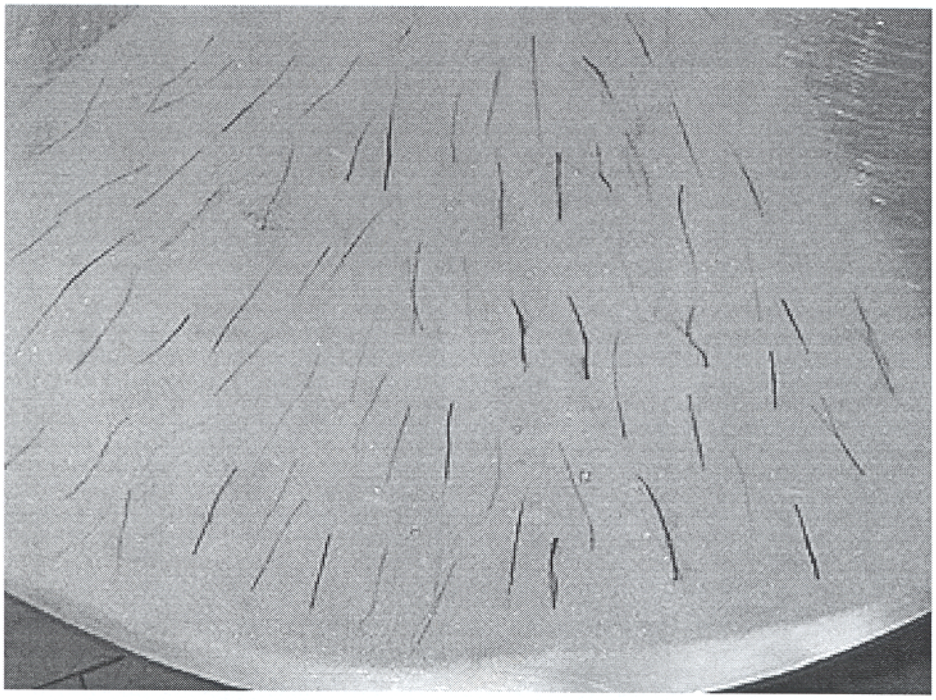

Figure 34. System Baseline. Al Disk. 3/24/98 Disk flat to 368μm. Horn 5.2cm from sample. Data filtered at 100Hz and sampled at 500Hz. Calibrations: Parallel Polarization (top graph) 2.35±0.28mV/K, Perpendicular Polarization (bottom, dotted) 3.30±0.34mV/K.

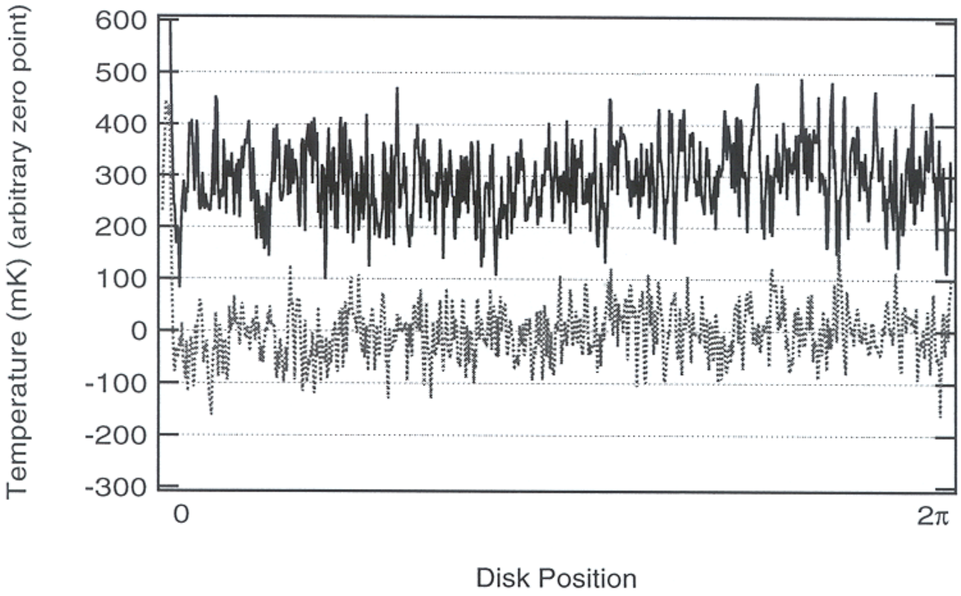

Figure 35. Al Disk, with spray-on adhesive. 3/24/98 368μm. Horn 5.2cm from sample. Data filtered at 100Hz and sampled at 500Hz. Calibrations: Parallel Polarization (top graph) 2.35±0.28mV/K, Perpendicular Polarization (bottom, dotted) 3.30±0.34mV/K.

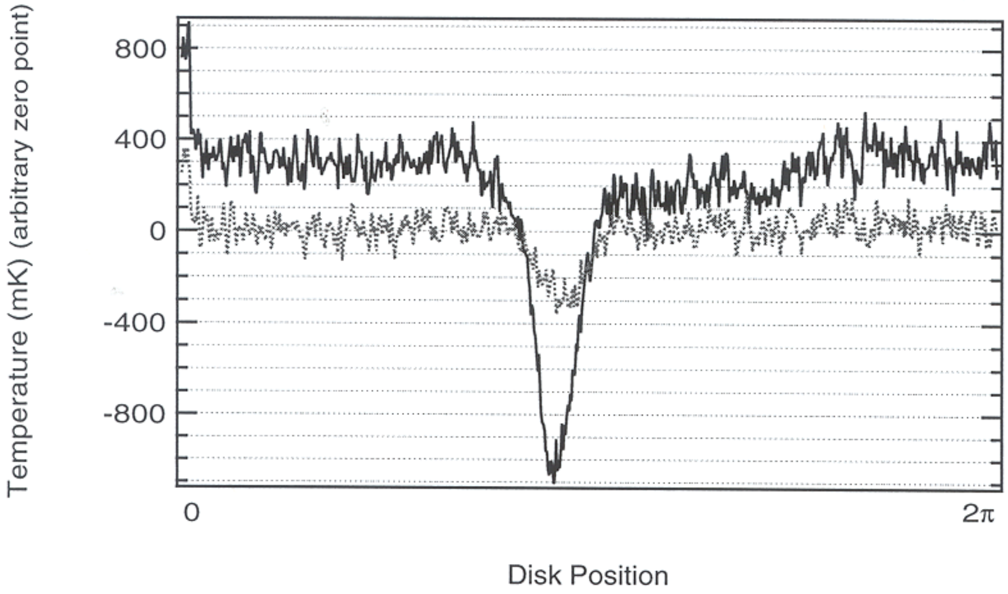

Figure 37. Al Disk with carbon fiber threads (¡1mm long), scattered. 3/24/98 The temperature scale is inverted. There is 31.10±0.05mg of carbon fiber in an area of 528cm^2. The disk is flat to 368μm. The horn is 5.2cm from the disk. Data is filtered at 100Hz and sampled at 500Hz. Calibrations: Parallel Polarization (top graph) 2.35±0.28mV/K, Perpendicular Polarization (bottom, dotted) 3.30±0.34mV/K.

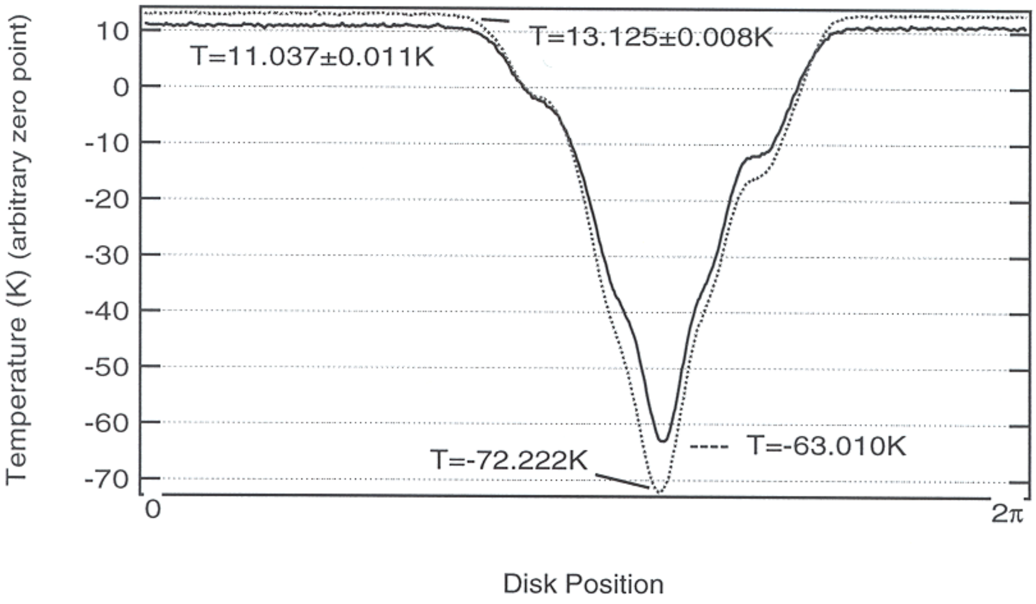

Figure 38. Al Disk with carbon fiber threads (1 in long), scattered. 3/24/98 The temperature scale is inverted. There is 20.55±0.02mg of carbon in an area of 528cm^2. The disk is flat to 368μm. The horn is 5.2cm from the disk. Data is filtered at 100Hz and sampled at 500Hz. Calibrations: Parallel Polarization (top graph) 2.35±0.28mV/K, Perpendicular Polarization (bottom, dotted) 3.30±0.34mV/K.

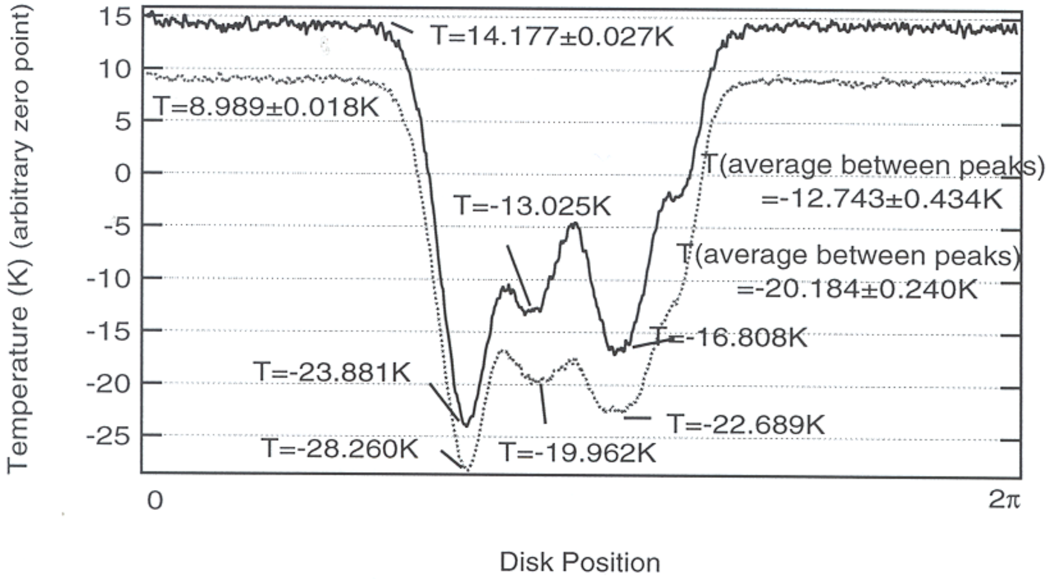

Figure 41. Al Disk with carbon fiber threads (1 in long), lined up in radial direction. 3/24/98 temperature scale is inverted. There is 20.55±0.02mg of carbon fiber in an area of 528cm^2. The disk is flat to 368μm. The horn is 5.2cm from the disk. Data is filtered at 100Hz and sampled at 500Hz. Calibrations: Parallel Polarization (top graph) 2.35±0.28mV/K, Perpendicular Polarization (bottom, dotted) 3.30±0.34mV/K.

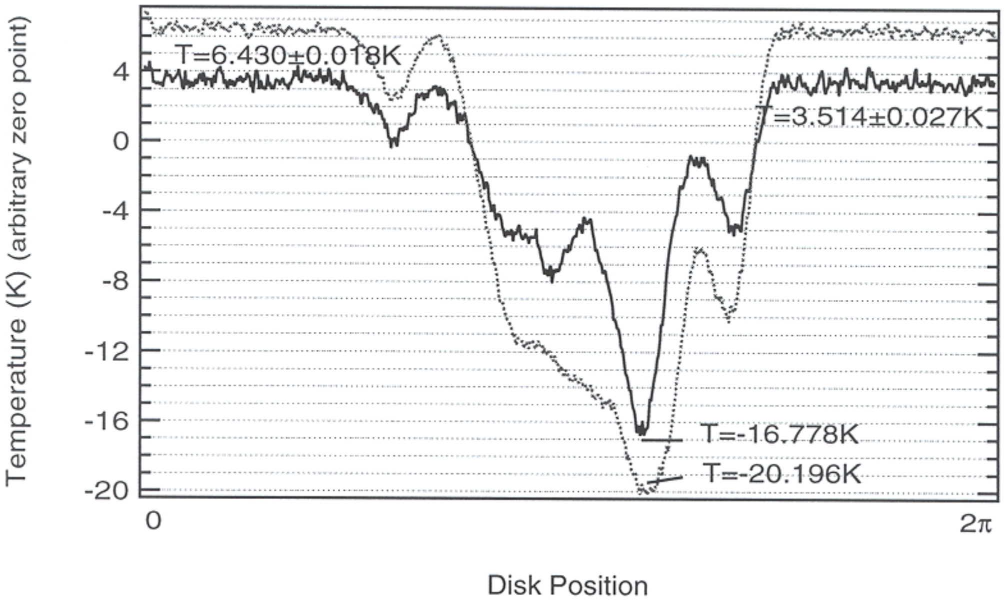

Vf. Systematic Effects and Checks

Vf1. Disk Flatness

One of the earliest systematic effects noticed was the signal variation due to an unflat sample disk. If the sample does not remain flat at 45° as it rotates, then it moves toward and away from the horn, allowing varying amounts of 300K ambient radiation into the feed. As the amount of ambient radiation entering changes continuously from some minimum to some maximum amount as the disk rotates, the result is a signal amplitude with a sinusoidal variation.

There were two reasons for the unflatness of the disk. The first, the fact that the axle was somewhat loose on its bearings, was corrected by shimming the bearings. The second and more lingering factor had to due with inexactness in the millings of the axle and sample disks. Although the disk and axle look perfectly flat, connecting them and spinning the disk reveals them not to be so. In order to correct for this, shims were placed between the axle and disk before every measurement. With a dial indicator, one can then, by trial and error, add or remove shim until the disk is adequately flat.

Figures 42 and 43 illustrate the way in which we quantify what is meant by adequately flat. Measurements were taken for each polarization, with the plain aluminum disk shimmed to varying levels of flatness. We then fit cosines to the data to find what portion of the total signal variation was due to the unflatness. Reduced Chi-squared χ^2/ν values for each fit are reported. A χ^2/ν equal to unity indicates a good fit, as discussed in Section IVd.

All of our fits appear to be good ones. Comparatively, only at the smallest unflatness—245-490μm peak to peak—in the perpendicular polarization (Figure 43) does the fit begin to appear poorer. This indicates that there is probably a negligible amount of signal variation (well below the rms) due to unflatness in this data.

Figure 42. Cosine Fits at Different Flatnesses in the Parallel Polarization. Al Disk (6061-T6): 11/14/97. All data taken for n =12000 sweeps, sampled at 500Hz, and filtered at 100Hz. Calibration: Parallel Polarization 5.10±0.61mV/K

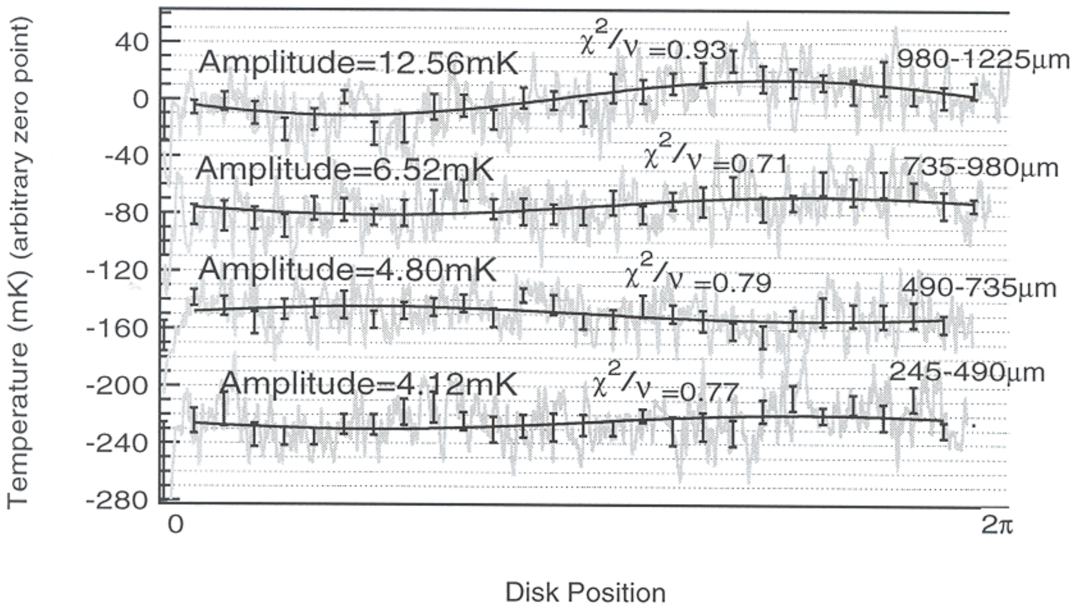

Figure 43. Cosine Fits at Different Flatnesses in the Perpendicular Polarization. Bulk Al Disk (6061-T6): 11/14/97. All data taken for n =12000 sweeps, sampled at 500Hz, and filtered at 100Hz. Calibration: Perpendicular Polarization 5.10±0.61mV/K

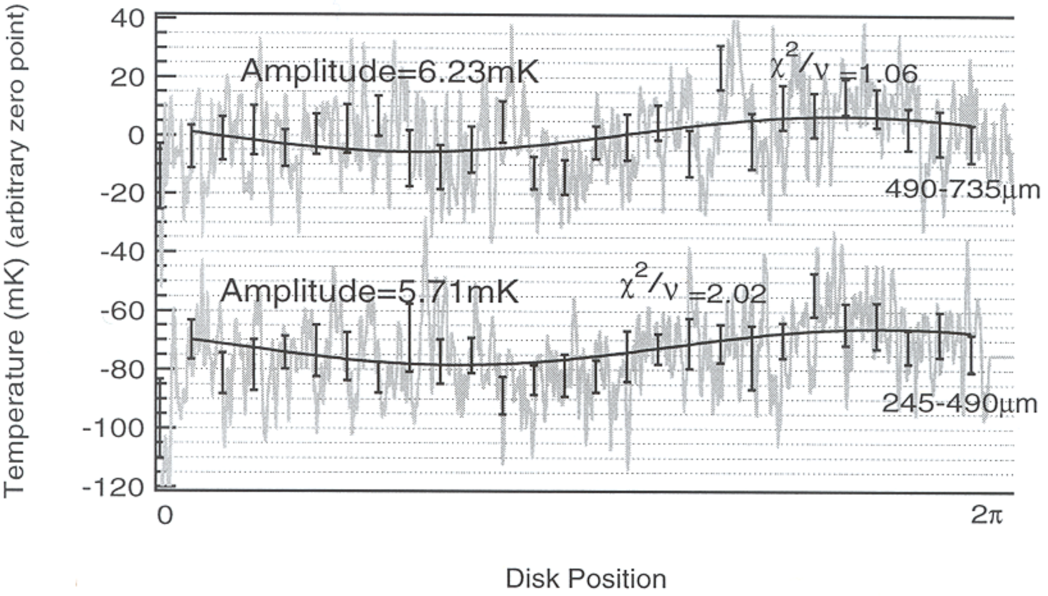

The result of these consideration, as illustrated by the plots, is that a disk shimmed flat to within 490μm suffers a tiny systematic side effect due to its unflatness. The cosine amplitude is down to 4.12mK in the parallel polarization and 5.71mK in the perpendicular polarization. The amplitude of the cosine term appears, from the plots, to increase monotonically with the unflatness of the sample. It was unobservable below 245μm peak to peak unflatness.

For all data, flatness of the disk is reported. Samples were shimmed to within or around 245μm. A generous estimate on the uncertainty in measurements of these samples due to unflatness is ±5mK for each polarization. Rather than treat this correction separately, however, we absorb it into the system baseline uncertainty discussed in Section IVd. We do this because the size of the error bars for the system baselines are determined partially by the disk flatness anyways. As long as we remain consistent throughout the data grouping in keeping the samples flat, then the systematic uncertainty due to the unflatness of the disk is contained within the system baseline measurement.

Figure 44. Orientations of the carbon fiber thread used to test the polarization convention. Each of the four diagrams displays the sample disk (with the axle at center) and the feed horn with respect to the thread.

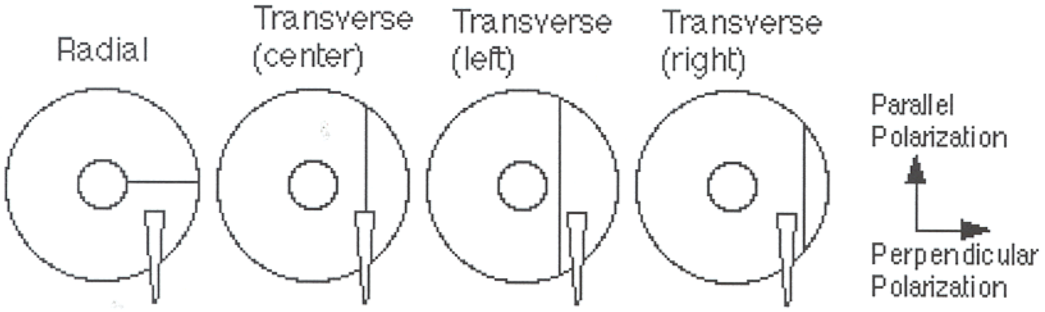

Vf2. Polarization Check

Another important systems check was to verify that what we had been calling the parallel polarization did in fact correspond to radiation polarized parallel to the plane of reflection. (Figure 44) Similarly, we desired to check our polarization convention for the perpendicular polarization.

To be absolutely certain that we had correctly identified the polarization, we used carbon fiber thread to test the emission patterns. Figure 44 shows the different thread orientations tested. The thread diameter was 0.5mm, smaller than the 3mm wavelength of radiation at 90GHz. Thus radiation could only be emitted polarized along the thread's length. We see this from Maxwell's equations. (Section IIa)

Consider Figure 45. Current can only flow along the length of the thread; there is not enough room across the width. From Ampere's law (equation (8)), we know that the magnetic field $\vec{H}$ is perpendicular to the direction of current flow. Radiation that comes off of the thread will be in the direction $\vec{E} \times \vec{H}$. As illustrated in Figure 45, the $\vec{H}$ field is perpendicular to the direction of current flow and the $\vec{E}$ field is parallel to it. Thus the radiation is polarized in the direction of the threads length.

Figure 46 shows data taken with a piece of thread attached radially outward, from the disk axle to the edge. The spike in the center of the data is due

Figure 45. Orientations of the $\vec{E}$ and $\vec{H}$ fields with current flowing along the carbon fiber thread.

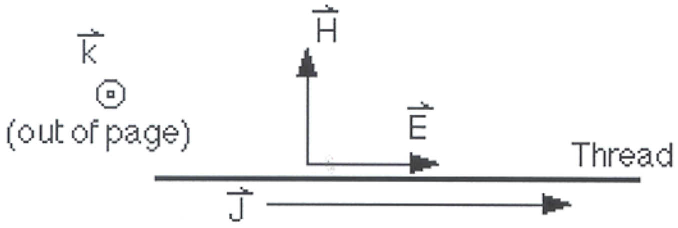

Figure 46. Bulk Al disk with 0.25mm diameter carbon fiber thread in radial direction. The disk is Flat to: 245μm peak to peak. Distance, feed to sample is: 5.2cm. Sample Rate: 500Hz. Filtered at: 100Hz. Calibrations: Parallel 2.17±0.26mV/K, Perpendicular 3.36±0.40mV/K.

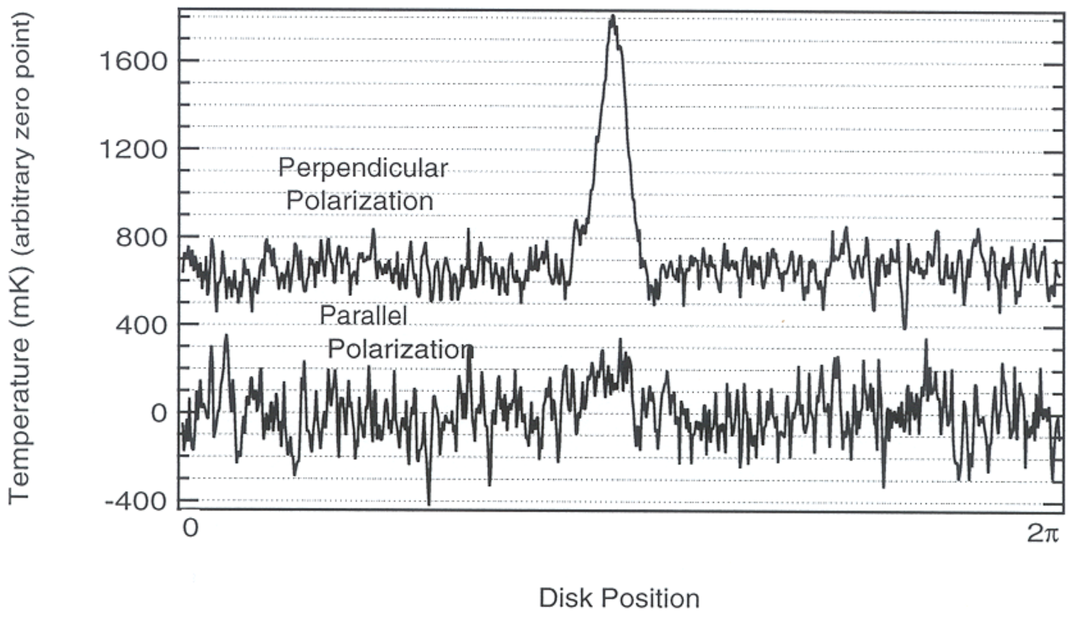

to the thread. That the spike is far larger in the perpendicular polarization verifies that we are indeed looking at radiation polarized perpendicular to the plane of reflection.

The next three graphs (Figures 47, 48, and 49) contain data taken with the thread situated transversely, across the disk. The first is data with the thread just left (3cm from center) of the feed horn. Figure 44 illustrates the various thread positions used. In Figure 47, there are two spikes in the data as the thread crosses the beam path twice per disk rotation. When it crosses, it is oriented near 45°. Thus we expect near equal contributions in each polarization

Figure 47. Bulk Al disk with 0.25mm diameter carbon fiber thread in the transverse direction, just left (3cm) of beam path center. The disk is Flat to: 245μm peak to peak. Distance, feed to sample is: 5.2cm. Sample Rate: 500Hz. Filtered at: 100Hz. Calibrations: Parallel 2.17±0.26mV/K, Perpendicular 3.36±0.40mV/K.

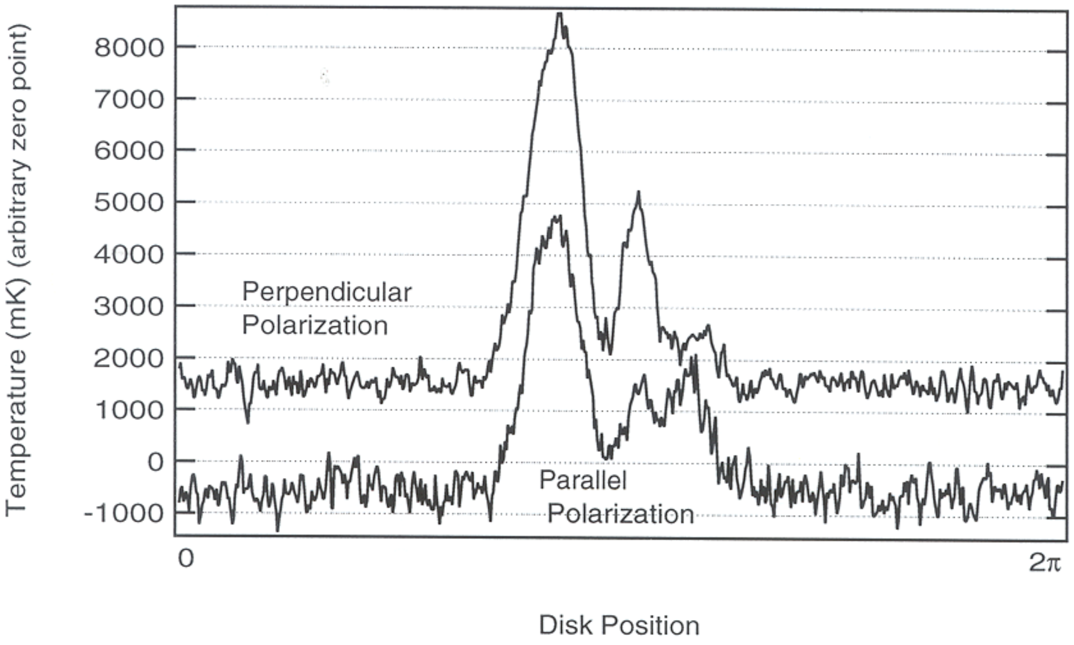

as observed.

The plot in Figure 48 is for the thread centered in the beam path. Consider what we would expect to happen in both polarization. In the parallel polarization. The thread should, as the disk rotates, rotate into and out of the beam path, filling the beam maximally when the thread lies entirely in the reflection plane. In the perpendicular polarization, there should be a small signal as the thread rotates into the beam path, never quite aligning perpendicular to the reflection plane. Then there should be a drop as it aligns with the reflection plane and cannot emit perpendicularly. Finally, there should be another small increase as it rotates away. From Figure 48, we see that this behavior is the observed behavior. Not only is the pattern evident, but we see that radiation is emitted much more strongly in the parallel polarization.

The final plot is for the carbon fiber thread just right (3cm) of the feed horn. Here, when the thread is aligned such that it could emit in the perpen-

Figure 48. Bulk Al disk with 0.25mm diameter carbon fiber thread in the transverse direction, at center of beam path. The disk is Flat to: 245μm peak to peak. Distance, feed to sample is: 5.2cm. Sample Rate: 500Hz. Filtered at: 100Hz. Calibrations: Parallel 2.17±0.26mV/K, Perpendicular 3.36±0.40mV/K.

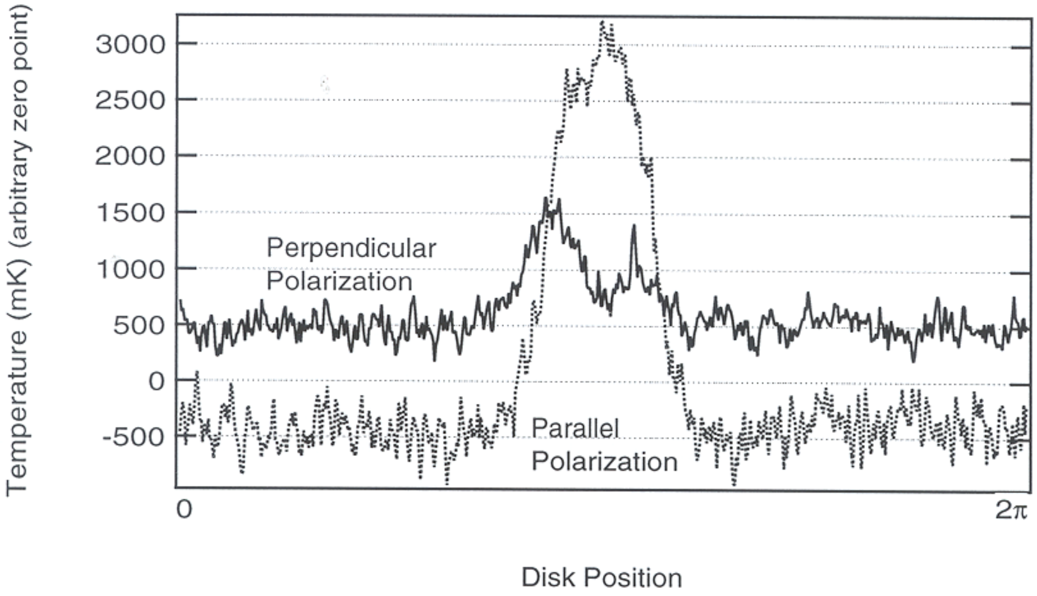

Figure 49. Bulk Al disk with 0.25mm diameter carbon fiber thread in the transverse direction, just right (3cm) of beam path center. The disk is Flat to: 245μm peak to peak. Distance, feed to sample is: 5.2cm. Sample Rate: 500Hz. Filtered at: 100Hz. Calibrations: Parallel 2.17±0.26mV/K, Perpendicular 3.36±0.40mV/K.

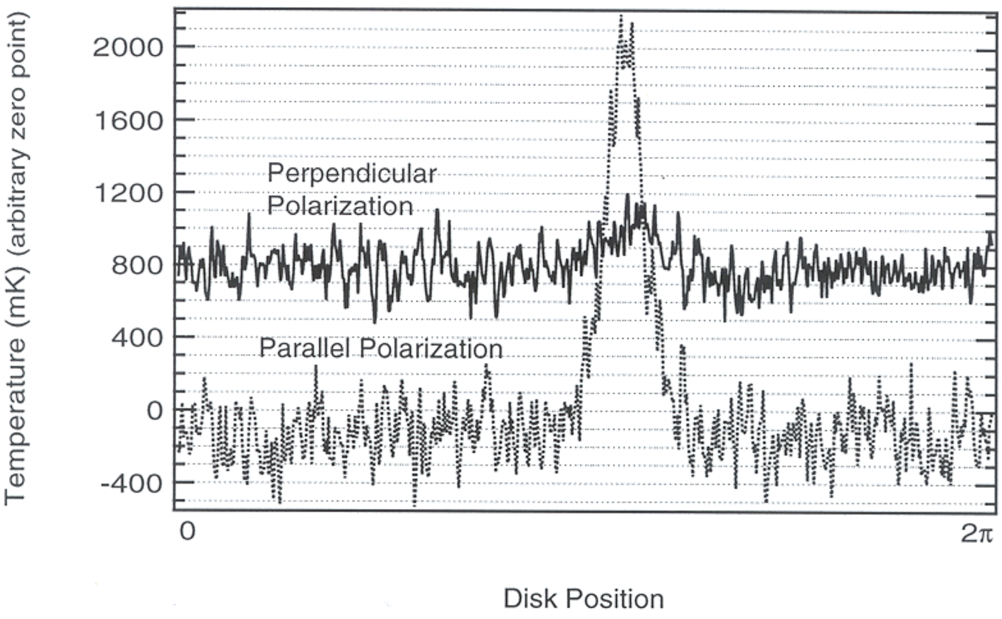

dicular direction, it is too far from the beam. Only radiation in the parallel polarization is emitted strongly. Our convention explains the data in this plot as well as the other three plots. Therefore we accept it and continue its use.

We can also note that these plots give us the width of the beam. For the case when the thread is in the radial direction, (Figure 46) the thread is effectively a point source of radiation as it moves by. We use this width as a gauge for removing the data around signal spikes from all data involving the polyester tape and sample edges. The signal spike in Figure 46 is approximately $\pi/5$ radians wide. Similarly, we see from Figure 48 that the beam is approximately $\pi/2$ radians wide in the parallel polarization.

Figure 50. Orientation and convention for the electromagnetic wave polarizations we are considering.

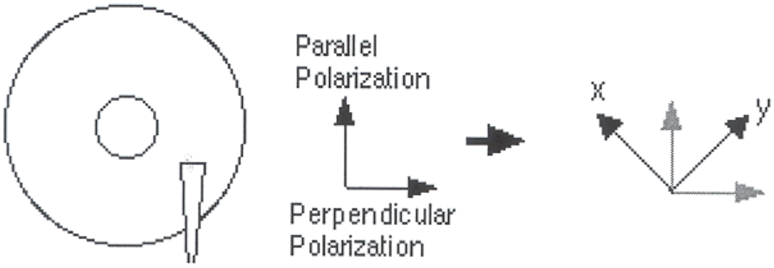

Vf3. Rotated Polarizations

This is perhaps the most important analysis of our system. Here we rotate the feed horn with respect to the sample by 45°. (Figure 50) Thus we rotate the polarization axis by 45°. As discussed in the theory section, it was sufficient to treat emitted radiation as being polarized either parallel or perpendicular to the reflection plane. Any other polarization could then be represented as a linear combination of those two. By rotating the feed 45° we present the same linear combination of polarized radiation to each of the radiometer's two channels. The power is the same because it depends on the square of E and not the sign. Thus, the signal is expected to be the same in each channel. Any observed discrepancy would suggest an inconsistency and systematic problem in our apparatus. The channel that was previously labeled parallel is now referred to as X. The other (previously perpendicular) is labeled Y. Note that for all plots the temperature scale is inverted and larger emissivities correspond to signal decreases.

We measured four of the samples—the Bulk Al (6061-T6) disk, MAP VDA #1, MAP VDA #2, and the Cu-Al-SS disk. As usual, we use the plain aluminum disk as a baseline indicator. As in Section IVd, we use it to determine the size of our error bars. Also, we use it as an initial (before the other samples) and final check on the system consistency. (Figures 51 and 52) We subtract the signal due to channel X from that in channel Y and check that the stan-

Figure 51. Initial system baseline for the rotated polarization tests. Bulk Al Disk (6061-T6), Rotated Feed. 3/10/98 The disk is flat to: 245μm. The distance, feed to sample is 5.2cm. Data was taken for n =10000, sampled at 1kHz, and filtered at 300Hz. The disk rotated at 5/4Hz. The calibrations are: X(formerly parallel) 2.36±0.28mV/K, Y(formerly perpendicular) 3.14±0.38mV/K.

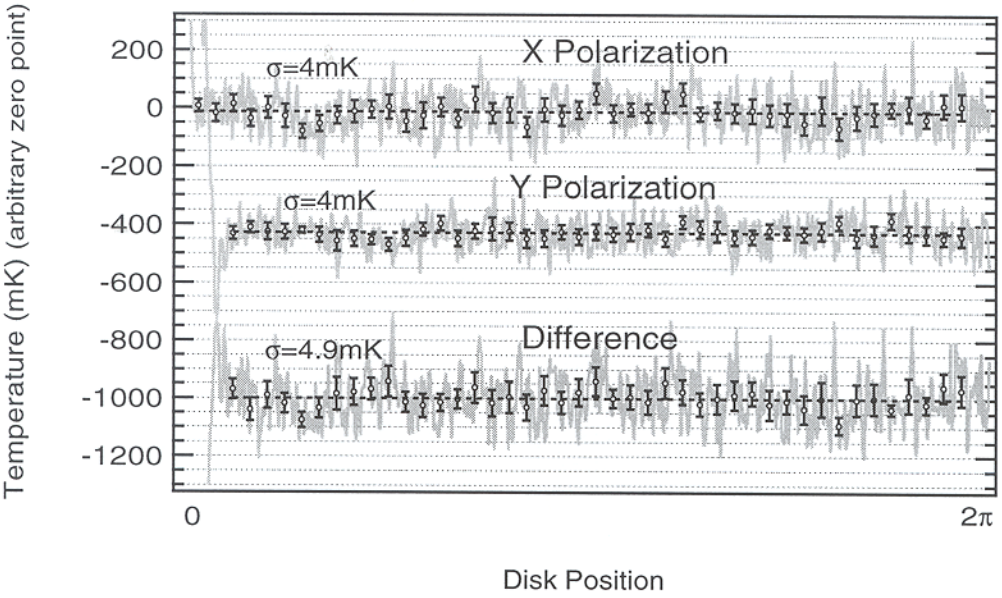

dard deviation divided by the square root of the number of uncorrelated data points σ of the difference signal is no larger than the sum in quadrature of the σ's of the individual signals. This you would expect for two similarly varying but independent signals. We observe this to be true for all of the samples we test. (Figures 51, 52, 59, 60, 61)

There are three plots for each sample. The first shows (Figures 53, 54, and 57) the entire signal, zoomed out to allow us to see that the large signal dips due to the tape at zone boundaries line up between channels. The second (Figures 55, 56, and 57) shows the data up close so that emissivity difference measurements can be attained and compared. Finally, there is a plot (Figures 59, 60, and 61) showing the ideal signal matchup found by varying the calibration ratio $C_{\parallel}/C_{\perp} \equiv R$. This sets bounds on the system calibration.

A first qualitative test of systematic consistency is to lay the data for each channel on top of one another to see how they match up. Examining the first

Figure 52. Final system baseline for the rotated polarization tests. Bulk Al Disk (6061-T6), Rotated Feed. 3/15/98 The disk is flat to: 245μm. The distance, feed to sample is 5.2cm. Data was taken for n =10000, sampled at 1kHz, and filtered at 300Hz. The disk rotated at 5/4Hz. The calibrations are: X(formerly parallel) 2.31±0.28mV/K, Y(formerly perpendicular) 3.24±0.39mV/K.

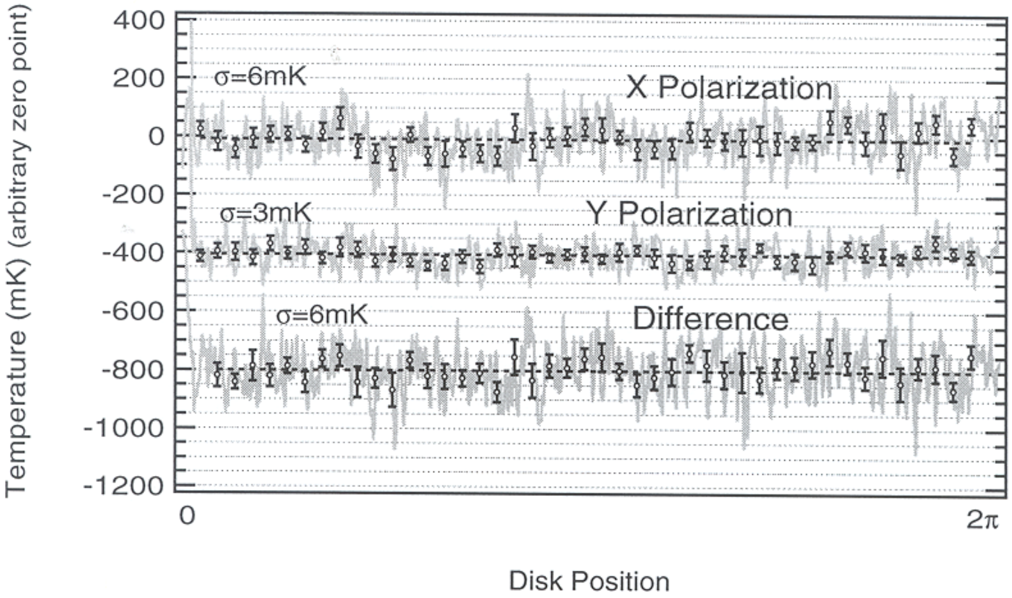

Figure 53. The calibrated signals are placed on top of each other for comparison. MAP VDA#1, Rotated Feed. 3/11/98 The disk is flat to: 245μm. The distance, feed to sample is 5.2cm. Data was taken for n =10000, sampled at 1kHz, and filtered at 300Hz. The disk rotated at 5/4Hz. The calibrations are: X(formerly parallel) (solid) 2.36±0.28mV/K, Y(formerly perpendicular) (dotted) 3.17±0.38mV/K.

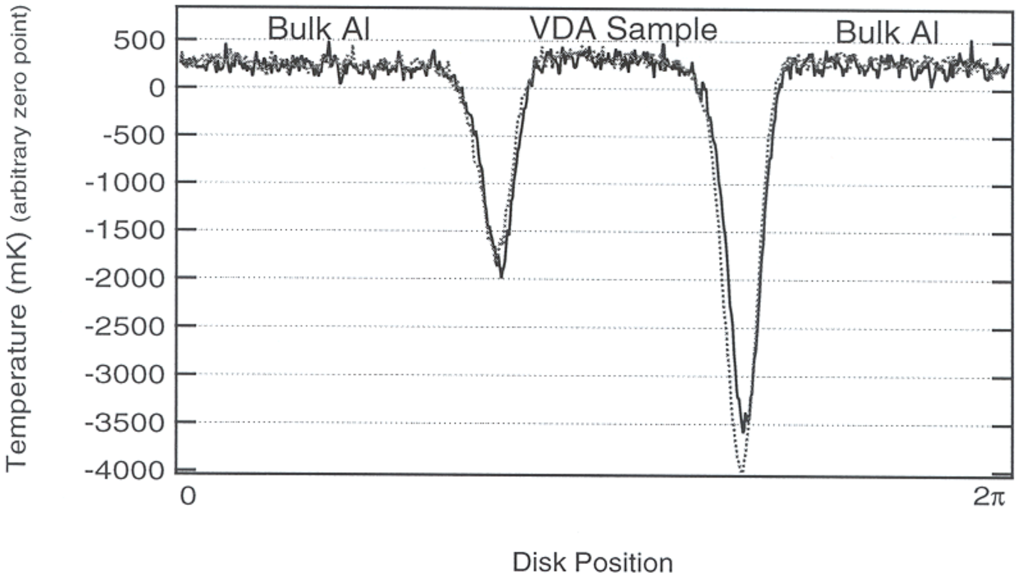

plot for each VDA sample, (Figures 53 and 54) the signals look practically equivalent between channels. The larger of the two spikes, however, is not

Figure 54. The calibrated signals are placed on top of each other for comparison. MAP VDA#2, Rotated Feed. 3/11/98 The disk is flat to: 245μm. The distance, feed to sample is 5.2cm. Data was taken for n =10000, sampled at 1kHz, and filtered at 300Hz. The disk rotated at 5/4Hz. The calibrations are: X(formerly parallel) (top graph) 2.39±0.35mV/K, Y(formerly perpendicular) (bottom) 3.16±0.38mV/K.

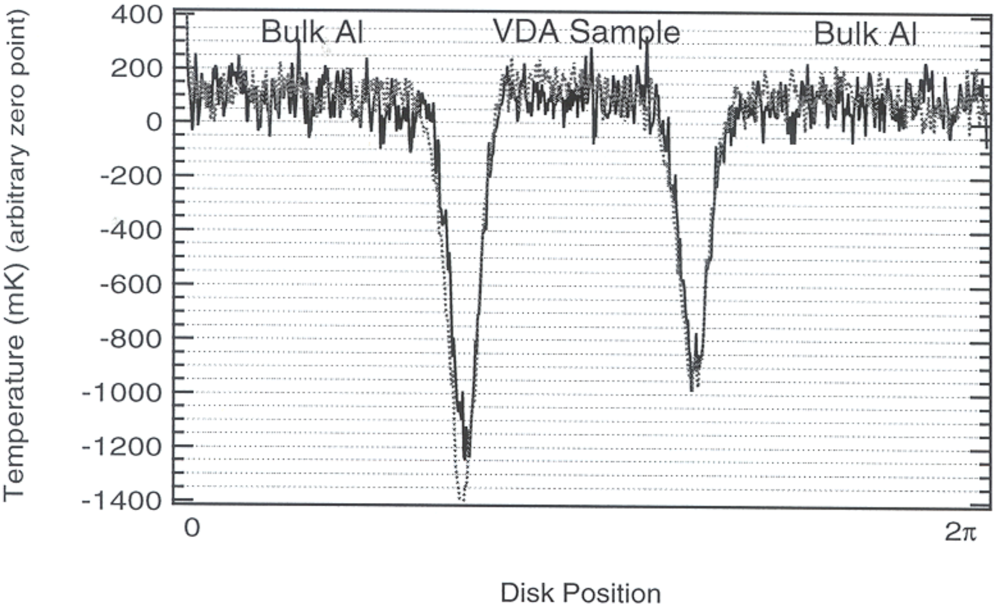

Figure 55. Blow up of the sample signals. MAP VDA#1, Rotated Feed. 3/11/98 The disk is flat to: 245μm. The distance, feed to sample is 5.2cm. Data was taken for n =10000, sampled at 1kHz, and filtered at 300Hz. The disk rotated at 5/4Hz. The calibrations are: X(formerly parallel) (top graph) 2.36±0.28mV/K, Y(formerly perpendicular) (bottom graph) 3.17±0.38mV/K.

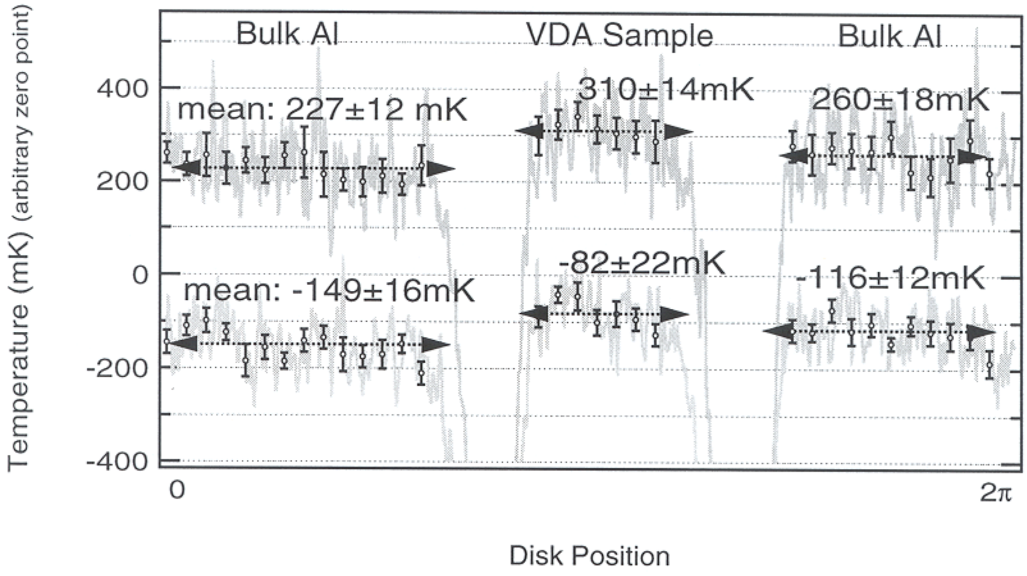

traced equivalently in each channel. As this is true for the second spike in MAP VDA #1 and for the first in MAP VDA #2, the larger of the two spikes

Figure 56. Blow up of the sample signals. MAP VDA#2, Rotated Feed. 3/11/98 The disk is flat to: 245μm. The distance, feed to sample is 5.2cm. Data was taken for n =10000, sampled at 1kHz, and filtered at 300Hz. The disk rotated at 5/4Hz. The calibrations are: X(formerly parallel) (top graph) 2.39±0.35mV/K, Y(formerly perpendicular) (bottom) 3.16±0.38mV/K.

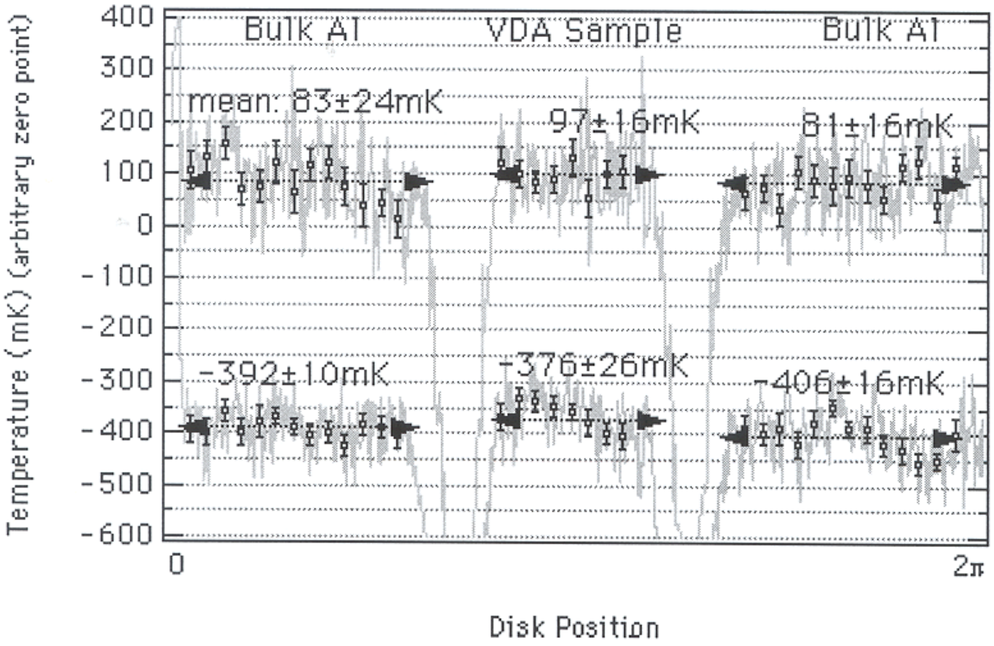

Figure 57. Cu-Al-SS, Rotated Feed. 3/14/98 The disk is flat to 980μm. Distance, feed to sample is 5.2cm. Data taken for n =10000 sweeps, sampled at 1kHz, and low pass filtered at 300Hz. The disk rotated at 5/4Hz. Calibrations: X(formerly parallel) (top graph) 2.45±0.29mV/K, Y(formerly perpendicular) (bottom) 3.57±0.43mV/K.

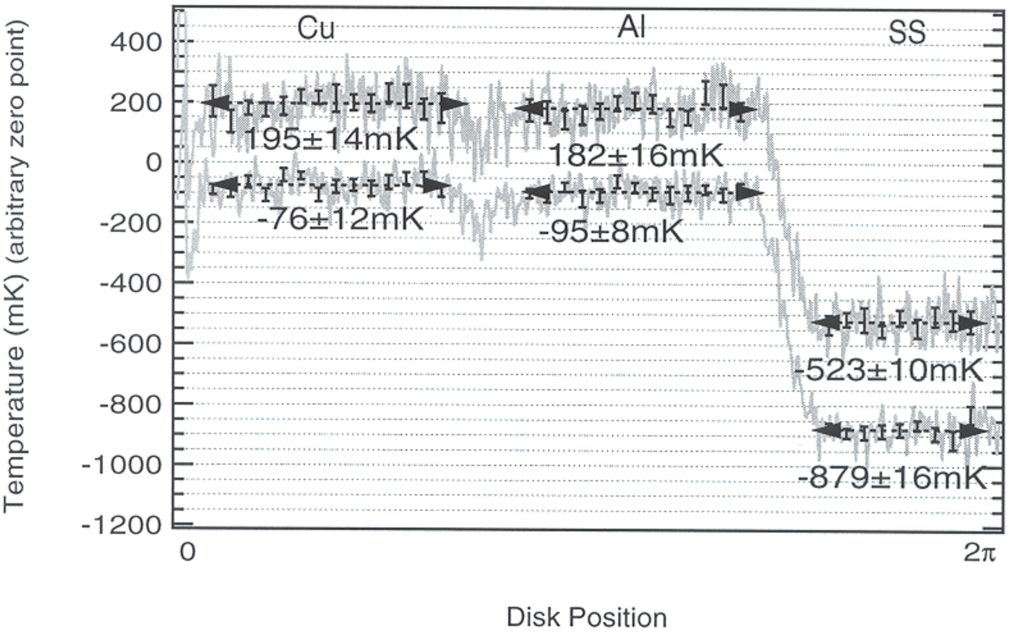

Table 10: Emissivities relative to bulk aluminum with the polarizations rotated. $(e - e_{Al}) \times 10^4$ *A minus sign indicates less emissive.*

Channel:	X	Y
Copper	-0.60 ± 1.40	-0.88 ± 0.92
Stainless (304)	32.66 ± 1.20	36.32 ± 1.12
MAP VDA #1	-3.08 ± 1.34	-2.34 ± 1.66
MAP VDA #2	-0.70 ± 1.66	-1.07 ± 1.81

in each instance, it seems to indicate a problem with measuring large signal variations.

There is no evidence, however, that this indicates a systematic defect. Rather, it is just an artifact of a too short signal averaging period. This is the portion of the disk that varies the most rapidly as it is sampled. Thus, the computer tends to receive widely varying values for the signal. One would expect these to require a longer period (than the rest of the disk) for both channels to average to the same curve.

The most important quantitative test we can perform is to actually determine the sample emissivity differences for each polarization and see if they agree. The method employed for calculating the emissivity differences is discussed in Section IVd. The results for these samples are displayed in Table 10. We, see that all of these data are consistent between channels except for that corresponding to stainless steel. We discuss below why we believe the stainless is inconsistent. Our conclusion is that the consistency of the system is excellent.

Vf4. Uncertainty in the System Calibration

The differing emissivty values (by 10%) calculated above for the stainless sample are telling us something about the system consistency. As the stainless steel–aluminum emissivity difference is the largest by an order of magnitude, it is the most sensitive to error in finding the system calibration. Errors would not be hidden within the statistical uncertainty as they would be for the smaller signal variations of other samples.

We can place bounds on the system calibration by requiring that emissivity differences be equivalent between channels as we have evidence from the last section to believe they are.

It is important to know accurately the calibration that allows us to convert the radiometer output in volts to units of temperature. We find this calibration by measuring the radiometer output voltage with a 300K piece of microwave absorber at the input and subtracting the output due to the 77K reflection of microwave absorber in the bath from the aluminum sample. The calibration C that we divide the output signal by to get units of temperature is then ΔV/(300-77)K.

Several factors contribute to an uncertainty in the calibration. There is a small uncertainty ($\approx$1%) in knowing room temperature and room pressure (to get the temperature at which LN_2 boils). There is an uncertainty due to the fact that we are not just seeing 77K from the bath; ambient 300K radiation can reflect from the LN_2 surface and enter the feed, making the bath look hotter. Finally, there is an uncertainty due to the drift in the radiometer. These last two are discussed below.

First, we can get an estimate of how much 300K ambient radiation is reflected from the surface of the LN_2 using the dialectric constant of LN_2. At 77K, ϵ is approximately equal to 1.4. (Guillien 1938) We will consider normal incidence. By analogy with the discussion leading up to equations (22) and (23) in Section IIa, the reflection coefficient is

$$|\vec{E}_1^\circ|^2/|\vec{E}_\circ^\circ|^2 = \left(\frac{1 - n_{LN_2}}{1 + n_{LN_2}}\right)^2 \tag{64}$$

where the index of refraction of LN_2 is the square root of the dialectric constant and the index of refraction of air has been replaced by unity. Plugging in $n_{LN_2} =$

$\sqrt{1.4}$, we find that the reflection coefficient is approximately 10^{-2}. Thus ambient 300K radiation reflected from the bath has the effect of making the bath look about 3K warmer than 77K. This is about 1% of the 300-77K temperature difference at which we calibrate.

Second, as the switch is mechanical and takes approximately a second to move between positions, it is not possible to rapidly and continuously calibrate the system. We are forced to find the system calibration before and/or after a data run. Thus it is vital that the system temperature be stable. Only then will the calibration we find be representative of the true (average) calibration over the course of a data run.

Unfortunately the system temperature does drift. Much of this can be side-stepped by allowing the radiometer to equilibrate overnight after power up. After equilibration, the drift is typically within 0.1mV/sec, corresponding roughly to 30-50μK/sec depending upon which polarization we are looking at. This does not appreciably affect the shape of the data; we subtract the DC offset of the signal every disk rotation. It does, however, affect the value of the system calibration because the system gain fluctuates.

Figure 58 displays two measurements, taken in late October of 1997, of the calibration drift over a period of 6.4 hours. We see that a typical drift over the course of a data run (4 hours for Series 2) is approximately 1%.

These data were taken previous to the establishment of the final setup, when the signal to noise would have been better. For the later data there is more noise, less gain, and the calibrations are smaller. But we are still in the square-law region (Section IIIb10) of our diode detector; so the effect would be similar. Therefore it is reasonable to expect that measurements of the system calibration before or after data runs should be sufficient, resulting in at most a 1% relative error.

Figure 58. Two plots of the relative variation in the system calibration C with time. These measurements were done prior to the advent of the corrugated feed and OMT.

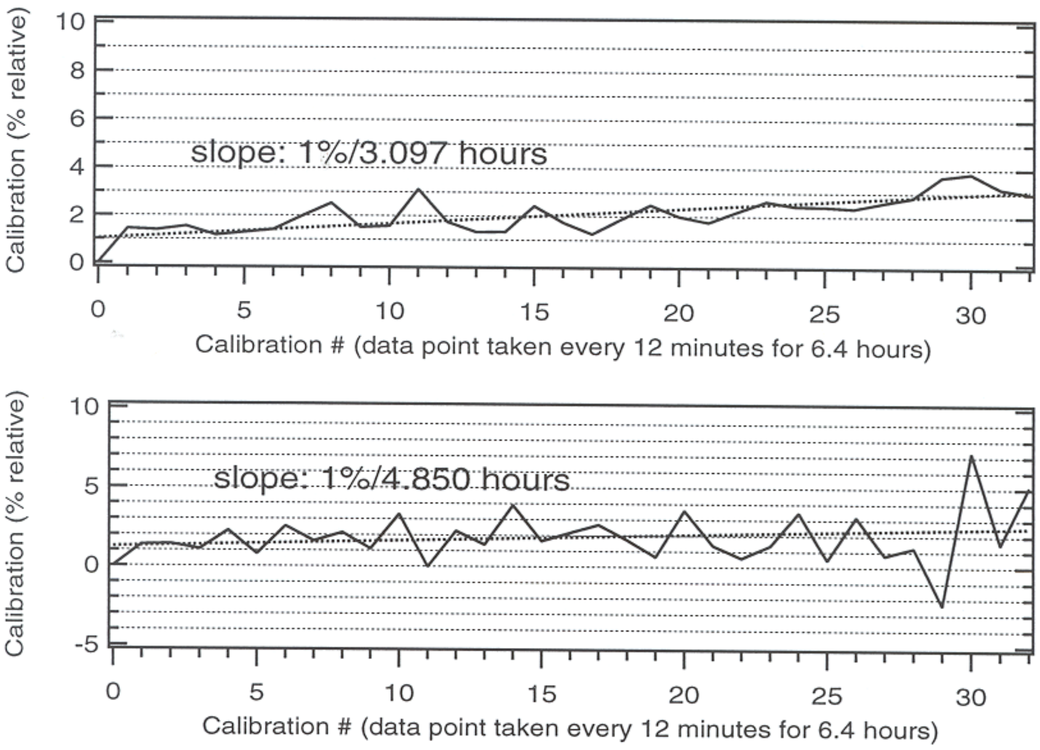

Pulling the three sources of uncertainty we have identified together, we expect a total uncertainty in the calibration of approximately 3%. We find a larger figure when we analyze the calibrations used in the rotated polarizations measurements.

Assuming, as seems evident from the data, that the system is consistent between channels, we can force the consistency to be precise and see what this tells us about the ideal system calibration for each channel. As mentioned above, there is more loss, and hence less signal to noise, and hence a smaller calibration, in the channel corresponding to the parallel polarization than in the channel corresponding to the perpendicular polarization. Therefore, in the case where each channel reads an identical signal, there should be a scaling factor R relating the two data streams. We can calculate this factor, which is just the ratio of the ideal calibrations $C_{\parallel}/C_{\perp}$, by minimizing the difference signal.

Table 11: Values for the calibration ratio R for three samples. Also reported are the measured values for the calibration ratio along with the error we believe to accompany them. These are from the calibrations reported with the plots in this section.

	MAP VDA #1	MAP VDA #2	Cu-Al-SS
R	0.66	0.63	0.61
Measured Ratio	0.75 ± 0.03	0.76 ± 0.03	0.67 ± 0.03
% Discrepancy	12%	17%	12%

We label data points in channel 1 by x_i and data points in channel 2 by y_i. Ideally $x_i = Ry_i - b$ for every data point i, where the term b takes into account any relative DC offset that could be present. To approach this ideal condition and to find the implication for R, we want to do a least squares fit between channels, to minimize the variance,

$$\sum_{n=1}^{N}((x_i - Ry_i + b)^2)^{1/2}, \tag{65}$$

with respect to b and R. Doing this and plugging the equation for b into the equation for R, we find

$$R = \frac{N\sum x_i y_i - \sum x_i \sum y_i}{N\sum y_i^2 - \left(\sum y_i\right)^2}. \tag{66}$$

This is just the covariance of the data in X and Y over the variance of the data in Y as one would expect. The results of applying this formula to the two MAP VDA samples and the Cu-Al-SS sample are displayed in Table 11. Figures 59, 60, and 61 show the calibration ratios applied to the data.

We see that the calibration ratio preferred by the data is in all cases smaller than that actually measured and used. This suggests either that the delta emissivity values we would calculate for channel X are too large or that the values for channel Y are too small. Alternatively, both could be off. Unfortunately, we do not have enough information to decide which case is true.

Naively, we might sidestep our uncertainty concerning error bounds and the possible asymmetrical shape of the confidence interval by simply reading Table 11 as implying an uncertainty as high as 17% on all calibrations, and

Figure 59. MAP VDA#1, Rotated Feed. 3/11/98. The lighter graph is the uncalibrated signal from the radiometer output in channel X. The darker data is channel Y data scaled to match channel X. The scaling factor is R. The difference signal and standard deviations are shown to illustrate the fit quality. The disk is flat to: 245μm. The distance, feed to sample is 5.2cm. Data was taken for n =10000, sampled at 1kHz, and filtered at 300Hz. The disk rotated at 5/4Hz.

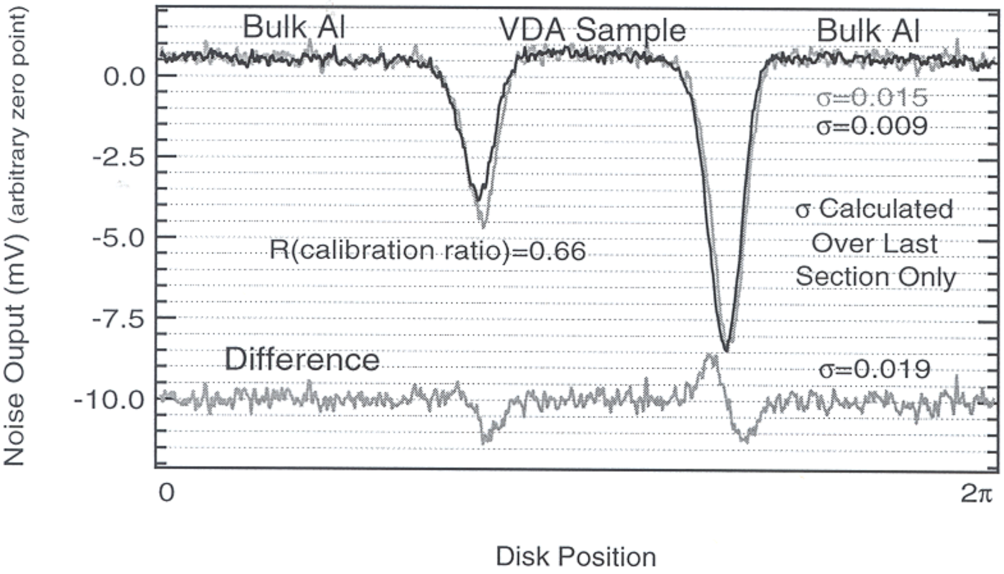

Figure 60. MAP VDA#2, Rotated Feed. 3/11/98 The lighter graph is the uncalibrated signal from the radiometer output in channel X. The darker data is channel Y data scaled to match channel X. The scaling factor is R. The difference signal and standard deviations are shown to illustrate the fit quality. The disk is flat to: 245μm. The distance, feed to sample is 5.2cm. Data was taken for n =10000, sampled at 1kHz, and filtered at 300Hz. The disk rotated at 5/4Hz.

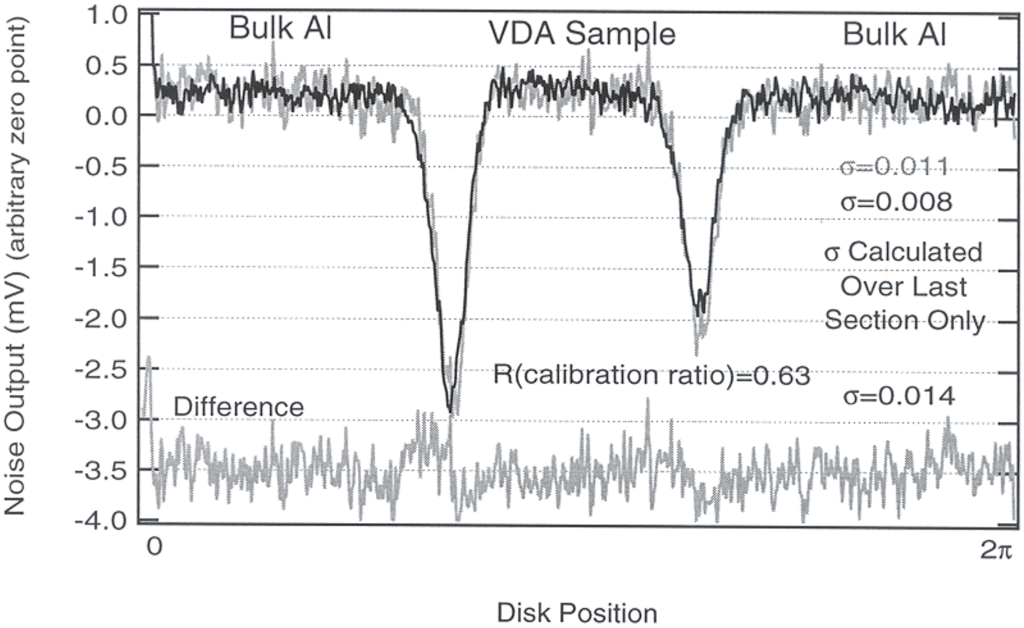

Figure 61. Cu-Al-SS, Rotated Feed. 3/14/98 The lighter graph is the uncalibrated signal from the radiometer output in channel X. The darker data is channel Y data scaled to match channel X. The scaling factor is R. The difference signal and standard deviations are shown to illustrate the fit quality. The disk is flat to 980µm. Distance, feed to sample is 5.2cm. Data taken for $n = 10000$ sweeps, sampled at 1kHz, and low pass filtered at 300Hz. The disk rotated at 5/4Hz.

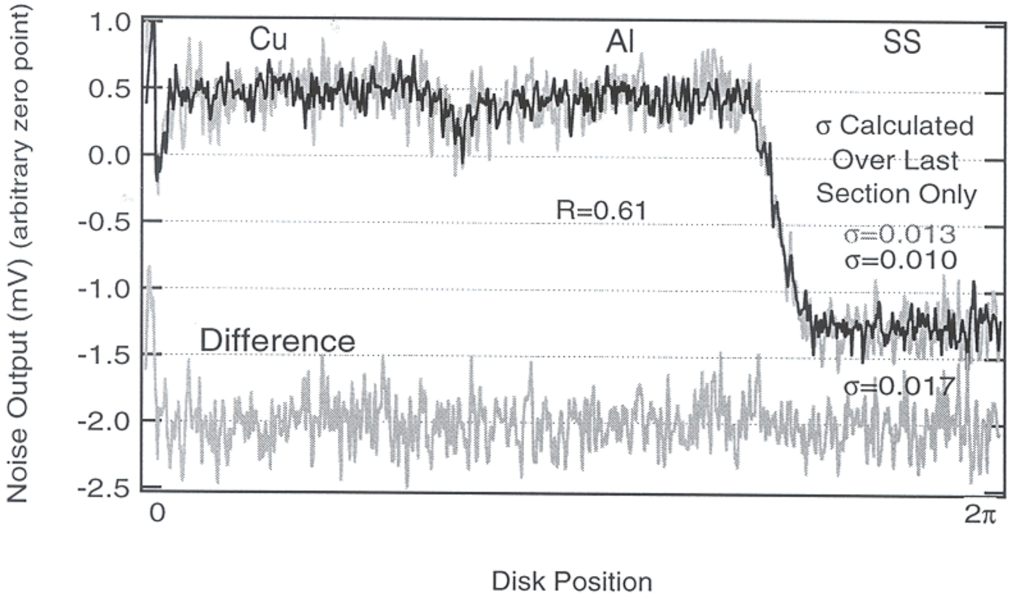

hence on all signal difference measurements. This would not be so bad; for most of the important MAP VDA measurements, the variations are comparatively small, and there is a reported uncertainty already this large. However, this would be an unjustified course of action with so little data to back it up. One of the three samples even appears to contradict the conclusion that its calibration ratio needs to be smaller. Note from Table 11 that for MAP VDA #1 Δe is larger in channel X than in channel Y. (Remember that R is a factor that scales down channel Y data.)

There is an important feature of the statistical procedure that produced these R's that must be noted. The test is more sensitive to larger signal variations than to smaller ones. That is, because it tries to line the data streams up by minimizing the variance, which is the sum of the differences at each point along the data stream, it weighs larger differences more than smaller ones. The test fails entirely when you try to run it on two relatively

Table 12: Summary of emissivities relative to bulk aluminum for the Cu-Al-SS sample. $(e - e_{Al}) \times 10^4$. *A minus sign denotes less emissive. Calculated values are from the model in section I. Uncertainties are the statistical and system baseline uncertainties only.* $E_{\parallel}$ *denotes the parallel polarization and* $E_{\perp}$ *denotes the perpendicular polarization.*

Cu-Al-SS	Copper		Stainless Steel	
	$E_{\parallel}$	$E_{\perp}$	$E_{\parallel}$	$E_{\perp}$
Early	-4.22 ± 7.13	-1.85 ± 7.41	55.87 ± 3.57	27.98 ± 4.40
Series 1 (tape)	-4.49 ± 1.90	-1.48 ± 3.06	68.05 ± 2.13	33.26 ± 1.58
Series 1	-5.47 ± 1.07	-1.95 ± 0.97	67.17 ± 1.67	33.20 ± 0.97
Series 2	-4.77 ± 2.13	-1.58 ± 0.93	56.05 ± 2.96	29.74 ± 1.11
Calculated	-6.63 ± 0.51	-3.32 ± 0.25	57.50 ± 0.65	28.81 ± 0.33

non-varying signals. For instance, applied to data from the plain aluminum disk, it forces the channel 2 data to have an rms of 0.

Therefore, when the test was applied to the MAP VDA samples, the variations it sought out most aggressively were those sharp spikes due to the sample boundaries (the tape). As we have noted, these do not provide an adequate criterion for comparing the data precisely because of sampling. The R values for the MAP VDA samples may not then be too significant.

The value for the Cu-Al-SS sample, however, is significant. Here there are no sharp spikes extending beyond the data. Rather, the biggest signal change is that due to an entire section of the sample, the emissivity difference between aluminum and stainless steel. Aligning these data by testing for the ideal system calibration ratio is highly significant.

We find that the measured system calibration ratio is, in this instance, 12% too large. Comfortingly, this is also the percent discrepancy in the measured Δe's between channels. (Table 10) Does this imply that there will always be a 12% error? No. It is a single measurement and cannot be interpreted statistically. What we can do, however, is look at all the stainless steel–aluminum measurements we have made. (Table 12) These data come from the plots in Figures 76, 77, 78, and 79.

To force all the SS-AL emissivity differences observed to be consistent, (Table 12) we need the relative uncertainty in the calibration to be about 6% in the perpendicular polarization and 12% in the parallel. This is a good measurement of the system calibration uncertainty if we assume that all the SS-Al measurements fall around the true mean. This may seem to be a somewhat arbitrary assumption, but it is not entirely. The following argument provides justification.

For all of our SS-Al data to be grouped around a mean that is not the true mean, the calibration ratio would have to have been measured to be too small or too large consistently. If it were too large, then all the perpendicular polarization data would be shifted up; all of the parallel polarization Δe's would have been shifted down. For a particular SS-Al measurement, if the calibration ratio used is larger than the true, the ratio of the calculated emissivities $\Delta e_{\|}/\Delta e_{\perp}$ will be larger than it should be, and conversely.

Fortunately, we know what that ratio should be; it is just 2! This, as we saw in section 1, is just a consequence of the system geometry. (Actually, it is not 2 exactly; some approximations went into equations (22) and (23), and a small amount of radiation enters the feed at incidence angles slightly different from 45°.) We can calculate the ratio for each of the four Cu-Al-SS disk measurements we have done. We find (from Table 12): 1.997, 2.046, 2.023, 1.885. These are respectively 0.2, 2.3, 1.2 and 5.8 % different from 2. However, the ratio of the mean Δe's for each polarization is 1.990, only 0.5 % away from 2!

Therefore, we can with reasonable confidence use the measurements in Table 12 for the emissivity difference between aluminum and stainless to set the calibration error bounds. As we have been dealing with ratios, and therefore cannot define the uncertainty separately for each channel, we are forced to

Figure 76. This is one of the earliest runs of the Cu-Al-SS sample. Cu-Al-SS, Early. 9/2/97. The disk is flat to: 980μm. Data taken for n =19200 sweeps, sampled at 1kHz, unfiltered. Calibrations: Parallel (top graph), Perpendicular (bottom, dotted) 16.9±2.0mV/K

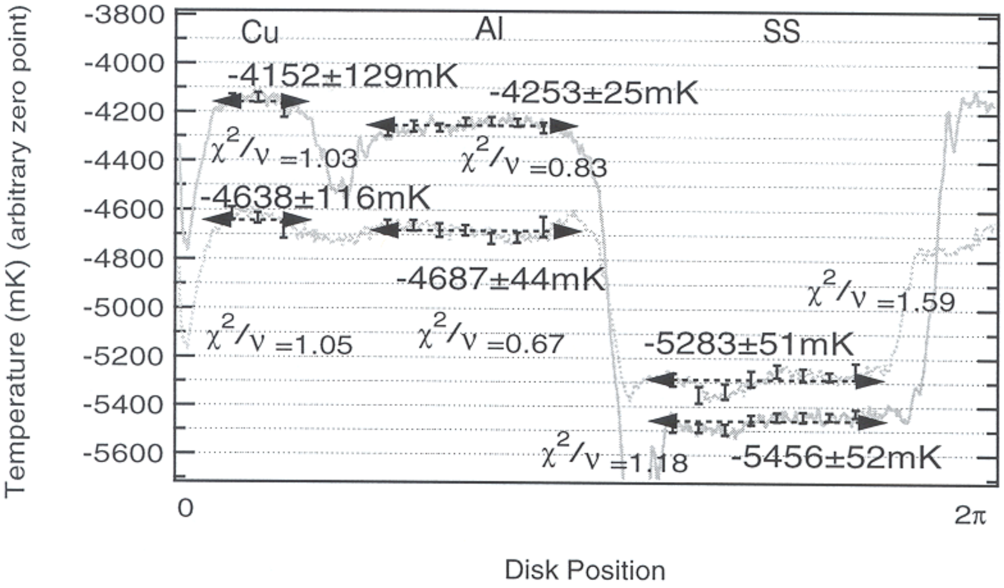

Figure 77. This is the first run of the Cu-Al-SS sample in a series format. There is polyester tape over the edges between each metal. Cu-Al-SS, Series 1 (tape). 1/20/98 The disk is flat to: 980μm. Data taken for n =7200 sweeps, sampled at 500Hz, and filtered at 100Hz. Calibrations: Parallel (top graph) 2.31±0.28mV/K, Perpendicular (bottom) 3.94±0.47mV/K.

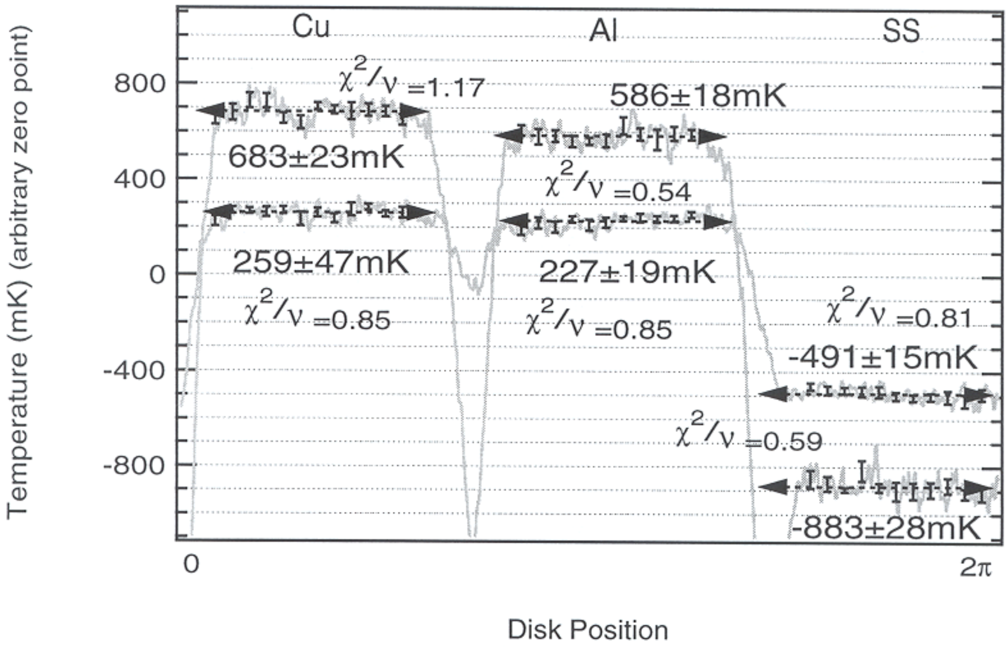

choose the larger of the two uncertainties. From the discrepancy in parallel

Figure 78. This is the second run of the Cu-Al-SS sample in a series format. Cu-Al-SS, Series 1 (no tape). 1/21/98 The disk is flat to: 980μm. Data taken for n =7200 sweeps, sampled at 500Hz, and filtered at 100Hz. Calibrations: Parallel (top graph) 2.31±0.28mV/K, Perpendicular (bottom) 3.94±0.47mV/K.

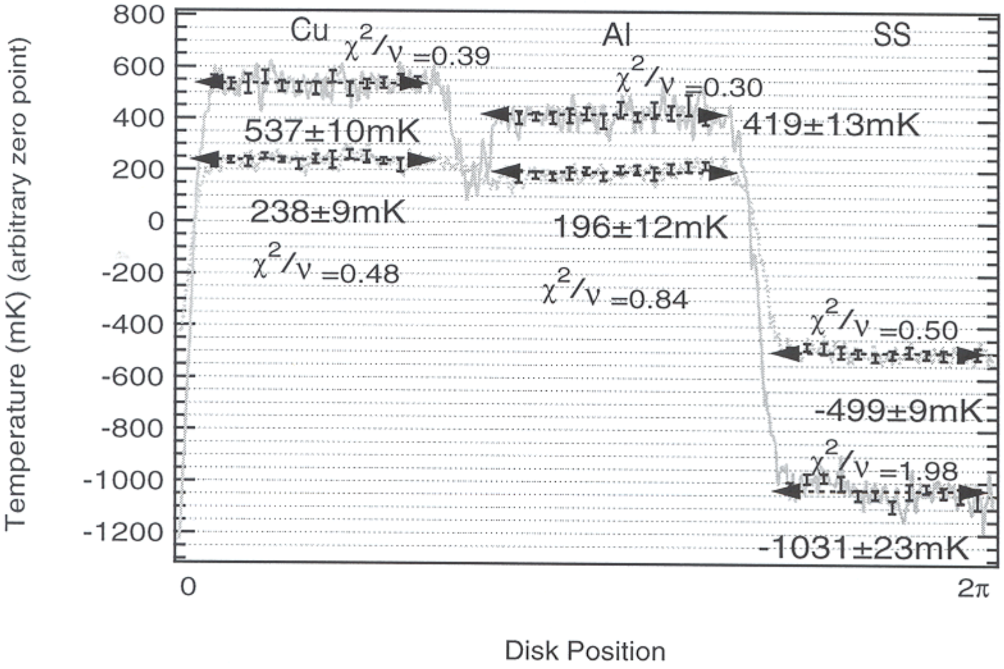

polarization, we set the relative uncertainty in the system calibration to be roughly 12%. This is only a rough figure because we are basing it on a small number of measurements (that we believe should be normally distributed). Reassuring, however, is the fact that this is enough uncertainty both to bring the measured mean into agreement with the theoretical value (Table 12) and to bring all of the measured calibration ratios into agreement with the R's suggested by the data.

As mentioned above, uncertainty in the calibration on this scale will not be of serious consequence. For the important measurements, the statistical uncertainty is already greater. However, it will be important in many other instances, such as determination of T_{sys}. (Section IVa)

The origin of this uncertainty is most likely in the actual act of measuring the calibrations. We have a few reasons for believing this; one of them is very

Figure 79. This is the third series format run for the Cu-Al-SS sample. Cu-Al-SS, Series 2. 3/5/98 The disk is flat to: $980\mu m$*. Data taken for* $n = 10000$ *sweeps, sampled at 1kHz, and filtered at 300Hz. The disk rotation frequency was 5/4Hz. Calibrations: Parallel (top graph) 2.11±0.25mV/K, Perpendicular (bottom) 3.30±0.40mV/K.*

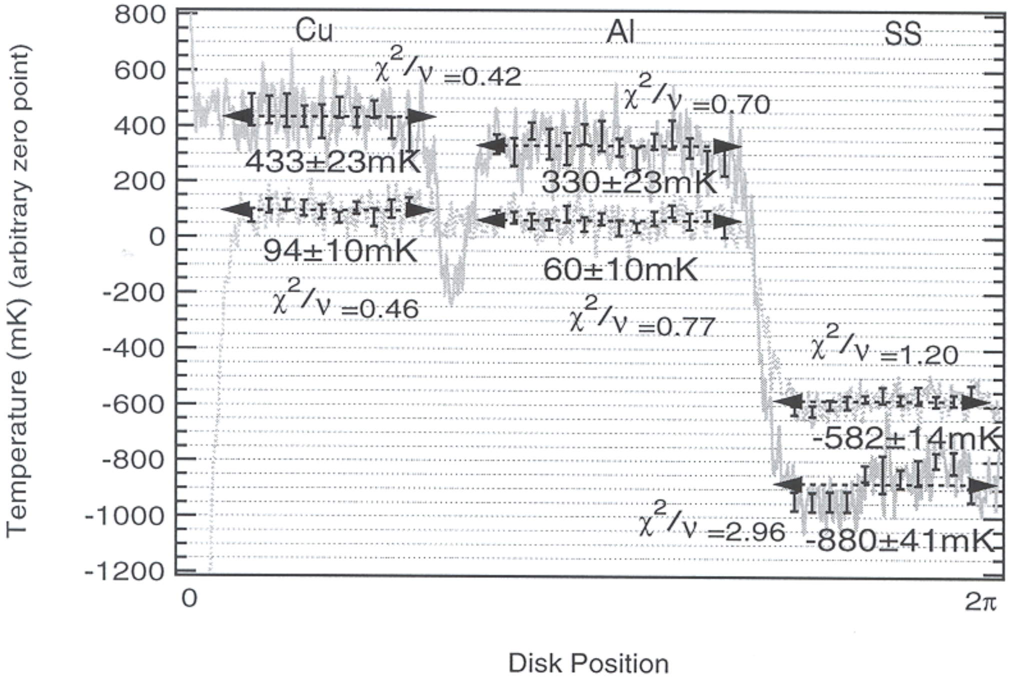

strong.

First, measurement of the calibration is often a difficult thing to do as the voltage output of the radiometer varies rapidly. Refer back to the second graph in Figure 58. Between twenty-ninth and the thirtieth calibration, the calibration jumps by nearly 10%. Thus, although, the slope of the curve describing the calibration increase is tiny, the actual measured calibration tends to jump around the fit curve substantially. It is often difficult to pick out the most representative value when measuring it.

That measurement is at fault is also suggested by our finding that the average ratio of the stainless–aluminum emissivity differences between the two polarizations is so close to 2. We have not been consistently measuring the calibration ratio too small. We have been measuring it both too small and too large.

Table 13: Values for the calibration ratio R for three samples. Also reported are the measured values for the calibration ratio along with the error we have determined to accompany them. Also reported is the average calibration ratio for the radiometer over the last two months.

	MAP VDA #1	MAP VDA #2	Cu-Al-SS
R	0.66	0.63	0.61
Measured Ratio	0.75 ± 0.13	0.76 ± 0.13	0.69 ± 0.11
Average Ratio for The Last Two Months:			0.64 ± 0.02

The most compelling evidence for measurement error is found when we calculate the average calibrations for each polarization taking into account all of the measurements we have made. We have twenty-eight pairs of calibrations for the final setup of the radiometer, measured over a period of two months, that we can treat statistically. Using the standard deviation of the mean as the uncertainty, we find for the calibration of the parallel polarization: 2.30±0.05mV/K. We find for the perpendicular polarization: 3.60±0.09mV/K. Our evidence for measurement error is the ratio: 0.64±0.02. This falls right in the middle of the R values calculated for Table 11. This both justifies our interpretation of the inconsistencies in the data as resulting from measurement and provides further evidence for the underlying consistency of the system.

We conclude this section by representing Table 11 for the measured and implied calibration ratios including a 12% relative uncertainty on all calibrations. We also include the average calibration ratio. All ratios are now consistent.

A 12% uncertainty in the calibration has been propagated through all calculations involving the calibration.

Vf5. Systematic Effects Due to the Polyester Tape

To see the effects of the polyester film tape used to fasten samples to aluminum disks, we performed three controlled experiments. We measured the Cu-Al-SS sample with and without tape over its seams. We measured the Lowered Al sample with and without tape over the machined edges separating the -245μm section from the rest of the disk. Finally, we measured the plain bulk aluminum disk with two pieces of tape radially outward as though enclosing a sample. Under one of these pieces we attached a 980μm diameter wire to simulate the effect of a sample edge higher than the rest of the disk. On all plots, temperatures are inverted such that larger emissivities correspond to lower temperatures.

From these tests, we learned two important things about the tape. First, it is quite emissive compared to bulk aluminum, especially in the parallel polarization. (Figure 62) Note that this is not the polarization you would expect from Maxwell's equations. (see Section Vf2) It seems to be a more complicated effect than a simple application of the field boundary conditions can explain. This is true for the untaped edges of the Cu-Al-SS sample as well. Second, the signal spikes that the tape produces are localized and do not affect appreciably the signal over the sample.

Figure 62 shows the signal from the tape on the flat aluminum disk. Here the tape has nothing underneath it and is itself flat. The signal increase in the parallel polarization is at maximum about 1.5K. In the perpendicular polarization, it is approximately 0.25K. The same size signals are evident in the Cu-Al-SS sample as well. Figure 63 shows the parallel polarization with and without tape.

Emissivity differences calculated for the Cu-Al-SS sample with and without tape (Table 14) are entirely consistent. Thus although the tape does cause

Figure 62. Section of the Bulk Al (6061-T6) disk with a piece of polyester film tape radially outward from disk center. The temperature scale is inverted. The spike in the data is due to the tape. The emissivity of the tape looks largest in the parallel polarization.

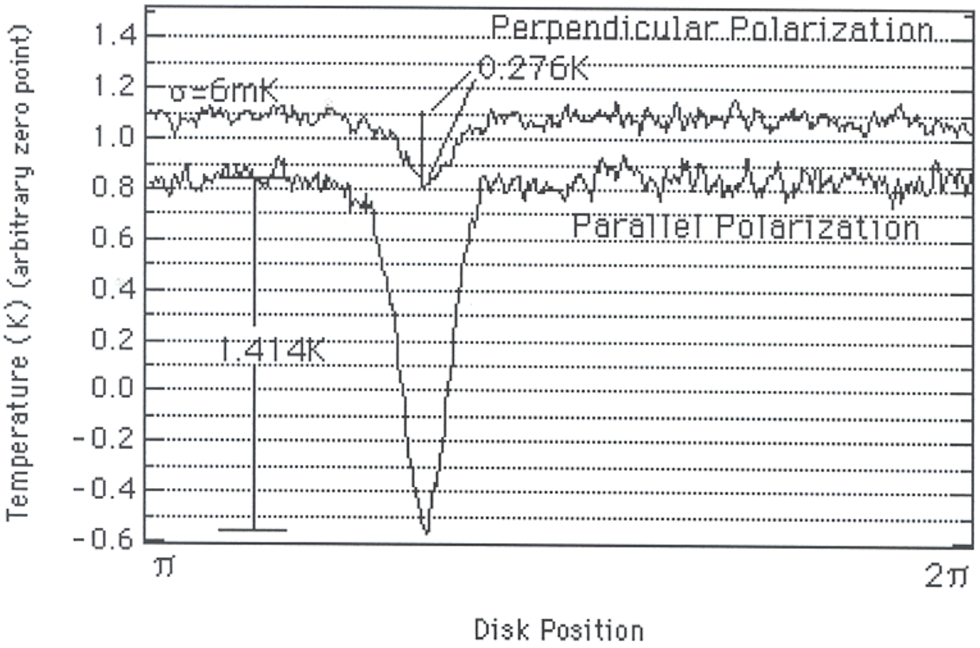

Figure 63. The Cu-Al-SS sample with and without tape in the parallel polarization. The temperature scale is inverted. The tape produces larger signals at the sample edges.

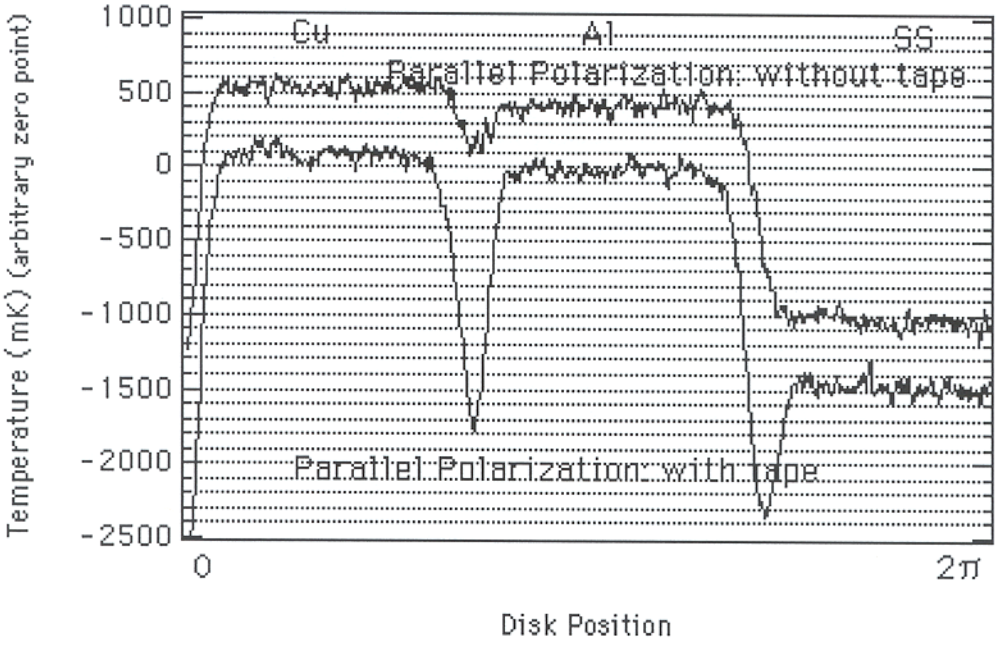

large signals at the sample boundaries, the effect does not appear to carry over appreciably onto the sample itself.

Table 14: Emissivities relative to bulk aluminum (6061-T6). $(e - e_{Al}) \times 10^4$. *A minus sign indicates that the sample is less emissive than Al 6061-T6. We have included the 12% uncertainty in the system calibration.* $E_{\|}$ *denotes the parallel polarization and* $E_{\perp}$ *denotes the perpendicular polarization.*

Cu-Al-SS

	Copper		Stainless Steel	
	$E_{\|}$	$E_{\perp}$	$E_{\|}$	$E_{\perp}$
Series 1 (tape)	-4.49 ± 1.90	-1.48 ± 3.06	68.05 ± 8.17	33.26 ± 3.99
" (no tape)	-5.47 ± 1.07	-1.95 ± 0.97	67.17 ± 8.06	33.20 ± 3.98

Figure 64. The Lowered Al sample with and without tape in the parallel polarization. Temperature scale inverted. The sample edge without tape looks more emissive than the edge with tape.

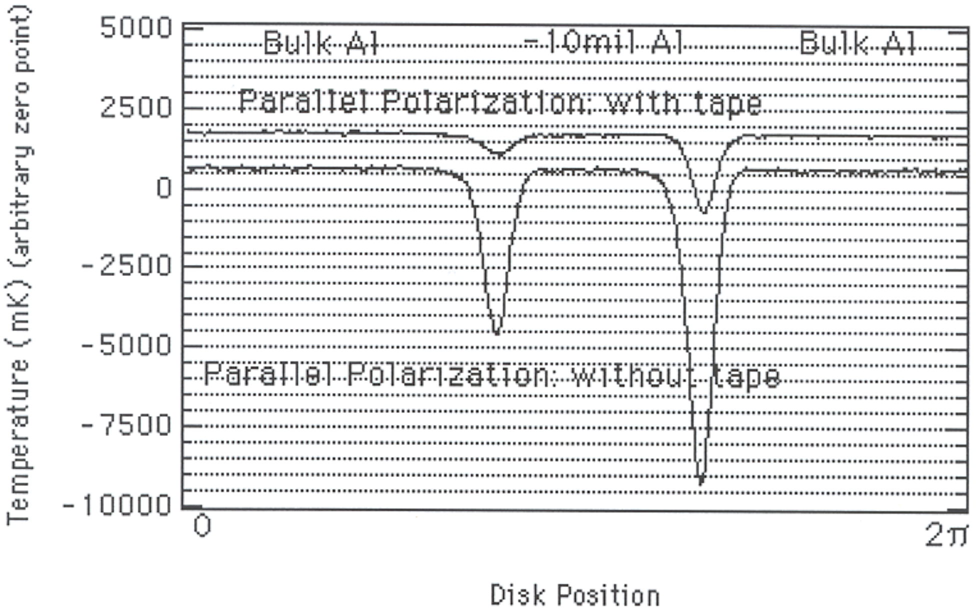

We find a similar result for the Lowered Al sample. Figure 64 shows the data for Lowered Al sample with and without tape in the parallel polarization. Here we notice that the tape makes the boundary of the sample appear less emissive. It hides the milled edge of the sample.

Figures 67 and 68 show blow ups of the two data sets (with and without tape) around the samples. It is apparent that the shape of the signal over the -245μm section is similar in each case, for each polarization. The slope of the signal in perpendicular polarization is somewhat greater for the sample with

Figure 67. The depressed aluminum sample with tape over the sample edges. -245μm Al (6061-T6), Series 1 (tape). 1/19/98 Flat to: 245μmDistance, feed to sample: 5.2cm. n=10800 sweeps. Sample Rate: 500Hz. Filtered at: 100Hz. Calibrations: Parallel (top graph) 2.32±0.28mV/K, Perpendicular (bottom) 3.94±0.47mV/K Polyester film tape is taped radially outward over the edges of the -245μm section.

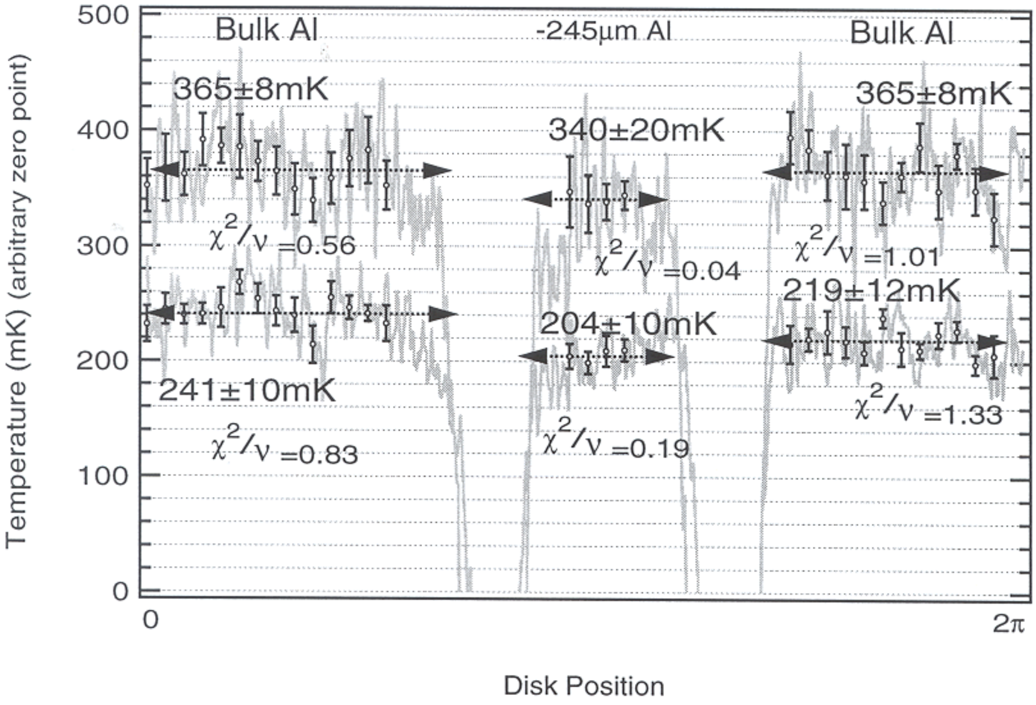

tape than the sample without. This suggests that the tape may have played a role in the smaller than normal emissivities we measured, as discussed above in section x, for MAP VDA in Series #1. However, the tape by itself does not explain the divergent values calculated for MAP VDA #1 as the tape's effect is to increase the emissivity, not to lower it.

The calculated emissivities for the Lowered Al sample are displayed in Table 15. The uncertainty ranges in both polarization for the sample with and without tape overlap. This provides further evidence that the tape does not effect the sample signal to a noticeable degree given the precision of our apparatus.

For a more quantitative description, we can very precisely constrain the degree to which the tape appears to affect the sample signal using the bulk Al

Figure 68. The depressed aluminum sample without tape over the sample edges. -245μm Al (6061-T6), Series 1 (tape). 1/19/98 Flat to: 245μmDistance, feed to sample: 5.2cm. n=10800 sweeps. Sample Rate: 500Hz. Filtered at: 100Hz. Calibrations: Parallel (top graph) 2.32±0.28mV/K, Perpendicular (bottom) 4.17±0.50mV/K Polyester film tape is taped radially outward over the edges of the -245μm section.

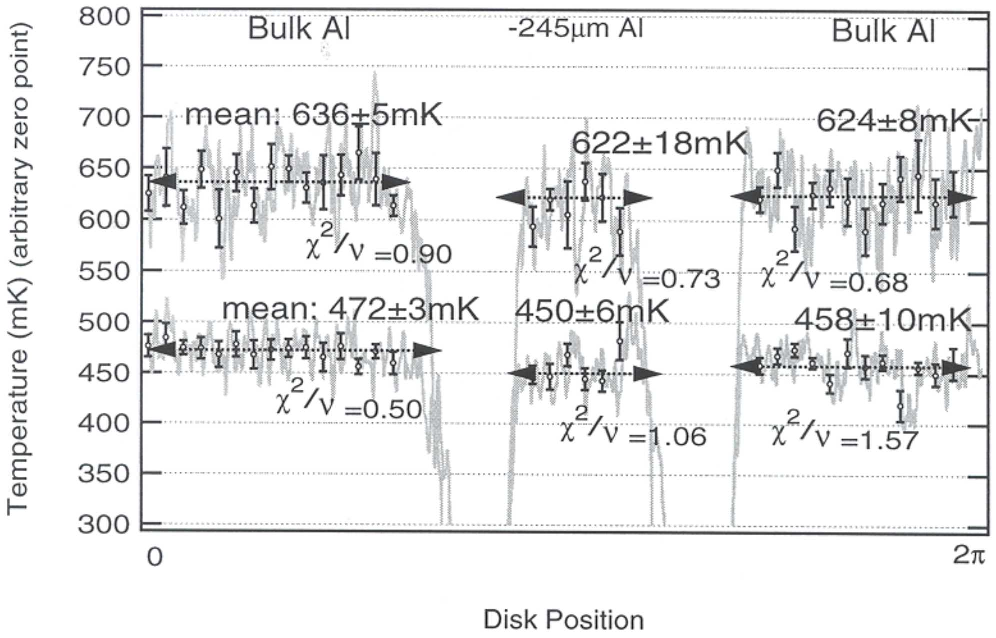

Table 15. Emissivities relative to bulk aluminum (6061-T6). $(e - e_{Al}) \times 10^4$. A minus sign indicates that the emissivity is less than that of bulk aluminum (6061-T6)

Depressed Sample: -245μm Al

	$E_{\parallel}$	$E_{\perp}$
Series 1 (tape)	1.16 ± 1.30	1.20 ± 0.97
Series 1 (no tape)	0.37 ± 1.13	0.70 ± 0.58

disk. From figure 65, we see that the raised piece of tape looks about 10 times more emissive in the parallel polarization and about 50 times more emissive in the perpendicular polarization at maximum than flat tape.

Figure 66 shows a blow-up of the flat aluminum disk with and without the two pieces of polyester tape. The top section of the plot contains data in the perpendicular polarization, and the bottom contains data in the parallel. As both measurements (i.e., with and without tape) were performed under identical circumstances, only adding or removing the tape from the disk sur-

Figure 65. Section of the Bulk Al (6061-T6) disk with a piece of polyester film tape radially outward from disk center. There is a 980μm diameter wire beneath the tape to simulate the effect of tape between two edges of different heights, as when the sample is not inset exactly flush within the aluminum disk. With the 980μm wire, the signal from the tape is far larger.

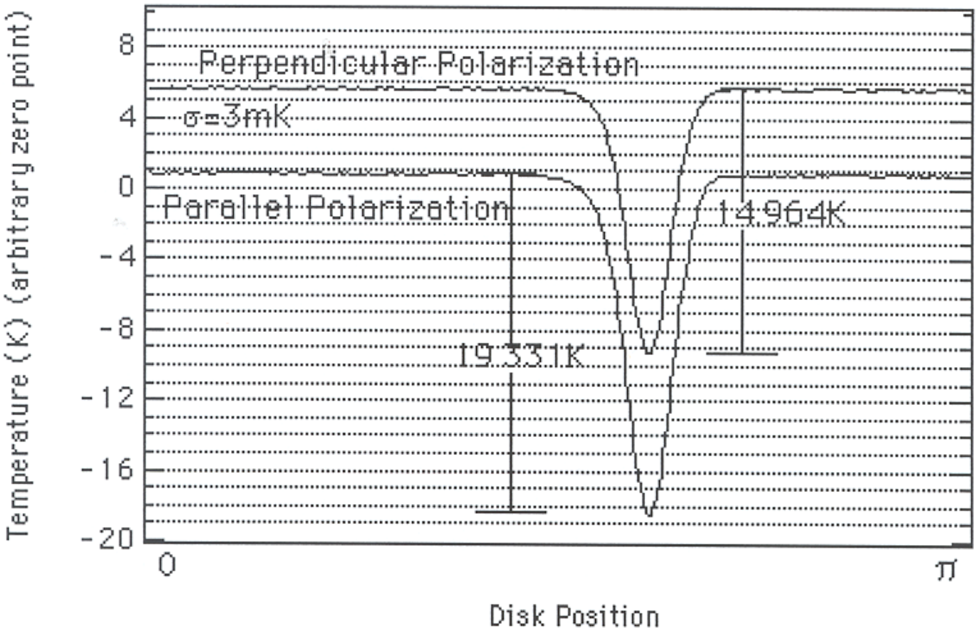

face, we can compare the two signal to isolate precisely the effects of the tape. Table 16 shows the calculated emissivity differences between the section of disk within the two pieces of tape and that without. These values are labeled "uncorrected" for reasons that will soon become apparent. The difference for each polarization is tiny, on the order of 10^5. We can check to see that this emissivity increase is due to the tape alone, and not a relic of the unflatness of the disk or some other systematic effect, by comparing the signal to the disk without tape. The apparatus is identical in both cases except for the presence of the tape.

We do this by averaging the Al disk without tape into three sections as with the taped disk. The sections that we averaged are marked by dashed vertical lines. Next we subtract the average signal from the taped disk from that of the plain disk for each of the sections. These average differences are

Figure 66. Bulk Al Disk (6061-T6), Series 1. 1/22/98 The aluminum disk with tape alongside the disk without tape. The top of the graph is the perpendicular polarization; the bottom is the parallel. Signal means are calculated for each in the sections away from the tape. The differences between signals of the same polarization are displayed in the gray boxes at the bottom of each section. These are uncorrected for the relative voltage drift between signals. The corrected numbers are in parentheses. The least squares fit slopes for each data set, excluding sections around tape, are reported.

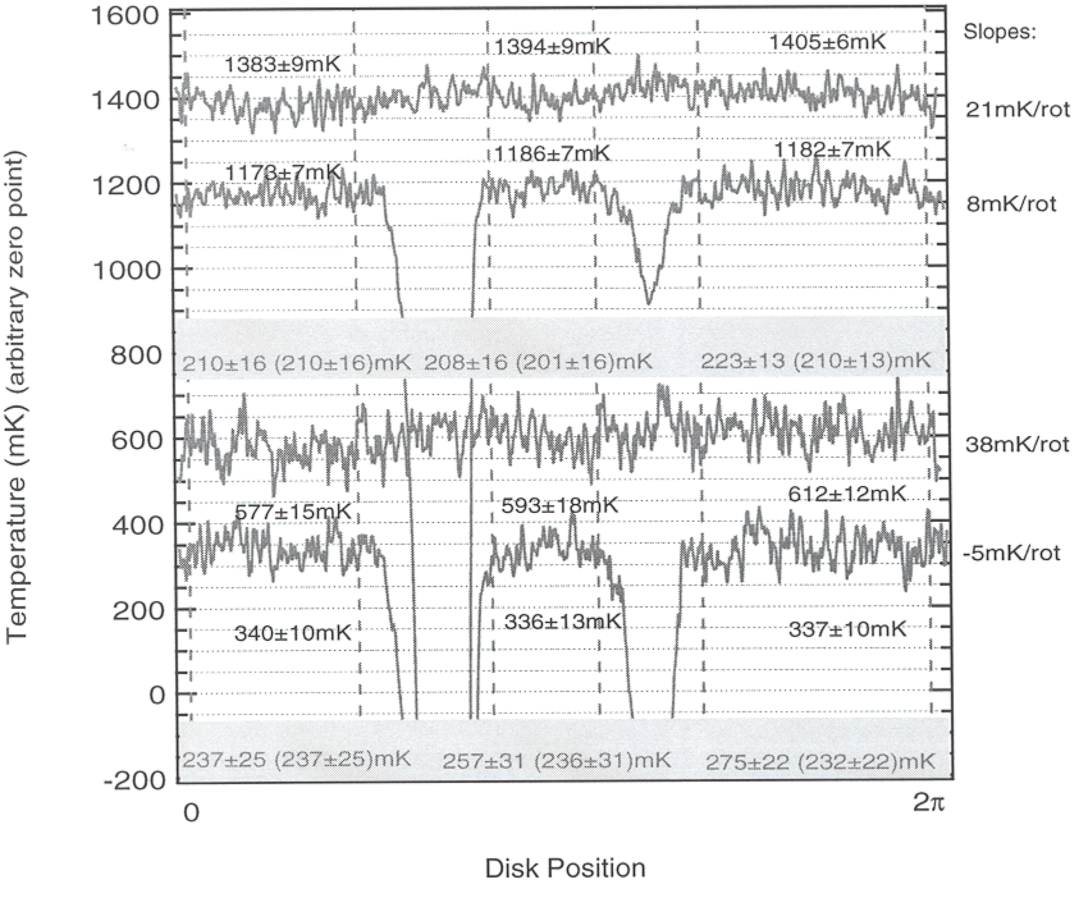

Table 16: Emissivity differences between a section of 6061-T6 Bulk Al between two sections of polyester tape and the rest of the Bulk Al disk. Uncorrected values are those calculated from the sample signal alone. Corrected values are those corrected against an untaped Bulk Al disk. || denotes the parallel polarization. ⊥ denotes the perpendicular polarization.

Bulk Al Disk

	$E_{\parallel}$	$E_{\perp}$
Uncorrected	0.12 ± 2.52	0.39 ± 1.41
Corrected	0.07 ± 2.52	0.41 ± 1.41

reported in Figure 66 in the gray boxes below each data set.

There is still, however, the possibility of a relative drift upwards or downward between the signals we are subtracting. This would be due to the drift in the radiometer which would be slightly different for each measurements because they were made at different times. Therefore, we find the least squares fit for each set of data and subtract it before proceeding. The slopes of each fit are reported in Figure 66. The largest value, 38mK per disk rotation, correspond to a drift of less than 0.1mV/s. This is too small to have been noticed and corrected for while taking data.

The signal difference values with the drifts subtracted away are displayed in the gray boxes in brackets in Figure 66. Table 16 displays the emissivity differences we calculate with these numbers alongside the ones we calculated before comparing to the untaped aluminum disk. The new values are labeled "corrected." The numbers we find are consistent with those from before. This is a good sign for the stability of our system.

We see from Table 16 that all data is consistent with a zero emissivity increase. Our conclusion is that further error allotments to take into account the effects of the polyester tape are unnecessary.

Table 17. Emissivities relative to bulk aluminum (6061-T6). $(e - e_{Al}) \times 10^4$. *A minus sign denotes less emissive than the aluminum. All samples have tape over the sample edges. The first values for the +490μm Al sample are from data under the section Early. All others are from Series 1.*

	$+490\mu$m Al	-245μm Al	$+490\mu$m SS
Parallel	1.60 ± 0.42		
Perpendicular	0.83 ± 0.51		
Parallel	1.41 ± 2.18	1.16 ± 1.30	66.52 ± 7.98
Perpendicular	0.44 ± 1.16	1.20 ± 0.97	33.63 ± 4.04

Vf6. The Sample Height

As mentioned in Section Ib, the two MAP VDA samples are slightly higher than the surrounding aluminum. MAP VDA #1 is 120μm higher and MAP VDA #2 is 25μm higher. In order to decide whether or not this height difference affected the measured emissivities, we performed three tests.

We perform two measurement, one from Early (Figure 69) and one from Series 1, (Figure 70) of the sample which has a section of plate aluminum (6061-T6) 490μm higher than the bulk aluminum (also 6061-T6) in the disk. We measure the sample in which a section of the bulk aluminum (6061-T6) has been milled out -245μm. (Figure 72) Finally, we measure the sample which has a section of 490μm thick AISI 304 stainless steel mounted to bulk aluminum. (Figure 71) All samples have polyester film tape along their edges. Calculated emissivity differences are displayed in Table 17.

The results for the emissivity difference between aluminum and stainless steel are within the ranges of those measured earlier (Table 12) for the Cu-Al-SS sample. Unfortunately, the dominant source of uncertainty here is in the system calibration. We cannot uncover the effects of the sample height. Nonetheless, we include this sample for completeness.

For all plots in this section, the temperature scale has been inverted; lower temperatures on the plots correspond to larger emission.

From Table 17, we see that the aluminum samples, the raised and the low-

Figure 69. +490μm Al (6061-T6), Early. 11/14/97. Flat to: 245μm. n=13000 sweeps. Sample Rate: 500Hz. Filtered at: 100Hz. Calibrations: Parallel (top graph), Perpendicular (bottom) 5.10±0.61mV/K This is the first run of the +490μm Al sample. This is prior to OMT installation.

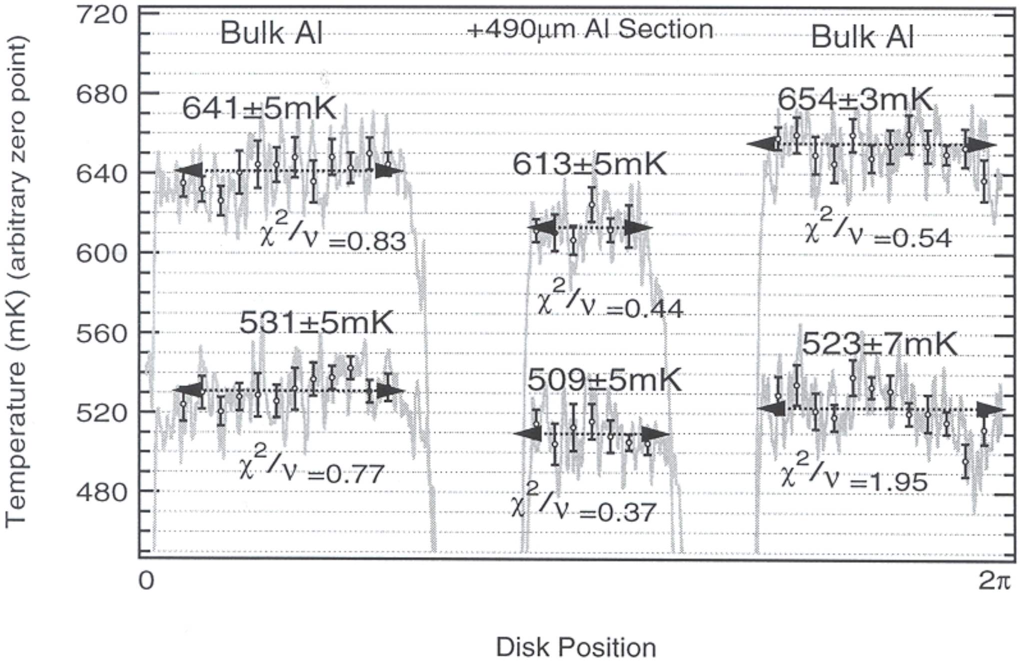

ered, both appear more emissive than the surrounding bulk aluminum. That the emissivity difference values for the raised and lowered samples are consistent for each polarization indicates that the cause of the emissivity increase is not the height of the sample per se. Rather, it is likely due to the change in height which allows a differing amount of 300K ambient radiation to be reflected into the feed.

We can estimate the uncertainty due to this effect by requiring that all values for the aluminum samples in Table 17 be consistent with a zero emissivity increase. This means an additional $\pm 1.18 \times 10^{-4}$ in the parallel polarization and $\pm 0.32 \times 10^{-4}$ in the perpendicular polarization. We include these uncertainties when considering all samples higher or lower than the bulk aluminum into which they are attached. This pertains to the two MAP VDA samples and the Greenbank sample.

Figure 70. +490μm Al (6061-T6), Series 1. 1/17/98 Flat to: 15mil. Distance feed to sample: 5.2cm. n=10200 sweeps. Sample Rate: 500Hz. Filtered at: 100Hz. Calibrations: Parallel (top graph) 2.55±0.31mV/K, Perpendicular (bottom) 4.17±0.50mV/K This is the second run of the +490μm Al sample, the first in a series format.

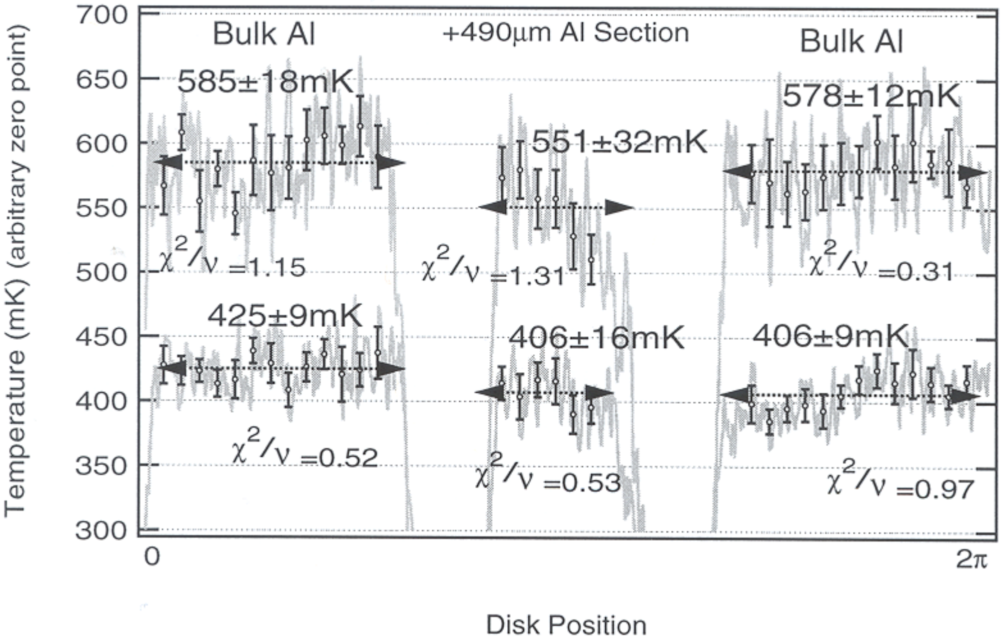

Figure 71. +490μm SS (AISI 304), Series 1. 1/16/98 Flat to: 368μm. Distance, feed to sample: 5.2cm. n=4200 sweeps. Sample Rate: 500Hz. Filtered at: 100Hz. Calibrations: Parallel (bottom graph) 2.32±0.28mV/K, Perpendicular (top) 3.71±0.44mV/K

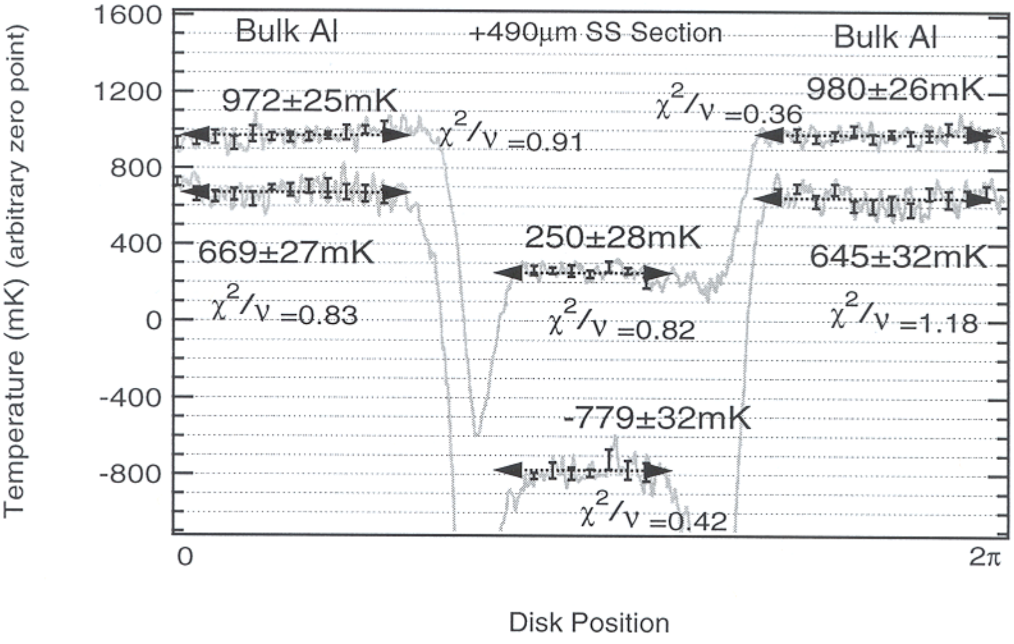

Figure 72. -245µm Al (6061-T6), Series 1 (tape). 1/19/98 Flat to: 245µmDistance, feed to sample: 5.2cm. n=10800 sweeps. Sample Rate: 500Hz. Filtered at: 100Hz. Calibrations: Parallel (top graph) 2.32±0.28mV/K, Perpendicular (bottom) 3.94±0.47mV/K Polyester film tape is taped radially outward over the edges of the -245µm section.

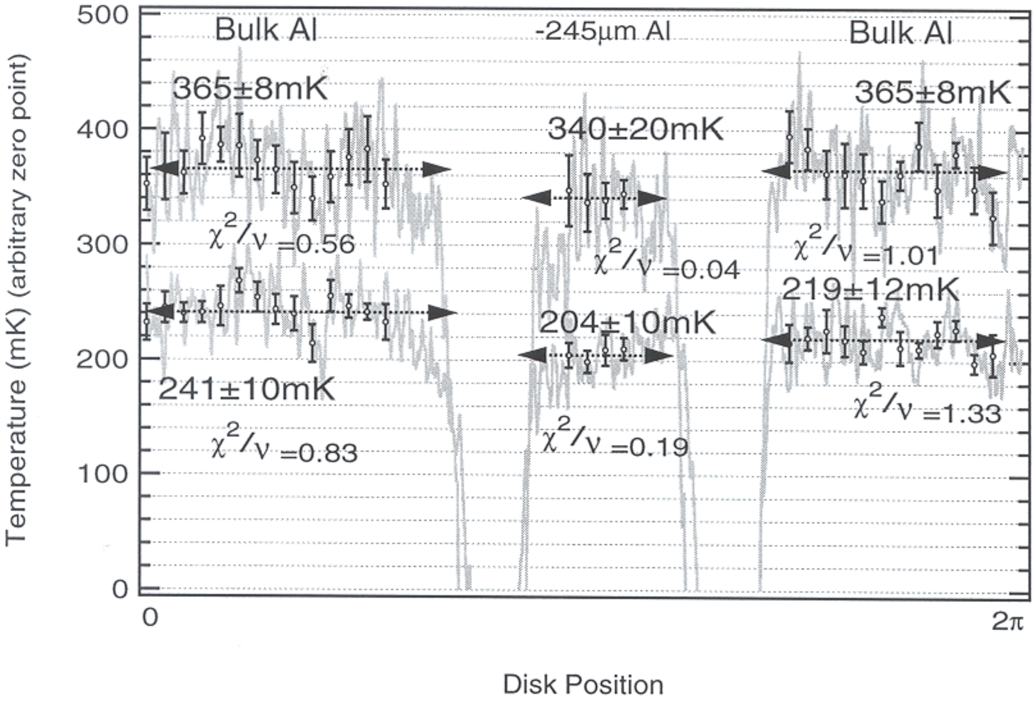

VI. Discussion and Conclusions

Tables 18 and 19 summarize the Δe measurements we have made for each of the two MAP VDA samples. These do not yet include uncertainties due to the calibrations or the sample height. We calculate the most probably value x_{mp} for each sample as the weighted average:

$$x_{mp} = \frac{\sum_{i=1}^{N} w_i x_i}{\sum_{i=1}^{N} w_i} \tag{67}$$

where the weights $w_i = 1/\sigma_i^2$. We then use for the error

$$\sigma_{mp} = \left(\sum_{i=1}^{N} w_i \right)^{-1/2} . \tag{68}$$

We calculate the most probable values and uncertainties in this way for all of the emissivity differences measured: MAP VDA #1, MAP VDA #2, Greenbank sample, copper-aluminum, stainless-aluminum. Next, we add the most probable uncertainty to that due to the sample height. (Section Vf6) Then we add in the error due to the calibration in quadrature. Finally, we correct all of these values to the calculated value for the emissivity of 6061-T6 aluminum. (Section IIa, Table 3) These absolute emissivity data are displayed, alongside the emissivities calculated from the model from Section IIa, in Table 20.

The most striking entries in Table 20 are those for MAP VDA #1 and MAP VDA #2 in the perpendicular polarization. Both mean values for the emissivities are below that of pure aluminum. The MAP VDA #2 result is consistent with an emissivity in the perpendicular polarization greater than that of pure aluminum, but the MAP VDA #1 result is not. As the VDA samples are made of aluminum, it is physically impossible for their emissivities to actually be less than that of pure aluminum.

One possible explanation would be that we used an incorrect value for the resistivity of Al 6061-T6. The emissivity scales as the square root of the

Table 18. Emissivities relative to bulk aluminum (6061-T6) at room temperature and 90GHz with $\theta_{inc} = 45°$. $(e - e_{Al})$. *A minus sign denotes less emissive than the aluminum. The parallel polarization is denoted by* $E_{\|}$. *The perpendicular polarization is denoted by* $E_{\perp}$.

MAP VDA #1.

Date	$E_{\|}$	$E_{\perp}$
10/31/97	$-2.59 \pm 1.53 \times 10^{-4}$	$-4.53 \pm 0.42 \times 10^{-4}$
12/10/97	$-2.18 \pm 1.48 \times 10^{-4}$	$-4.81 \pm 1.90 \times 10^{-4}$
3/4/98	$-2.13 \pm 3.01 \times 10^{-4}$	$-3.98 \pm 1.76 \times 10^{-4}$
Most Probable Value:	$-2.35 \pm 1.00 \times 10^{-4}$	$-4.51 \pm 0.40 \times 10^{-4}$

Table 19. Emissivities relative to bulk aluminum (6061-T6) at room temperature and 90GHz with $\theta_{inc} = 45°$. $(e - e_{Al})$. *A minus sign denotes less emissive than the aluminum. The parallel polarization is denoted by* $E_{\|}$. *The perpendicular polarization is denoted by* $E_{\perp}$.

MAP VDA #2.

Date	$E_{\|}$	$E_{\perp}$
1/6/98	$4.03 \pm 1.39 \times 10^{-4}$	$-2.69 \pm 0.93 \times 10^{-4}$
1/7/98	$2.87 \pm 0.88 \times 10^{-4}$	$-2.18 \pm 0.74 \times 10^{-4}$
1/16/98	$2.64 \pm 2.32 \times 10^{-4}$	$-2.59 \pm 0.97 \times 10^{-4}$
3/4/98	$1.85 \pm 2.04 \times 10^{-4}$	$-2.27 \pm 0.93 \times 10^{-4}$
Most Probable Value:	3.01 ± 0.67	-2.40 ± 0.44

Table 20. Absolute Emissivities for all materials measured and calculated, at room temperature and 90GHz and $\theta_{inc} = 45°$. *Calculated values are from the model in Section IIa and corresponding material names are in italics. The parallel polarization is denoted by* $E_{\|}$. *The perpendicular polarization is denoted by* $E_{\perp}$.

	$E_{\|}$	$E_{\perp}$	Ratio $e_{\|}/e_{\perp}$
Pure Al	$14.55 \pm 0.01 \times 10^{-4}$	$7.28 \pm 0.01 \times 10^{-4}$	2.0 ± 0.0
6061-T6 Al	$18.26 \pm 0.44 \times 10^{-4}$	$9.14 \pm 0.22 \times 10^{-4}$	2.0 ± 0.1
MAP VDA #1	$15.91 \pm 2.64 \times 10^{-4}$	$4.63 \pm 1.12 \times 10^{-4}$	3.4 ± 1.0
MAP VDA #2	$21.27 \pm 2.32 \times 10^{-4}$	$6.74 \pm 1.03 \times 10^{-4}$	3.2 ± 0.6
Greenbank	$40.73 \pm 4.64 \times 10^{-4}$	$14.47 \pm 2.00 \times 10^{-4}$	2.8 ± 0.5
AISI 304	$83.14 \pm 8.54 \times 10^{-4}$	$41.14 \pm 4.18 \times 10^{-4}$	2.0 ± 0.0
AISI 304	$75.76 \pm 0.21 \times 10^{-4}$	$37.95 \pm 0.11 \times 10^{-4}$	2.0 ± 0.0
OF Cu	$13.11 \pm 2.56 \times 10^{-4}$	$7.51 \pm 1.50 \times 10^{-4}$	1.7 ± 0.3
OF Cu	$11.63 \pm 0.07 \times 10^{-4}$	$5.82 \pm 0.03 \times 10^{-4}$	2.0 ± 0.0

resistivity (equations (22) and (23)). If we had used too low a value for the resistivity, then our emissivites would be too low as well. Figure 73 addresses this possibility with a plot of the mean emissivity in the parallel polarization

Figure 73. Plot of the ratio of the emissivity in the parallel polarization over the emissivity in the perpendicular polarization as a function of the resistivity of Al 6061-T6 for the mean of each of the two MAP VDA samples. The reported ρ for Al 6061-T6 is $41.7 \pm 1.7 n\Omega$-m.

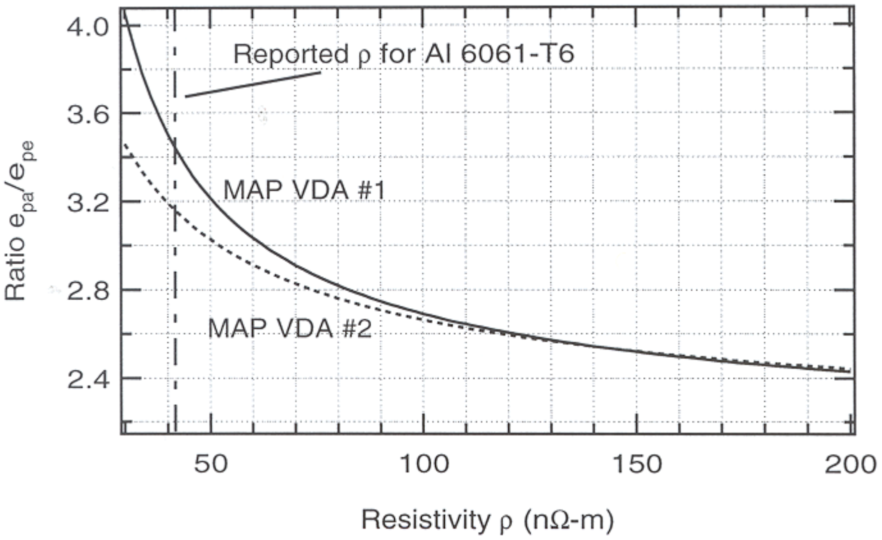

over the mean emissivity in perpendicular polarization as a function of the resistivity of Al 6061-T6. We look at the ratio because it allows us to keep track of what both polarizations are doing as the resistivity increases. We could certainly increase the resistivity enough such that the emissivity in the perpendicular polarization was no longer smaller than that of pure aluminum, but this would also increase the emissivity of the sample in the parallel polarization, possibly making it non-physically large.

We expect the ratio of the emissivities to be roughly equal to 2 as discussed in Section Vf4. We do not expect 2 exactly because the geometry of our setup is such that not all the radiation pattern is at 45°. From Figure 73, it is apparent that it will take an asymptotically large value for the resistivity of Al 6061-T6 for the mean emissivity ratio to be as near to 2 as we would expect. This conclusion is reached as well for all values of the emissivity ratios for each VDA sample within the uncertainties listed in Table 20. Therefore, we have no grounds to doubt our resistivity value for Al 6061-T6.

Another, possibility is that the emissivities are described by an incidence

Figure 74. Plot of the ratio of the emissivity in the parallel polarization over the emissivity in the perpendicular polarization as a function of incidence angle in degrees for aluminum. The ranges suggested by the data for MAP VDA #1 and MAP VDA #2 are boxed.

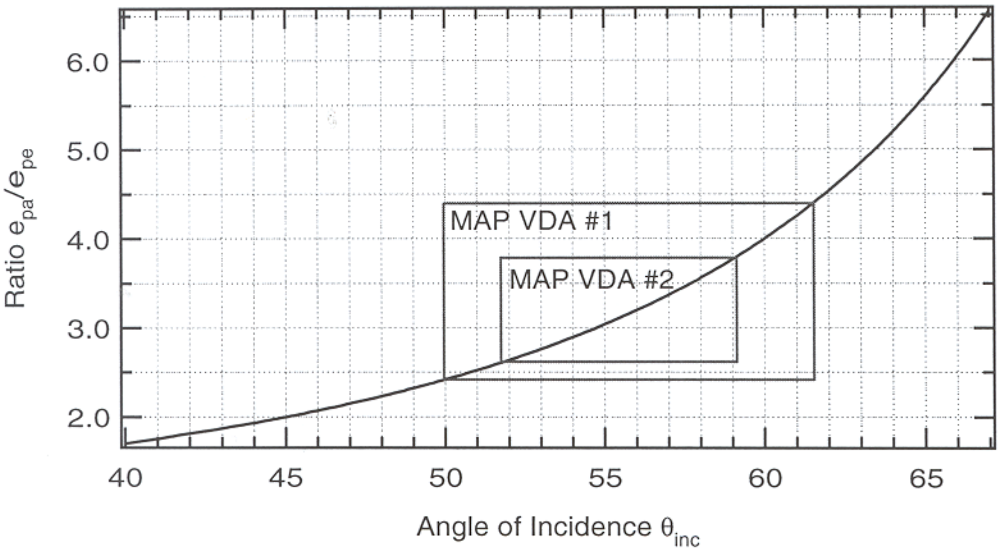

angle θ_{inc} other than 45°. This would be true if, for example, the apparatus were misaligned. We do not believe this to be the case as the alignment was meticulously checked before each measurement grouping. Listed in the far right side of Table 20 are the emissivity ratios for each sample. The ratio is a strong function of θ_{inc} as displayed in Figure 74. From this plot, we see that the incidence angle suggested by the data for MAP VDA #1 and MAP VDA #2 is in a range greater than 45°. This is also true for the Greenbank sample.

Three facts, however, keeps us from coming to the conclusion that our angle of incidence is simply wrong. First, from Table 20 and as noted in Section Vf4, the measured emissivity ratio for stainless steel is very close to 2. Second, the ratio for copper is consistent with 2 as well. Third, we saw when we rotated the polarizations by 45° that the system was practically identical between channels. (Section Vf3)

Therefore, as we have no mechanism to explain why the reflector samples should appear to have $\theta_{inc} > 45°$ while two other measurement sets (i.e. Cu and SS) are consistent and strongly imply $\theta_{inc} = 45°$, we are forced to expand

Table 21. Absolute Emissivities for all materials measured and calculated, at room temperature and 90GHz and $\theta_{inc} = 45°$. *Calculated values are from the model in Section IIa and corresponding material names are in italics.* $E_{\parallel}$ *denotes parallel polarization and* $E_{\perp}$ *denotes perpendicular polarization.*

	$E_{\parallel}$, $\theta_{inc} = 45°$	$E_{\perp}$, $\theta_{inc} = 45°$	Normal Incidence
Pure Al	$14.55 \pm 0.01 \times 10^{-4}$	$7.28 \pm 0.01 \times 10^{-4}$	$10.30 \pm 0.01 \times 10^{-4}$
6061-T6 Al	$18.26 \pm 0.44 \times 10^{-4}$	$9.14 \pm 0.22 \times 10^{-4}$	$12.9 \pm 0.31 \times 10^{-4}$
MAP VDA #1	$15.91 \pm 2.99 \times 10^{-4}$	$4.63 \pm 2.65 \times 10^{-4}$	$8.08 \pm 5.28 \times 10^{-4}$
MAP VDA #2	$21.27 \pm 2.67 \times 10^{-4}$	$6.74 \pm 2.56 \times 10^{-4}$	$11.42 \pm 5.51 \times 10^{-4}$
Greenbank	$40.73 \pm 4.99 \times 10^{-4}$	$14.47 \pm 3.53 \times 10^{-4}$	$23.90 \pm 8.43 \times 10^{-4}$
AISI 304	$83.14 \pm 8.89 \times 10^{-4}$	$41.14 \pm 5.71 \times 10^{-4}$	$57.59 \pm 7.48 \times 10^{-4}$
AISI 304	$75.76 \pm 0.21 \times 10^{-4}$	$37.95 \pm 0.11 \times 10^{-4}$	$53.67 \pm 0.16 \times 10^{-4}$
OF Cu	$13.11 \pm 2.91 \times 10^{-4}$	$7.51 \pm 3.03 \times 10^{-4}$	$10.62 \pm 4.29 \times 10^{-4}$
OF Cu	$11.63 \pm 0.07 \times 10^{-4}$	$5.82 \pm 0.03 \times 10^{-4}$	$8.22 \pm 0.05 \times 10^{-4}$

our systematic uncertainty allotments. We add an uncertainty of ±1.53 to all measurements made in the perpendicular polarization and an uncertainty of ±0.35 to all measurements made in the parallel polarization. These are the minimum uncertainties that allow for all MAP VDA measurements in the perpendicular polarization to be consistent with an emissivity equal to that of pure aluminum. Also, it is enough uncertainty such that all emissivity ratios are consistent with 2.

We conclude by presenting all of our data, corrected with this additional uncertainty, for both polarizations. We also include in Table 21, the expected emissivities at normal incidence. This, by analogy with the discussion leading up to equations (22) and (23), should be equal to $\sqrt{2}$ times the emissivity in the perpendicular polarization and $1/\sqrt{2}$ times the emissivity in the parallel polarization.

Acknowledgements

Special thanks to: Lyman Page for nearly a year's worth of guidance and encouragement, Michael Kesden and Michael Desai for helping to build and run the apparatus, Bob Sorenson, Dick Bitzer, and Charles Sule for answering a million questions, Al and Ted in the student shop for your patience and assistance, everyone in the metal shop, Michele Limon for advice and help, Suzanne Staggs for a room in which to work, my family (including but not limited to: Mom, Dad, Jordan, Tyler, Grandma, Grandpa), my roommate Chris α, my study hall mates Adam Kessel and Jackie Lu, my carmic döppelganger James Forrest or Pete Rowinsky, Molly Graves for her constant assurances that the thesis lifestyle is unreal, everyone else at the 2 Dickinson Street Co-op (including but not limited to: Scarlet, Ransom, Craig, Sarah, Liz, Gillian, Bogac, Li, Brian, Rizwan, Heather, Amy, Tammy, Erica), members of WORF (including but not limited to: James Weaver, Fred Weaver, Justin Brocious, Joel Mack, Josh Shugarts), members of NINJA (including but not limited to: James Weaver, Fred Weaver, Justin Brocious, Joel Mack, Josh Shugarts), resident and non-resident members of 301/2 Feinberg, physics department seniors, Jah.

References

Boyer, H. E., Gall, T. L. *Metals Handbook.*American Society for Metals. Metals Park, Ohio : 1984, c1985.

Evans, G. *RF Radiometer Handbook.* Artech House. Dedham, MA: 1977.

Guillien, R. *Sur la variation de la constante diélectrique a la solidification des liquides homopolaires. (Regarding the Change of the Dialiectric Constant of Homopolar Liquids on Solidification.*Compt. rend. **207**. 393-5; C. A. **32**, 7791 (1938)

Heald, M. A., Marion, J. B. *Classical Electromagnetic Radiation.* Third Edition. Saunders College Publishing. New York, NY: 1995.

Horowitz, P., Hill, W. *The Art of Electronics.* Cambridge University Press. Cambridge: 1980.

Kraus, J. D. *Radio Astronomy.* 2nd Edition. Cygnus-Quasar. Powell, OH: 1986.

Pozar, D. M. *Microwave Engineering.* Addison-Wesley. New York, NY: 1993.

Press, W. H., Teukolsky, S. A., Vetterling, W. T., Flannery, B. P. *Numerical Recipes in C.* Cambridge University Press. Cambridge: 1992.

Reed, R., P., Clark, A., F. *Materials at Low Temperature.* American Society for Metals. Metals Park, Ohio: 1983.

Touloukian, Y. S., Ho, C. Y. *Thermal Radiative Properties: Metals, Elements, and Alloys.* Vol. 7. IFI/Plenum. New York, NY: 1979.

Appendix A: Data and Specifications Sheets

ARC TECHNOLOGIES
THE NEW WAVE
RADAR ABSORBING MATERIALS

CERTIFICATE OF COMPLIANCE

This form certifies that the products for the referenced purchase order have been manufactured and tested to meet all required specifications per the corresponding drawings and/or data on file at ARC Technologies, Inc. at the time of shipment

Customer: PRINCETON UNIVERSITY
PHYSICS DEPT.
WASHINGTON ROAD
PRINCETON, NJ 08544

Item #	Description	Quantity
1	ARC-RT-10003	10

Purchase Order #: S002-9372-98
Ship Date: 03/12/98
ARC S.O. #: 980147
Shelf Life: N/A

Quality Control:
Brian W. Peavey, Jr.

11 CHESTNUT STREET AMESBURY, MA 01913
(508) 388-2993 (508) 388-6866 FAX

Communication from Surface Optics Corporation

Subject: Re: Specifications for the 12 by 12 samples sent East
Date: Tue, 14 Apr 1998 10:36:51

Coating Dates	Sample
8-1-97	2.8 µm Al 2.5 µm SiOx
10-15-97	2.5 µm Al 1.1 µm SiOx (MAP VDA #1)
12-20-97	2.15 µm Al 2.4 µm SiOx (MAP VDA #2)

Sample ID	FS8557	FS8626	FS8782
Al Thickness	2.8µm	2.5µm	2.15µm
SiOx Thickness	2.5	1.1µm*	2.4µm
Solar Absorbtance	.589	.394	.299
Emittance** (300)	.695	.524	.621
BRDF % outside 10			95.06

* This thickness was estimated to be 1.8 um by J.H.
** Emittance is calulated in band at near normal incidence only.

GBT Goldstone Paint Sample
(ave = 3.79 +/- 0.14 mils)

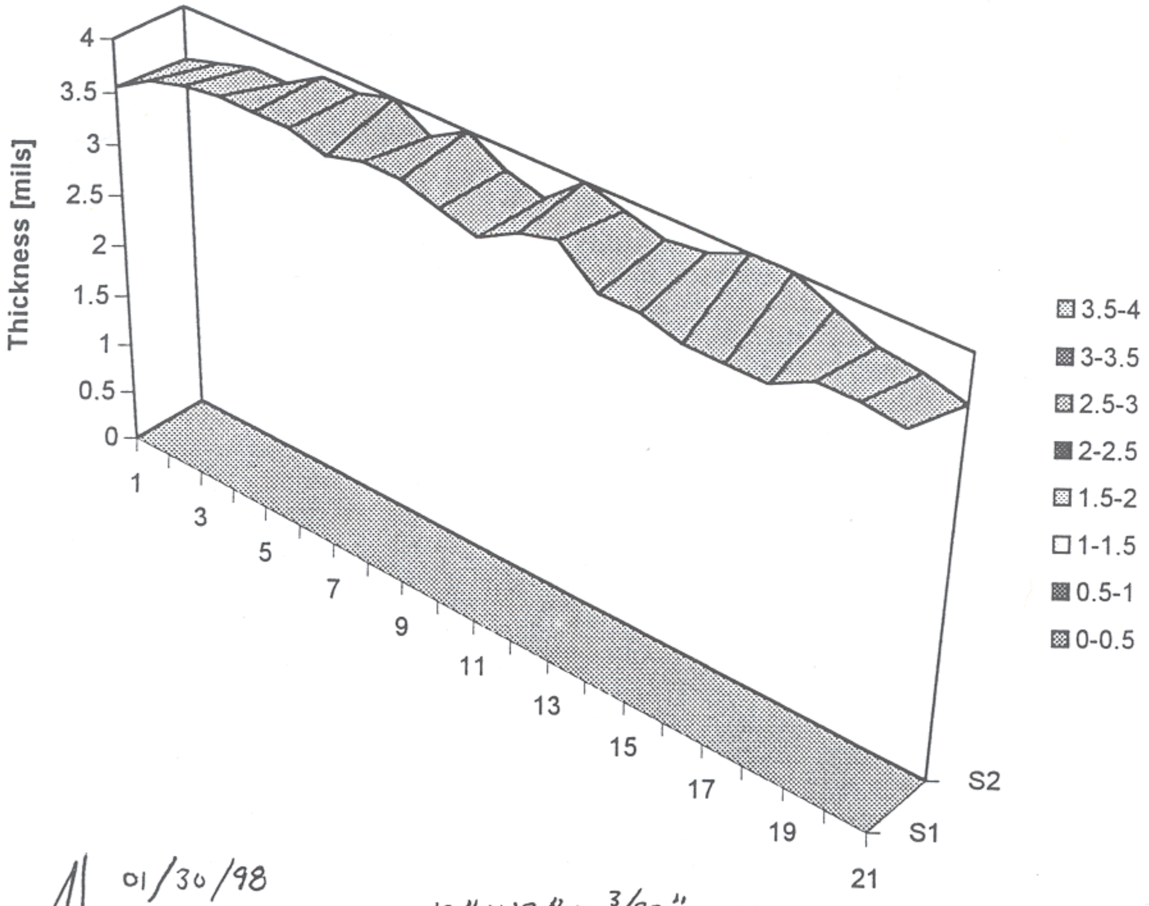

01/30/98

SAMPLE Ⓑ

12" x 12" x 3/32" AL PLATE WITH GOLDSTONE™ PAINT

$t_{PAINT} \simeq$ 3.8 ± 0.14 mils

$t_{PAINT} + t_{AL} \simeq$ 0.090 ± 0.001

roduct # 500HR5

Goldstone™ TriThane Formula

Acrylic Urethane , High Reflectance, Microwave Antenna Coating

APPLICATION DATA

REQUIREMENTS FOR APPLICATION:

All substrates must be dry and in sound condition. Remove oil, dust, loose rust, peeling paint or other contamination to ensure good adhesion. For maximum durability of paint system, prepare the steel for painting in accordance with SSPC-SP6, Commercial Blast Cleaning. Minimum surface preparation should be no less than SSPC-SP2, Hand Tool Cleaning or SSPC-SP3, Power Tool Cleaning. On smooth metal, etching the surface is necessary. The use of iron phosphate preparation will enhance the adhesion of topcoat or primer to most metal surfaces. **500HR6** is recommended for direct application to properly prepared fiberglass but all other substrates should be primed.

- Surfaces must be dry and protected from all moisture until rainproof as per chart above.
- Both surface and ambient temperature must be + 45°F and + 5°F above the dewpoint. Maximum recommended temperature is 110°F surface and 95°F ambient.
- Fiberglass and surfaces previously painted with **500HR6** or equivalent must be sanded to dull. For a fine finish on any sanded surfaces, finish sanding with very fine 400 – 600 grit sandpaper and dry brushed or vacuumed to remove all dust.

PRIMING:

Sheet metal	941P Tripoxy Primer
Aluminum	994P PreEtch+900P Envirotech Primer
Galvanized Steel	945P AquaPrime
Iron/Steel	941P Tripoxy Primer

FILM DEVELOPMENT & THICKNESS:

Recommended film thickness varies with use. In non corrosive atmospheric service, a two mil DFT is recommended. The use of two distinct coats is highly recommended as insurance against pinhole voids. Two coats each with a 2 mil DFT are also recommended on surfaces subject to intermittent submersion. **Goldstone TriThane** can be recoated during the tack stage of drying. **500HR6** series dries very quickly which allows multiple coats to be applied at one time. However, if **500HR6** dries for 90 – 120 min. it must be allowed to dry completely for 8 hours before it is recoated.

MIXING:

Catalyzing: Mix ratio is 7:1. Pour Part B in to Part A while stirring, *then reduce*. When preparing smaller quantities, recommend staying in quart increments (28 fl.oz. of 500 to 4 fl.oz. of hardener).

Pot Life: Pot Life will vary slightly with temperature and humidity but when reduced to spray viscosity, pot life will be at least 6 hours in all conditions.

THINNING:

Add Hardener before reducing. Designed for a 25 – 50% reduction when applied by conventional spray and 5 – 15% when applied by airless. Two reducers are used:

• AT46	Medium, 45° – 65° F.
• AT70 + AT46	Medium slow, 65° – 95° F.
• AT70	Slow, above 95° F.

APPLICATION:

500HR6 is specifically designed for conventional spray but is amenable to HVLP and air assist airless but these two methods require the use of slower solvents. Airless spray is recommended for large surface maintenance painting such as tanks, large beams, etc. High ratio pumps are required. Typical ⅓ – 1 gpm house pumps do not develop enough pressure for proper atomization.

CLEANUP: .... AT17 Wash Thinner

Rinse tools with clean AT46.

SAFETY AND HANDLING

FLASH POINT: [Part A] .... 68° F. (16° C.)
FLASH POINT: [Part B] .... 81° F. (16° C.)
SHIPPING DESCRIPTION: [CFR 49]
Ground/Air/Vessel: ..... Paint, 3, UN1263, PG II
Required Label: .... FLAMMABLE LIQUID
Required Marking: .... PAINT UN1263
IMDG PACKAGING:
FLAMMABLE LIQUID, class 3.2, UN1263, II
IMDG STOWAGE: .... Category B
UNIFORM FIRE CODE: [CFR 29] .... CLASS I-B
STORAGE TEMPERATURE: .... 120° F. max.
SHELF LIFE: [warranted] .... 1 Year
"HMIS" RATINGS: .... H - 2; F - 3; R - 0; PP - H

(01/21/98)

Product # 500HR6

Goldstone™ TriThane Formula

Urethane Enamel, High Reflectance, Microwave Antenna Coating

SELECTION DATA

DESCRIPTION:

Goldstone 500HR6 is a specially formulated coating designed to have high infrared radiation reflectance. It is formulated for the NASA Deep Space Instrumentation Facilities (DSIF) to protect microwave antennas from heat accumulation. This coating is also used to protect large dish telescopes and radio receivers. **Goldstone** is intended for spray application. It is designed for HVLP air spray and HVLP air assisted airless systems but, where legal, it can be applied with conventional or airless systems. **Goldstone 500HR6** is a 500 g/l VOC compliant, high performance, two component, air or forced dry, acrylic aliphatic urethane enamel. **Goldstone 500HR6** is hard drying but with a resilient, leather like toughness that gives it unsurpassed impact and abrasion resistance. In addition, it is water impermeable, fully resistant to atmospheric exposure to chemicals and resistant to splash and spill type contact with most chemicals. This is a 7 to 1 mix.

USE:

Goldstone typical applications include; microwave antenna dishes, radio receivers, large dish telescopes or where a high infrared diffused reflection is needed.

ADVANTAGES:

- Meets 500 g/l VOC as applied.
- State of the art color retention, abrasion and chemical resistance.
- High infrared diffusion properties reduced surface temperature.
- When used as a complete Triangle system, it does not distort or obstruct transmission and receiving signals.

LIMITATIONS:

- When applied, may not meet local air quality regulations.
- Not recommended for sustained direct chemical contact, permanent submersion in water or below grade use.

PHYSICAL PROPERTIES

VOC: [catalyzed] .... 422 g/l – (3.53 lbs./gal.)

APPEARANCE: [Gloss at 60°]

Flat (F) .... 5 – 10

WEIGHT PER GALLON: [catalyzed] .... 10.4 lbs.

FLASH POINT: [catalyzed] [setaflash] .... 68° F.

PACKAGE VISCOSITY: [catalyzed] .... 65 – 75 KU

SOLIDS: [catalyzed]

By Weight .... 69 ± 1%
By Volume .... 52 ± 1%

COVERAGE: [catalyzed]

Theoretical at 1 mil DFT .... 834 sq.ft./gal.
Theoretical at 1.5 mils DFT .... 556 sq.ft./gal.
[Recommended DFT per coat (1 or 2 coats) 2.0–2.5 mils.]

DRY SCHEDULE: [at 50% RH and 2 mils DFT]

	45° F.	*60° F.*	*75° F.*	*90° F.*
Tack free	3 hrs.	90 mins.	45 mins.	30 mins.
Handle	10 hrs.	4 hrs.	2 hrs.	1½ hrs.
Rainproof	28 hrs.	12 hrs.	6 hrs.	4 hrs.
Recoat	24 hrs.	12 hrs.	10 hrs.	8 hrs.
Full cure	7 days	4 days	10 hrs.	8 hrs.

ORDER NUMBER AND COLOR:

500HR6 .... TriThane Flat White
TriThane Hardener 500B

COLOR AVAILABILITY:

The **Goldstone 500HR6** is packed as White only. Any color can be made with 25 gallon minimum order.

PACKAGING:

One gallon kit .... 50 lbs.
One gallon ⅞ full (112 fl.oz.) fill of Part A & one pint (8 fl. oz.) fill pint can of Part B.

Five gallon kit .... 60 lbs.
One each 4⅜ gallon fill in a 5 gallon can of Part A & a ⅝ fill 1 gallon can of Part B

TRIANGLE COATINGS, INC.
Tel: 510-895-8000
800-895-8000
Fax: 510-895-8800
TRIANGLE

FEED & OMT SPECIFICATION

This note establishes the specification of the *MAP* feeds. Many have contributed to its contents including especially Ken Hersey, Michele Limon, and YRS Associates. This note supercedes the May 26, 1997 version.

Introduction & Overview

Feeds The *MAP* feeds were designed by YRS Associates. Each feed is tailored to the shaped optical system. The full near field expression for the electric field as determined from a spherical wave expansion is used to determine how the feed illuminates the subreflector.

For each band, a slightly different strategy is employed. The natural conic length of the K band feeds is longer than would fit into the S/C so the feeds are profiled. Conical Q and Ka band feed fit naturally. In V and W bands, the feeds naturally want to be much shorter than required and so they are lengthened with corrugated waveguide.

Table 1. Feed Specifications

Band designation	K	K_a	Q	V	W
Parameters					
Design frequency (GHz)	22	30	40	60	90
Frequency range^a (GHz)	20-25	28-37	35-46	53-69	82-106
Feed Bandwidth^a (GHz)	5	9	11	16	24
Total Number	2	2	4	4	8
Microwave Properties					
Feed FWHM^b (deg)	8.8°	8.3°	7.0°	8.0°	8.4°
Gain^c (dB)	26.79	27.23	28.77	27.28	26.40
Secondary ET (dB)	-48.7	-54.4	-58.8 (46)	-58.7	-57.2
Primary ET (dB)	-13.1	-20.2	-21.0 (46)	-21.0	-19.6
Far field^d (cm)	177	162	215	143	96
VSWR^e	1.00	1.01	1.02	1.01	1.03
Absorptance^f (dB)	0.004	0.009	0.01	0.02	0.03
Emission Temp^g (mK)	75	170	180	370	550
Effective Temp^h (mK)	75	170	190	370	570
Mechanical Properties					
Net Length^i (cm)	53.640	54.213	56.762	56.959	60.329
OMT end diam. (cm)	1.250	0.834	0.668	0.441	0.297
Aperture diam. (cm)	11.953	9.754	9.624	6.447	4.316
No. Grooves	117	170	217	329	533
Copper Throat^j	No	No	Yes	Yes	Yes
Length of Copper (cm)	...	...	5.283	8.534	11.110
No. Sections	1	1	3	4	5
Mass/Feed^k (gm)	820	840	520	280	192
Total (gm)	1640	1680	2080	1120	1536

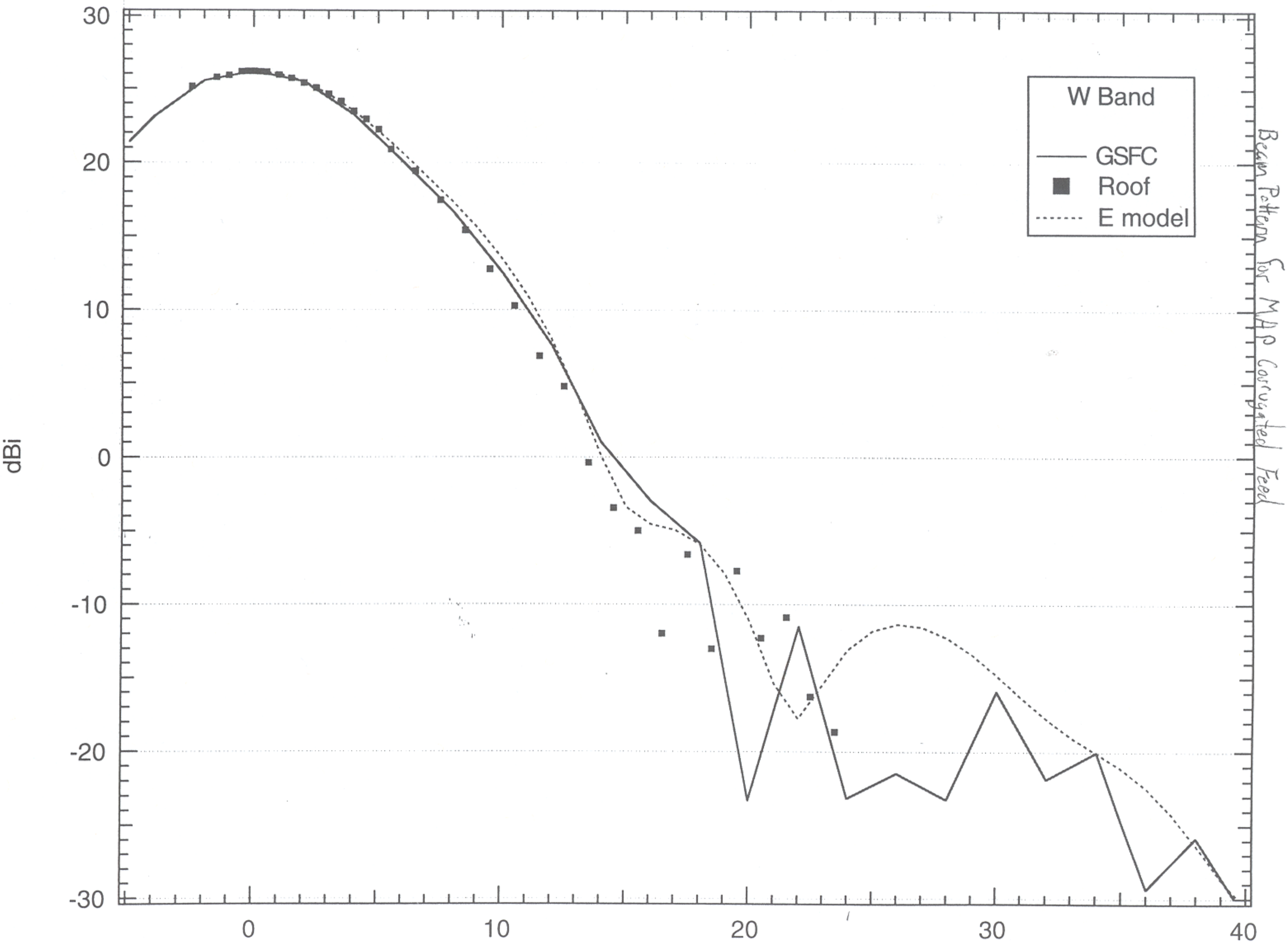

Beam Pattern for MAP Corrugated Feed

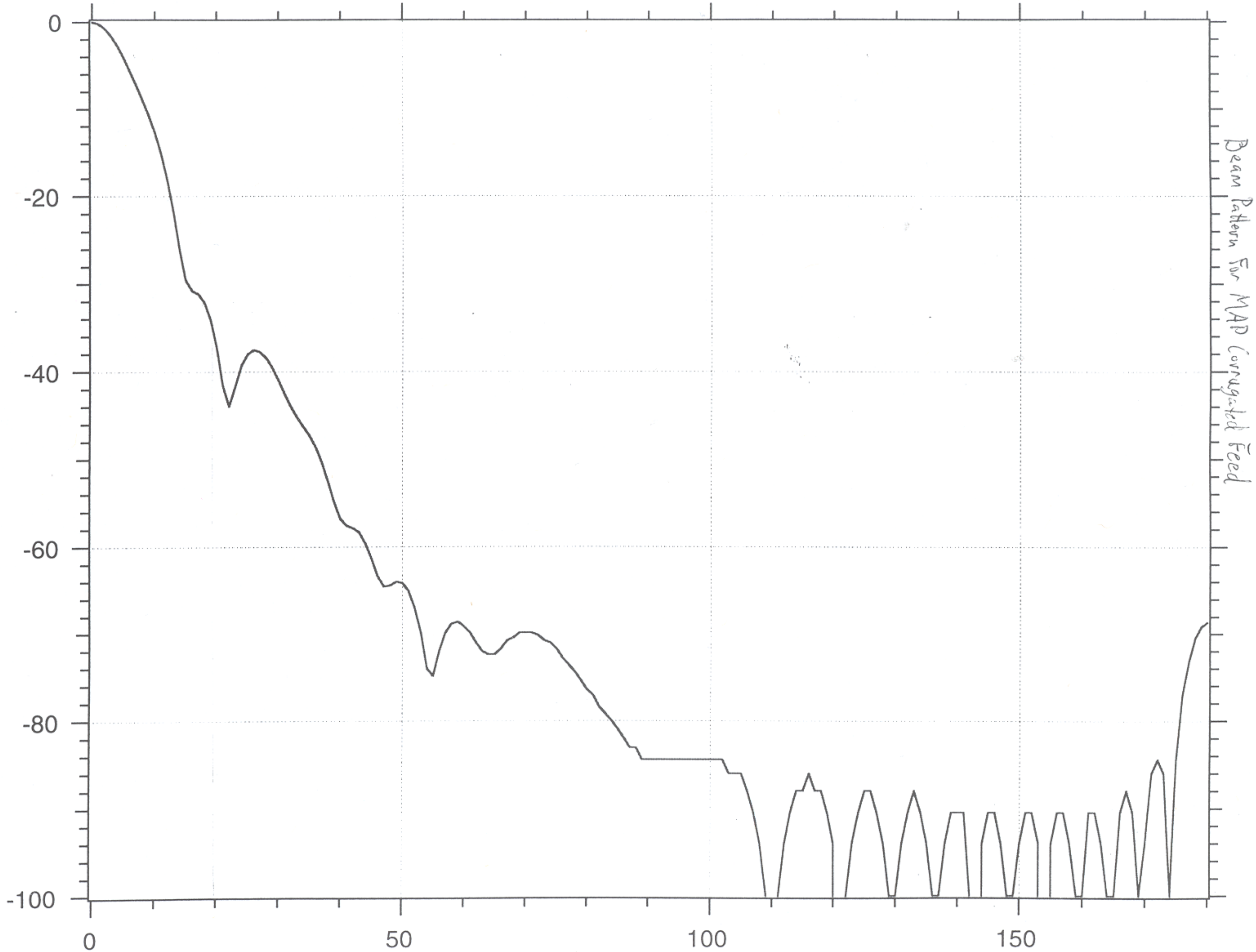

Beam Pattern For MAP Corrugated Feed

G = 26.4 dB @ 90 GHz

millitech®

Millimeter Wave Products and Services

Millimeter Wave Orthomode Transducer Test Data Sheet

CUSTOMER: Princeton University

P.O. NO: ________

MODEL NO: CBC-10-01836

SER. NO: 024

DESCRIPTION: Orthomode Transducer

DATE: 9/11/97

JOB NO: 67567.001

REF NO: ________

TEST DATA

Waveguide Band: WR-

Frequency Range: 82-106 GHz

Bandwidth: 7.5 %

Center Frequency: 94 GHz

Flange: MIL-F-3922/67B-010

Parameter	Specified	Measured
Insertion Loss: (dB)	N/A	.53 SIDE .81 THRU
Isolation: (dB)	19dB	29.56 SIDE 26.26 THRU
Return Loss: (dB)	14dB	13.47 SIDE 16.85 THRU

Sweep Attached

Comments:

Technician: ________

Quality: Paul Sull

A

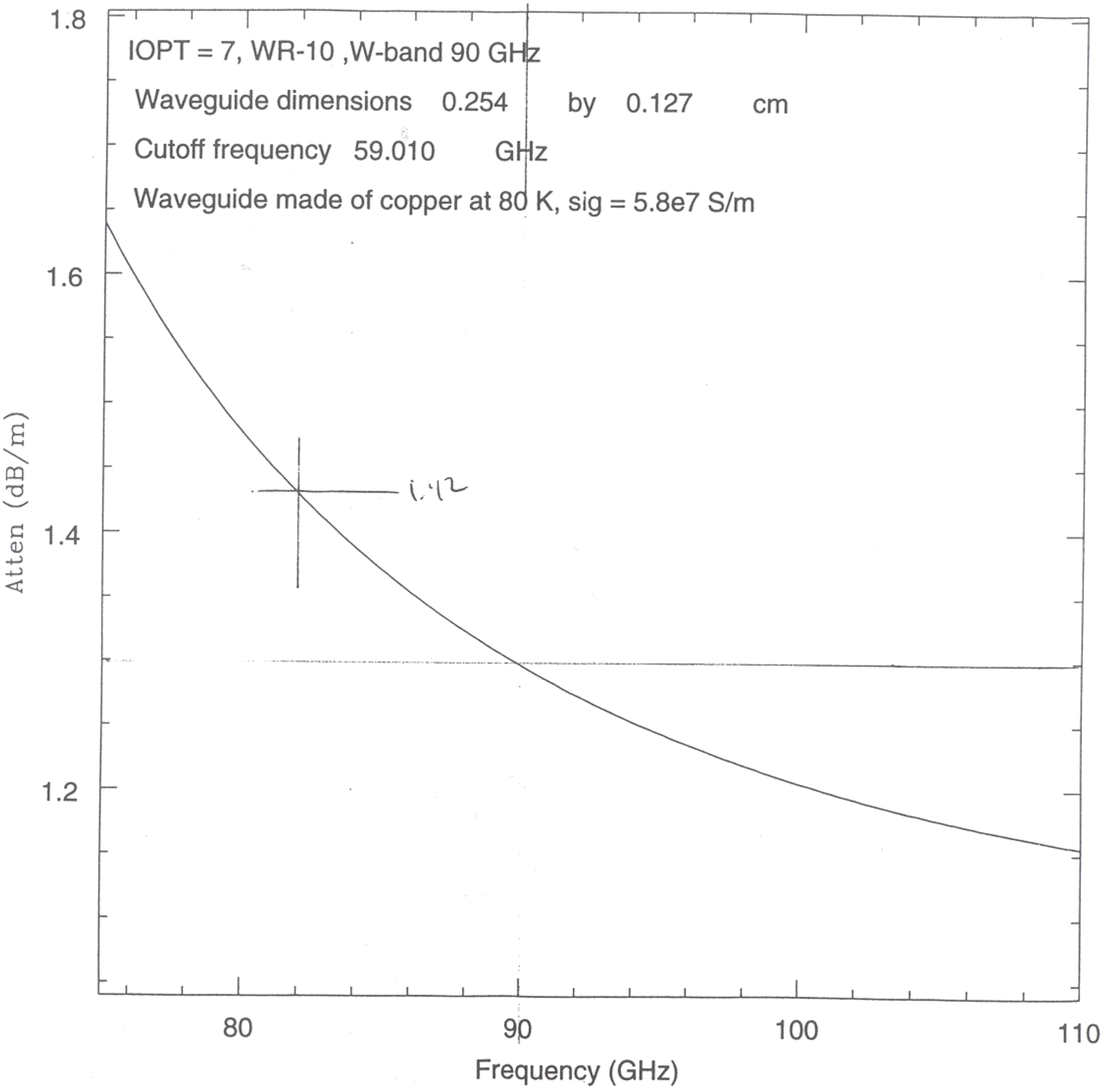
IOPT = 7, WR-10 ,W-band 90 GHz
Waveguide dimensions 0.254 by 0.127 cm
Cutoff frequency 59.010 GHz
Waveguide made of copper at 80 K, sig = 5.8e7 S/m
1.8
1.6
1.4
1.2
Atten (dB/m)
80
90
100
110
Frequency (GHz)
1.42

millitech®
Millimeter Wave Products and Services

MOTORIZED WAVEGUIDE SWITCH
TEST DATA

MODEL NO: MWS- 10-0BP3W S/O NO: A7641.001

SERIAL NO: 019 FREQUENCY RANGE: 75-110GHz

1.0 ISOLATION

Specified: 50 dB (min) Measured: 50 dB

2.0 VSWR (RETURN LOSS)

Specified: 1.15:1 (max) Measured : 1.15:1

3.0 INSERTION LOSS

Specified: 1.00 dB (max) Measured: 0.85 dB

NOTE:

TEST ENGINEER: LAMONT SMITH Date: 03-21-97

QA: Date: 3/24/97

millitech®

Millimeter Wave Products and Services

MIXER TEST DATA SHEET

CUSTOMER: Princeton University
P.O. NO:
MODEL NO: MXP-10-RSSXL
SER. NO: 047
DESCRIPTION: WR-10 Balanced Mixer
DATE: 12/11/96
JOB NO: A7354.001
REF NO:

SPECIFICATIONS AND REQUIREMENTS

RF BANDWIDTH: 92 to 94 GHz
CONVERSION LOSS: 8 dB SSB max
LO FREQUENCY: 90 GHz

OPERATING CONDITIONS

RF FREQUENCY: 92 to 94 GHz
POWER: -10 dBm
LO FREQUENCY: 90 GHz
POWER: +13 dBm
IF FREQUENCY: 2 to 4 GHz

RF Frequency (GHz)	LO Frequency (GHz)	IF Frequency (GHz)	SSB Conversion Loss (dB)
92.0	90.0	2.0	6.9
92.5	90.0	2.5	6.5
93.0	90.0	3.0	6.1
93.5	90.0	3.5	6.5
94.0	90.0	4.0	6.8

Comments:

Technician: Frank Grimaldi **Quality Assurance:**

MILLIMETER-WAVE OSCILLATOR COMPANY
700 Ken Pratt Blvd. Suite 204-211
Longmont, CO. 80501
TEL 303-652-3294
FAX 303-652-3923

DATA SHEET

January 12, 1998

A voltage regulator and cable is supplied with the oscillator. Connect the cable to the oscillator and regulator. Apply the dc input voltage to the EMI filter located on the side of the regulator housing. The input voltage can vary from +9.0 to +15.0 Vdc. The ground return can be made to the ground terminals located on each side of the EMI input filter. The DC power supply should be able to provide at least .80 Amps of current for the Gunn diode to turn on and start proper oscillation.

Operating Voltage (Input to Regulator)	Operating Current
+9.0 to +15.0 Vdc	.35 Amps

Frequency	Power
90.00 GHz	36 mW

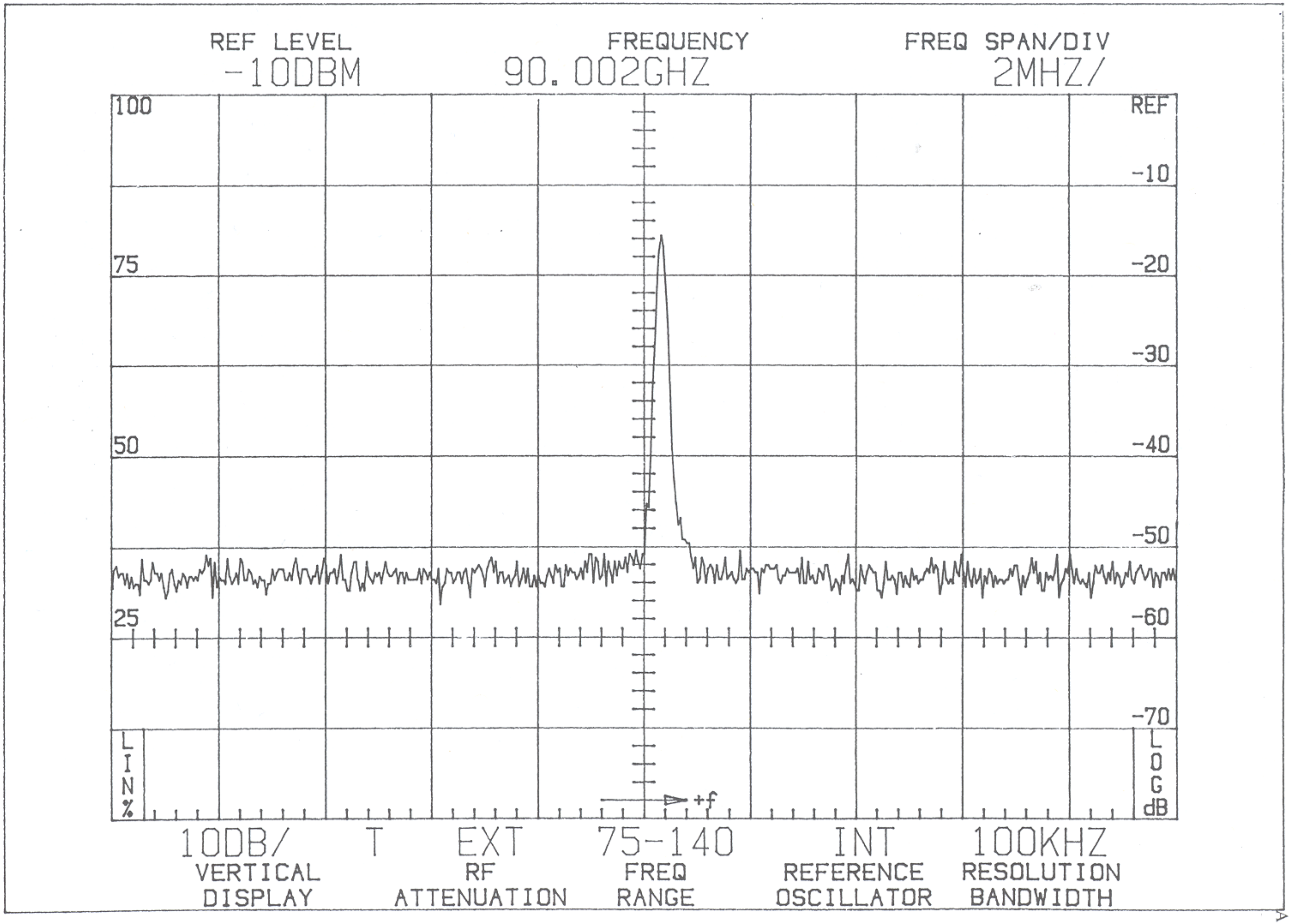
REF LEVEL
-10DBM
FREQUENCY
90.002GHZ
FREQ SPAN/DIV
2MHZ/
100
75
50
25
LIN %
REF
-10
-20
-30
-40
-50
-60
-70
LOG dB
+f
10DB/
VERTICAL DISPLAY
T
EXT
RF ATTENUATION
75-140
FREQ RANGE
INT
REFERENCE OSCILLATOR
100KHZ
RESOLUTION BANDWIDTH

millitech®
Millimeter Wave Products and Services

WAVEGUIDE TERMINATION
TEST DATA

MODEL NO. WTR-10-R0000

DATE: 2-11-97

SERIAL NO. 262

WAVEGUIDE SIZE: WR-10

SALES ORDER NO. 7767

FLANGE: MIL-F-3922/67B-010

FREQUENCY BAND 75-110 GHz

TEST FREQUENCY 75-110 GHz

DATA

	SPECIFIED:	MEASURED:
VSWR:	1.06:1	1.06:1

Todd Roberts
PRODUCTION

PRODUCT ASSURANCE

Millitech Corporation, South Deerfield Research Park, Post Office Box 109, South Deerfield, Massachusetts 01373, U.S.A.
(413) 665-8551 FAX: (413) 665-2536 Customer Service: 1-800-6MILLITECH

A1

RYT INDUSTRIES
336 MATHEW ST. • SANTA CLARA, CALIFORNIA

DATA SHEET

MODEL NO. 300037

SERIAL NO. 243

RYT
QA
1

DATE 3/7/97

TECH.
signature

CUSTOMER PRINCETON UNIVERSITY

FREQ	VSWR			ISOLATION (dB)			LOSS (dB)		
GHz	1	2	3	2-1	3-2	1-3	1-2	2-3	3-1
2.0	<1.20	<1.20	<1.20	>21	>21	>21	<0.40	<0.40	<0.40
3.0	↓	↓	↓	↓	↓	↓	↓	↓	↓
4.0									

RYT 114 (3-78) fc

Oct 8 98

Miteq Amplifier

AFD3 -020040-15
S/N 64447

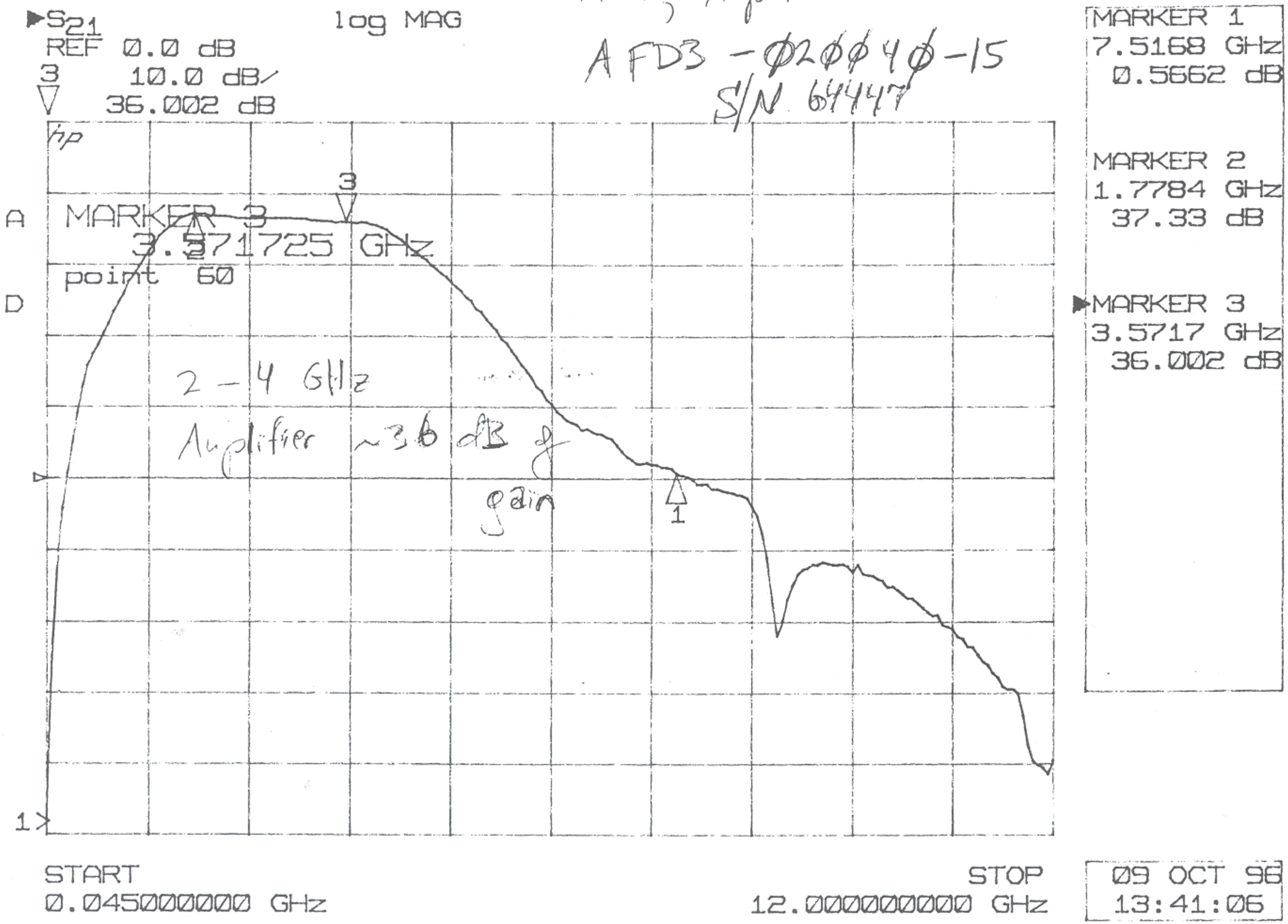

2 - 4 GHz
Amplifier ~36 dB of gain

Model 8472

is mechanical
t does not
otify the
shipping con
aterial shows
as the
ing mate-
office
hout wait-

the
tor for
nale
put

Table 1. Specifications

Frequency Range: 10 MHz to 18 GHz.

NOTE

RF may leak through the output connector, especially below 1 GHz. It can be reduced, if objectionable, with a suitable low-pass filter.

Frequency Response:[1,2]
±0.2 dB over any octave 10 MHz to 8 GHz;
±0.3 dB 10 MHz to 12.4 GHz;
±0.5 dB 10 MHz to 15 GHz;
±0.6 dB 10 MHz to 18 GHz.

Maximum Operating Input Power: 200 mW, peak or average.

Maximum Short Term Input Power: 1 watt (typical) peak or average for < 1 minute.

Sensitivity:[1,3]
High Level: <0.35 mW produces 100 mV output.
Low Level: >0.5 mVdc/μW CW.

SWR:[1,2]
10 MHz to 4.5 GHz, 1.20; 4.5 GHz to 7.0 GHz, 1.35; 7.0 GHz to 12.4 GHz, 1.50; 12.4 GHz to 18 GHz, 1.70.

Input Impedance: 50Ω (nominal).

Output Impedance:[2] 1 to 2 kΩ (typically 1.3 kΩ) shunted by 20 to 60 pF (typically 30 pF).

Output Polarity: Negative (refer to Options for positive polarity units).

Detector Element: Supplied (refer to Table 2 for replacement elements).

Bias: Not required.

Noise: <50 μV p-p with CW applied to produce 100 mV output, 400 kHz bandwidth.

Options:

Option 001: Matched detector pair. Frequency response characteristics (exclusive of basic sensitivity) track within ±0.2 dB from 10 MHz to 12.4 GHz, ±0.3 dB from 12.4 GHz to 18 GHz.

Option 003: Positive polarity output.

Option 100: Female OSSM-type output connector.

Environmental:
Operating Temperature: −20° C to +85°C.
Humidity: <95% relative
Vibration: 20G from 80 to 2000 Hz
Shock: 100G for 11 ms
Altitude: 4570m (15.000 ft.).

General:
Weight: Net 57 g (2 oz.)
Dimensions: 64 mm long, 14 mm diameter (2.50 in. long, 0.56 in. diameter).

---

[1] Specifications given for +25°C unless otherwise noted.

[2] Measurement made at −20 dBm.

[3] Sensitivity decreases with increasing temperature, typically: 0.5 dB from −20°C to +25°C: 0.5 dB from +25 °C to +40°C; 1 dB from +40°C to +55°C; 1.25 dB from +55°C to +75°C; 4 dB from +75°C to +85°C.

instrument is being returned to Hewlett-Packard for servicing, attach a tag indicating the type of service required, return address, model number, and serial number. Also , mark the container FRAGILE to assure careful handling. In any correspondence, refer to the instrument by model number and serial number.

21. OPERATION

CAUTIONS

Static discharge can damage the detector element. A 100 pF capacitor (1.2 m [4 ft.] of coax cable) charged to 14 volts stores .1 erg, the maximum pulse rating of the detector element. Connect cables to test equipment and discharge the center conductor before connecting to the detector.

DO NOT NEEDLESSLY HANDLE DETECTOR ELEMENT USED IN CRYSTAL DETECTOR. Static electricity which builds up on a person, especially on a cold dry day, must never be allowed to discharge through the crystal detector. Avoid exposed leads to or from the crystal detector, since these are often touched accidentally.

22. Operating Information

23. The crystal detector can be used as a demodulator to obtain a pulse envelope which can then be

Figure 75. The apparatus.

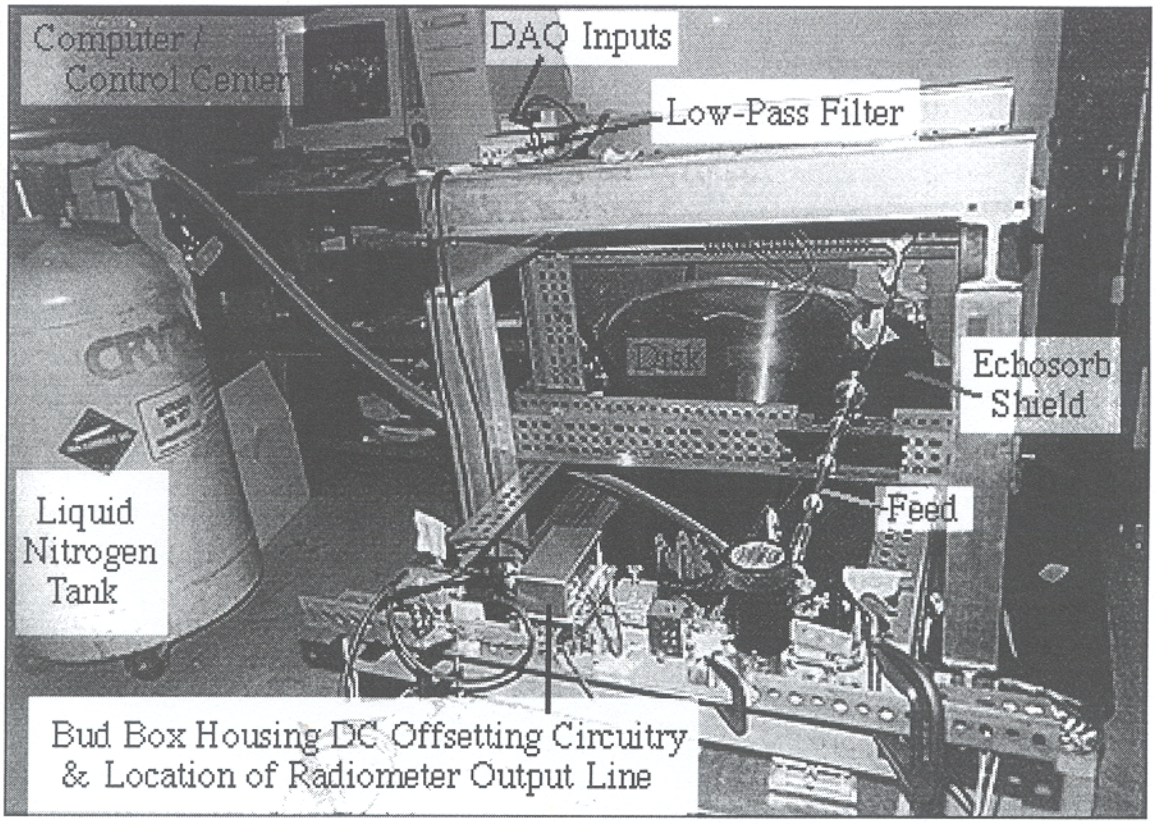

Appendix B: How to Operate the Apparatus

F1. Mounting a new sample.

Before removing or placing a new sample disk onto the axle, it is essential to disconnect the feed horn. You want to be careful that nothing scratches the disk surface as you remove it. If there is a sample already attached and the Echosorb shield is in place, you should note the position of the shield and then remove it.

Now to remove a disk already in place, you will need to unscrew the four small bolts holding the cap to the axle collar in place. Next, using a socket wrench, remove the four large bolts (5/8") that hold the collar and the wheel in place. Be careful, the samples are heavy. It might be necessary to have assistance holding the sample in place while unbolting the collar. When the collar is off, slide the disk off the axle slowly, using both hands, and guide it out of the cage, taking care not to touch any delicate sample surfaces. Finally, remove the small piece of aluminum used in triggering from the underside of the disk. This will be needed for each sample. To install a new sample, reverse this procedure.

When the new sample is in place, you will need to make certain that it is flat. A dial indicator has proven satisfactory for this task. Attach it so that the sensor rubs the *back* of the sample. Thin metal shim can be obtained in the stockroom and inserted between the disk and axle to level the disk. Measuring the rise and fall of the disk from the outer edge, best results require a readout difference of about 10mil from the dial indicator.

When the disk is flat to the desired amount, reattach the echosorb shield and the feed-horn. The shield should be such that it hides the outer edge of the disk from the beam path while not rubbing up against the disk. For consistent results, keep the feed horn a constant distance from the sample. Two inches has worked well for this experiment.

F2. Filling the Nitrogen Bath

Next the cold load should be put in place. Fill the nitrogen bath deeply enough that all the Echosorb on the bottom of the bath will remain submerged for the course of your data run. The rate at which the nitrogen depletes can be somewhat unpredictable. At best, a full bath will last you eight hours. It will deplete much faster if the bath has begun to leak. So far, we have replaced the lining once. If the nitrogen depletes itself quicker than you would like, you may want to replace the lining.

When filling the bath, take care not to let the hose from the nitrogen tank rest against the cage. This will cool the cage a great deal, and as aluminum transports heat so well, the radiometer temperature will decrease and voltage outputs will drift.

F3. Operating the Radiometer

The radiometer output voltage tends to drift around, especially after all the amplifiers have just been powered up. To minimize the drift you should turn on the system power a day in advance and allow everything to equilibrate. Doing so has proven to reduce the drift to less than 0.1mV/s.

When the bath is full of nitrogen, it is an excellent idea to check that the radiometer is working by waving your hand or a piece of Echosorb in front of the feed-horn. If the voltage output of the radiometer changes noticeably, it is working. Often you will have to make certain that the switch is in the correct position. This can be done manually or with the computer as discussed below.

There are soldered connections connecting the power supplies to each radiometer element that occasionally come undone. If the radiometer does not seem to be operating correctly, check to see that all components are receiving their power supply. Both IF amplifiers need +15V. The trigger needs +5V. The LO has a special regulator which receives +15V. These voltages come from the external (+28V) power supply and are regulated on the aluminum mounting plate of the radiometer. All the operational amplifier circuitry requires ±15V which comes from the supply at the front of the cage.

When the radiometer is operating correctly, you will need to calibrate it. This should be done before, and probably after, every data run for each polarization. The cold load signal is represented well by the reflected signal from the sample disk. To get the 293K voltage, a piece of 1" Echosorb can be placed in front of the feed. The calibration is then the observed voltage difference between the two signals divided by the known temperature difference.

The output of the radiometer (the coaxial port labeled "Out") should be connected to the post-detection low pass filter. Before you connect to the filter, open the silver bud box on top of the radiometer (to which you have just connected the filter) and with a screw driver, turn the screw on the potentiometer and minimize the signal DC level. This will keep the filter from overloading when run in DC coupling mode. Now, attach the radiometer output to the filter. Then connect the radiometer to the filter. Set the 3dB point of the filter to below the Nyquist critical frequency (Section IV).

The switch driver requires a large current (~1A), +28V power supply. Preferably, as the switch tends to draw a great deal of current only when it is in the process of switching, hence causing the voltage level in the power supply to drop briefly, it should be powered by a separate supply from the rest of the radiometer.

F4. Taking Data

The apparatus is now set up and equilibrated. There are three connections which need to be made to the computer. First, run the line from the triggering circuit to the SCB-68 I/O Connector. Connect the ground wire to digital ground (pin 4). Connect the positive voltage wire to "EXTTRIG*" (pin 11). Also, inside the connector, a connection should be made between pin 11 and pin 41. Second, there are three lines coming from the switch driver. The ground wire (grounded to the apparatus cage) should be connected to digital ground (pin 15). The two wires sending the logic signals to the driver should be attached to digital I/O ports 0 and 1 (pins 52 and 17). Finally, connect the radiometer signal from the low-pass filter output to analog channels 0 and 1 (pins 68 and 33). The ground wire is not connected to the computer's ground as there is invariably a great deal of noise pickup in and around the computer which makes the DAQ ground undependable. It is best to operate with the DAQ in differential mode as we are doing.

The primary Lab View program for co-adding the receiver signal is called `mapscope.vi`. It can be found in the directory `C:\Programs Files \National In-`

`struments \LabView \map`. The program is designed to co-add the signal from two of the switch positions, keeping track of each separately and displaying each as waveform graphs during data intake. The program's console is rather self-explanatory. There are three fields that may need to be changed. First, the sampling rate should be set as discussed in Section IV. For disks rotating near 1Hz, a value of 1000(ms) works nicely. This means that 1000 samples will be taken every second. Second the number of iterations spent at each switch position before changing should be set. The computer controls the switch position by sending logic pulses to the switch driver. Keep in mind that the more often you switch between polarizations, the more data you lose. On the other hand, you want to switch enough that the system doesn't change appreciably between switchings. In this experiment, we switch between channels approximately every five minutes. Lastly, the total number of iterations should be specified so that the program know when to stop taking data and when to save the averaged signal to file.

Before starting the program, turn the power on for the motor which spins the sample. Power the motor up and down slowly. The first thing that `mapscope.vi` calculates is the rotation period of the disk. You can stop and restart the program as needed until you have adjusted the power to the motor and the disk rotation period. The motor tends to seize up if it rotates the disk with a period shorter that about 0.6s. An 0.8s period is suggested.

In addition to `mapscope.vi`, there are three other important LabView programs in the same directory. There is a small vi called `salvage.vi` that can be used to retrieve data from a run that, for whatever reason, `mapscope.vi`did not save to file. Just use the arrow tool to select the waveform graph containing the data in `mapscope.vi` and past it into the main console of `salvage.vi`. When you hit run, the program will prompt you for a destination and will save the data to disk.

There is also a small program called `calibrate.vi`. This is simply a console with two switches; each can be logical TRUE or logical FALSE. This allows you to control the switch position through the switch driver. The program is called `calibrate.vi`because it makes it simple to go between switch positions at the beginning of each data run when measuring the system calibration.

Finally, there is a vi called `plot.vi`which allows for the plotting, binning, and scaling of data saved to file. There are two channels so as to allow comparison of two data files.

All of the LabView programs are straight-forward and easily dissected. Enjoy.